NASA CR-3513

NASA Contractor Report 3513

ORIGINAL
COMPLETED
132

An Experimental Investigation of Gapwise Periodicity and Unsteady Aerodynamic Response in an Oscillating Cascade

I - Experimental and Theoretical Results

Franklin O. Carta

CONTRACT NAS3-22018
JUNE 1982

NASA

NASA Contractor Report 3513

An Experimental Investigation of Gapwise Periodicity and Unsteady Aerodynamic Response in an Oscillating Cascade

I - Experimental and Theoretical Results

Franklin O. Carta
United Technologies Research Center
East Hartford, Connecticut

Prepared for
Lewis Research Center
under Contract NAS3-22018

National Aeronautics
and Space Administration

**Scientific and Technical
Information Office**

1982

I BEST DOCUMENT AVAILABLE

BLANK PAGE

TABLE OF CONTENTS

	Page
SUMMARY	1
INTRODUCTION	2
LIST OF SYMBOLS	4
EXPERIMENTAL EQUIPMENT AND PROCEDURES	8
Oscillating Cascade Wind Tunnel and Air Supply	8
Test Airfoils	9
Oscillatory Drive System	10
Instrumentation	10
TEST PROGRAM AND DATA ACQUISITION	13
Calibration Procedures	13
Test Plan	13
Steady Data Acquisition and Reduction	14
Unsteady Data Acquisition and Initial Reduction	15
UNSTEADY RESULTS	18
Analysis	18
Gapwise Periodicity	18
Aerodynamic Damping and Stability	21
Chordwise Distributions	22
Comparison With Theory	24
Intergap Sidewall Variations	25
Additional Comparisons	27
CONCLUSIONS AND OBSERVATIONS	29
Preliminary Remarks	29
Primary Findings	29
Secondary Findings	30

BEST DOCUMENT AVAILABLE

TABLE OF CONTENTS (Cont'd)

	Page
APPENDICES	33
1. DERIVATION OF RELEVANT EQUATIONS	33
2. POSSIBLE SOURCES OF GAPWISE PERIODICITY SCATTER	44
3. ACOUSTICAL RESONANCE	48
4. HIGHER HARMONIC BEHAVIOR AND WIND TUNNEL DISTURBANCES	49
REFERENCES	51
TABLES	53
FIGURES	62

BEST DOCUMENT AVAILABLE

An Experimental Investigation of Gapwise Periodicity and Unsteady Aerodynamic Response in an Oscillating Cascade

I - EXPERIMENTAL AND THEORETICAL RESULTS

SUMMARY

Tests were conducted on a linear cascade of airfoils oscillating in pitch to measure the unsteady pressure response on selected blades along the leading edge plane of the cascade, over the chord of the center blade, and on the sidewall in the plane of the leading edge. The tests were conducted at a constant inlet velocity of 61 m/sec (200 ft/sec) for all 96 combinations of 2 mean camberline incidence angles (α_{MCL} = 2 and 6 deg), 2 pitching amplitudes ($\bar{\alpha}$ = 0.5 and 2 deg), 3 reduced frequencies (k = 0.072, 0.122, and 0.151 based on semi chord), and 8 interblade phase angles (σ = 0, ± 45, ± 90, ± 135, 180 deg). The pressure data were reduced to Fourier coefficient form for direct comparison, and were also processed to yield integrated loads and, particularly, the aerodynamic damping coefficient. In addition, results from the unsteady Verdon/Caspar theory for cascaded blades with nonzero thickness and camber were compared with the experimental measurements.

The three primary results that emerged from this investigation were: 1) from the leading edge plane blade data, the cascade was judged to be periodic in unsteady flow over the range of parameters tested, 2) as before, the interblade phase angle was found to be the single most important parameter affecting the stability of the oscillating cascade blades, and 3) the real blade theory and the experiment were in excellent agreement for the several cases chosen for comparison. These are felt to be particularly significant because 1) this was the first known test of unsteady periodicity in cascade, and its verification lends credence to the self-consistency of the data gathered herein, 2) the cascade damping measurements continue to corroborate previous assessments of the importance of interblade phase angle in controlling stability, and 3) the mutual agreement of real blade theory and experiment represents an important milestone because it establishes the validity of both.

BEST DOCUMENT AVAILABLE

INTRODUCTION

The use of linear cascades to investigate phenomena related to turbomachinery blades has always been predicated on the ability of the rectilinear cascade to model blades in an annular array. To this end, steady-state experiments have customarily been devised with sufficient flow and geometric control to provide a uniform, or periodic, flow behavior over as much of the cascade center (i.e., the measurement region) as possible. Although this is desirable in dynamic testing, as well, unsteady periodicity is not, as a rule, verified in such tests. Virtually all of the unsteady cascade experiments reported on in the open literature generate data on one or two blades near the center of the cascade with no additional measurements away from the cascade center.

Several test programs have been undertaken in the United Technologies Research Center (UTRC) Oscillating Cascade Wind Tunnel (OCWT) to measure the unsteady loads on the center blade of an 11-blade cascade oscillating in pitch (Refs. 1, 2, 3, 4). These tests, which have investigated the effects of varying frequency, interblade phase angle, and incidence angle, have indicated a strong cascading effect, influenced largely by changes in interblade phase angle, on blade response. Our most recent published results (Ref. 4) have shown that changes in interblade phase angle from negative values (backward travelling waves) to positive values (forward travelling waves) lead to instabilities, even under modest load. All tests previously conducted in the OCWT have been at the (relatively) large amplitude of $\bar{\alpha} = 2$ deg, and the mean camber line incidence angle has been representative of modest to high loading ($\alpha_{MCL} \geq 6$ deg). Furthermore all measurements have been made only on the center blade of the cascade, with no opportunity to verify dynamic periodicity.

The research program just completed had a three-fold objective, addressing the three limitations of previous experimental programs. The specific major tasks undertaken in this experiment and reported on herein were:

1) to examine the gapwise periodicity of the steady and unsteady blade loads under a variety of conditions;

2) to determine the effect of a smaller pitching amplitude on the unsteady response;

BEST DOCUMENT AVAILABLE

3) to examine the effects of steady loading on the unsteady response by performing these tests at both low and modest incidence angles.

In addition, comparisons with an advanced unsteady theory for thick, cambered airfoils were made, and unsteady intergap pressure measurements were made along the leading edge plane. Details of this study will be found in the subsequent sections of this report.

BEST DOCUMENT AVAILABLE

LIST OF SYMBOLS

Note: Equation or figure numbers refer to the defining relationship or to the first use of the given symbol

A	area under $f(\xi)$, Eq. (11)
C	general amplitude or coefficient, Eq. (31)
C_M	moment coefficient per unit amplitude, positive nose up, Eq. (10)
C_N	normal force coefficient per unit amplitude, positive up (toward suction surface), Eq. (9)
C_p	unsteady pressure coefficient per unit amplitude, Eq. (1)
C_W	work coefficient, Eq. (15)
c	airfoil chord, m, Eq. (52)
ΔC_p	unsteady pressure difference coefficient per unit amplitude, Eq. (5)
F	periodic function, Eq. (21)
f	frequency, Hz, or function to be integrated, Eq. (11)
J	maximum number of Gaussian integration stations, Eq. (11)
j	Gaussian integration integer, Eq. (11)
k	reduced frequency, $= c\omega/2V$, Eq. (52), or harmonic integer, Eq. (21)
M	Mach number, Eq. (52)
n	blade number, Eq. (38)
p	pressure, newton/m^2, Eq. (1)
q	dynamic pressure, newton/m^2, Eq. (48)
t	time, sec, Eq. (1)

BEST DOCUMENT AVAILABLE

LIST OF SYMBOLS (Cont'd)

V	velocity, m/sec, Eq. (48)
W_j	Gaussian integration weighting coefficients, Eq. (11)
x	chordwise blade coordinate, positive aft, m
y	normal blade coordinate, positive toward suction surface, m
Z_p	total pressure loss coefficient, Fig. 11
z	Gaussian interval multiplier, Eq. (13)
α	pitching angle, positive nose up, deg, Eq. (3)
$\bar{\alpha}$	pitching amplitude, deg, Eq. (1)
α_{MCL}	mean camberline incidence angle, positive nose up, deg
α_{THEORY}	theoretical incidence angle, positive nose up, deg
β_1	inlet angle, deg, Fig. 2
β_1^*	mean camber line stagger angle, Eq. (52) or Fig. 2
δ	phase angle, deg or radian, Eq. (32)
ϵ	eccentricity, Eq. (46)
η	gap fraction, Fig. 8
θ	response phase angle relative to motion, deg or radian, Eq. (41)
$\Delta\theta$	flow turning angle, deg, Fig. 11
ν	integer, Eq. (52)
Ξ	aerodynamic damping parameter, Eq. (19)

BEST DOCUMENT AVAILABLE

ξ	Gaussian coordinate distance, Eq. (11)
ρ	air density, newton sec^2/m^4, Eq. (48)
σ	interblade phase angle, positive for forward traveling wave, deg or radian, Eq. (38)
τ	slant gap, m, Eq. (52)
ϕ_M	moment phase angle, deg or radian
ϕ_N	normal force phase angle, deg or radian
ϕ_p	pressure phase angle, deg or radian, Eq. (4)
$\phi_{\Delta p}$	pressure difference phase angle, deg or radian, Eq. (8)
x	dimensionless distance along chord, positive aft, Eq. (1)
x_p	pivot axis location, Eq. (10)
ψ	general phase angle, deg or radian, Eq. (31)
ω	frequency of oscillation, rad/sec, Eq. (2)

Subscripts, superscripts, and special symbols

$( )_A$	actual value, Eq. (46)
$( )_I$	imaginary part, Eq. (2)
$( )_j$	jth Gaussian station, Eq. (11)
$( )_k$	kth harmonic, Eq. (21)
$( )_L$	lower or pressure surface, eq. (5)
$( )_o$	nominal value, Eq. (46)

BEST DOCUMENT AVAILABLE

LIST OF SYMBOLS (Cont'd)

$( )_R$ real part, Eq. (2)

$( )_s$ sidewall

$( )_U$ upper or suction surface, Eq. (5)

$( )^n$ blade n, Eq. (35)

$( )^*$ adjusted gapwise value

$(\bar{})$ amplitude, Eq. (2)

Re| | real part of | | , Eq. (15)

BEST DOCUMENT AVAILABLE

EXPERIMENTAL EQUIPMENT AND PROCEDURES

Oscillating Cascade Wind Tunnel and Air Supply

The experimental program was carried out in the UTRC linear subsonic Oscillating Cascade Wind Tunnel (OCWT) which is shown schematically in Fig. 1. The test section of this facility is 25.4 cm (10 in) wide and 68.6 cm (27 in) high, and the sidewall configuration is currently arranged to accept 11 shaft-mounted blades in cascade. The bearing mounts for these blades are equally placed along a line making a 30 deg angle with respect to the tunnel floor, and hence the sidewall stagger angle of the OCWT is nominally 30 deg. Actual blade stagger angles can be varied according to the configuration and blade orientation. The distance between blade shaft centers along the stagger line is 11.43 cm (4.5 in).

Sidewall boundary layer slots are located 34.29 cm (13.5 in) ahead of and parallel to the bearing mount locus line. For a 15.24 cm (6 in) chord blade pivoted at its midchord the slots are 26.67 cm (10.5 in) (or 1.75 chord lengths) ahead of the locus of blade leading edges. Similar slots are located in the tunnel ceiling above the uppermost blade and in the tunnel floor below the lowest blade, with the slot knife edges approximately in line with the blade leading edges. Slot capture areas were designed to accommodate boundary layer thicknesses associated with test section speeds up to 121.9 m/sec (400 ft/sec); therefore, the ceiling, sidewall, and floor slot widths are .89cm, 1.52 cm, and 1.91 cm (0.35 in., 0.60 in., and 0.75 in.), respectively.

Each slot opens onto its own plenum, and each plenum is separately vented to a common vacuum line which is evacuated by a Roots-Connersville vacuum pump. The main 25.4 x 68.6 cm (10 x 27 in) test section receives its air from atmosphere through an upstream bellmouth and discharges downstream through two Allis-Chalmers centrifugal compressors which are driven by a P&WA FT-12 engine. Tests at 61 m/sec (200 ft/sec) and below showed that the boundary layer thickness, based on recovery to within 98 percent of free stream velocity, was approximately 0.51 cm (0.2 in) on either wall, and the spanwise velocity distribution was flat to within the limitations of the measuring probe (Ref. 1).

In this system, the inlet angle variations are obtained by rotating the floor and ceiling nozzle blocks about a pair of pivots whose centers lie along the locus of blade leading edges. The inlet bellmouth is configured such that the floor and sidewall panels of the bellmouth move with the floor nozzle block as a rigid unit while the upper panel of the bellmouth remains fixed to the ceiling nozzle block. In addition, the upper bellmouth panel has the freedom

BEST DOCUMENT AVAILABLE

to slide paraliel to the nozzle block, thus assuring a smooth closure of the inlet bellmouth. Because of the complicated interfaces between knife edges and sidewalls of varying lateral dimensions, several internal seals were required for each inlet angle.

The ceiling and floor slot knife edges form the leading edges of the ceiling and floor end blocks. These blocks serve the dual function of providing flow boundaries one gap space away from each end blade, and, at their trailing edges, of providing pivot points for the tailboards. Each tailboard is separately driven by an electric motor, and each has an angular potentiometer to monitor its position. The tailboards are used to ensure a uniform, undistorted exit flow. Experience has shown that this is achieved when the static pressure along the exit plane of the cascade is uniform.

To assure a uniform inlet flow condition, a fine mesh screen having 65 percent porosity was placed over the bellmouth, and a 15.24 cm (6 in) deep aluminum honeycomb with 2.54 cm (1 in) cell size was inserted within the rectangular entry region just aft of the bellmouth. Fine adjustments were made in the honeycomb placement and orientation to provide an undistorted inlet flow. An upstream cross-tunnel wedge probe, inserted between the sidewall boundary layer slot and the cascade leading edge locus, was sufficient to ensure proper operation of the OCWT. The wedge probe plane of symmetry was rotated to the desired flow angle, and the tailboard and sidewall suction adjustments were made to yield zero wedge probe unbalance as well as uniform upstream and downstream static pressure distributions along the cascade inlet and exit planes. A further discussion of this procedure will be found in Ref. 2.

Test Airfoils

The cascade configuration consists of eleven NACA 65-series blades, each having a chord of c = 15.24 cm (6 in) and a span of 25.4 cm (10 in), with a 10 degree circular arc camber and a thickness-to-chord ratio of 0.05. Figure 2 is a schematic drawing of four of the eleven blades as they are mounted in the wind tunnel. The relative positions shown are properly scaled but the blade geometry has been exaggerated for clarity in describing the blade shape parameters. The slant gap, measured along the blade-to-blade stagger line, is τ = 11.43 cm (4.5 in) so the gap-to-chord ratio is τ/c = 0.75.

For these tests the blade stagger angle, β_τ, measured between the tangent to the blade mean camber line at the leading edge and the leading edge locus line, is 30 deg. (Note that this angle is the complement of the NASA blade angle defined on pp. 184, 185 of Ref. 5.) The blade inlet angle, β_1, is measured between the inlet velocity, V, and the leading edge locus line. Hence, the mean camber line incidence angle is defined as $\alpha_{MCL} = \beta_\tau - \beta_1$. The blade profile in true scale is shown in Fig. 3, and the profile coordinates, in fraction of chord, are contained in Table 1.

BEST DOCUMENT AVAILABLE

Oscillatory Drive System

The entire set of airfoils is coherently driven in a sinusoidal pitching motion with an amplitude of $\bar{\alpha}$. The system is driven by a constant speed, 5.6 kW (7.5 hp) electric motor with a continuously variable speed transmission through a timing belt and pulleys, as shown in Fig. 1. The upper pulley drives a central pulley within the sidewall transmission, and through a series of internal timing belts and pulleys, all eleven internal pulleys are driven in the same direction and at the same speed. Finally, each internal pulley drives a four-bar linkage (described below) which produces the sinusoidal airfoil motion. The design oscillatory frequency range of the system is $3 \leq f \leq 150$ Hz, but recent testing has been confined to a range of $6 \leq f \leq 26$ Hz.

The four-bar linkage is shown in Fig. 4. The solid outline represents the actual hardware and the dot-dash lines show the location of each of the three physical bars plus the fourth fixed baseline bar. The eccentric cam, which is driven by an internal pulley, rotates at constant speed. The two intermediate links are bearing mounted at the cam and at their common point. The lower link is rigidly clamped to the blade drive shaft at its midchord and imparts the oscillatory motion to the blade. This system was designed to provide a motion having less than 0.5 percent second harmonic distortion. In this test program the cams were set to yield several values of interblade phase angle, σ, which is customarily defined positive for an equivalent forward traveling wave around the rotor. In the case of the stationary cascade pictured in Fig. 2, this is simulated by the lowest blade in the pack leading its upper adjacent neighbor. The interblade phase angle can be varied to any desired value by adjusting the orientation angle of each cam relative to its neighbor.

Instrumentation

Conventional pneumatic wind tunnel instrumentation is used to measure the flow properties in the test section. A pitot probe downstream of the inlet honeycomb measures the total pressure in the tunnel, and sidewall static taps, aligned with the sidewall stagger angle, are used to measure the static pressure along the inlet and exit planes of the cascade. The upstream taps are approximately halfway between the blade leading edges and the boundary layer scoop knife edges. Tunnel speed is set by measuring the inlet plane static pressure at tunnel midheight and referring it to the pitot pressure to calculate the dynamic pressure, $q = 0.5\ \rho V^2$. After manipulating both tail-boards, and the vacuum system for boundary layer flow removal, to yield a uniform (or nearly uniform) inlet and exit plane static pressure distribution, all pressures are recorded for subsequent use in calculating velocity distributions. In addition, records are made of the flow parameters in each of the four vacuum ducts, as well as tailboard potentiometer readouts and inlet temperature.

BEST DOCUMENT AVAILABLE

The center airfoil (blade no. 6) was extensively instrumented to provide measurements of several flow parameters. Ten minature high response pressure transducers were placed on each surface of the airfoil to obtain measurements of unsteady static pressures. Coincident in chord position with each high-response orifice is a pneumatic static pressure tap to provide a zero frequency reference for each unsteady pressure (see below). This blade is shown schematically in Figs. 5 and 6.

The instrumentation for the suction surface is shown in Fig. 5. Orifices for both the pressure transducers and the static taps were placed along the chord near the span center line. The specific chordwise locations, from 1.2 percent to 91 percent, were arranged in a Gaussian array to yield maximum accuracy in the numerical integration of the resulting pressure distributions (Ref. 6). The same arrangement of pressure orifices was used on the pressure surface.

Conventional static tap construction was used with small bore hypotubing laid into the surface channels and potted into place. Small surface holes were then drilled into the tubing at the appropriate chordwise locations. These tubes were gathered at either span end and passed through bored holes in the end shafts.

A typical installation for the unsteady pressure transducers near the center blade leading edge is shown in Fig. 6 which is a section view in the chordwise plane of the first four suction surface transducers. This schematic shows how a series of counterbored (or milled) holes from the pressure surface, culminating in a small orifice hole to the suction surface, provides a receptacle for each minature transducer. In these sketches, the small circles in the top of each transducer represent the 15-mil wires which were placed in milled surface channels and carried out through the hollow shafts. Additional details on transducer installation can be found in Ref. 7.

Five other blades were also instrumented with miniature transducers. The blades are located in the cascade as shown in the schematic diagram in Fig. 7. Blade no. 6 is the fully instrumented center blade. Partial instrumentation was placed on blades no. 3, 4, 5, 7, and 9. Locations, in chord fraction, $\chi = x/c$, of all transducer orifices are listed for all blades in Table 2a. As shown, blades 3, 5, 7, and 9 have suction surface orifices at $\chi = 0.0120$, and 0.0622, and pressure surface orifices at $\chi = 0.0120$. Blade 4 also has suction surface orifices at $\chi = 0.0120$ and 0.0622 and has additional suction surface orifices at $\chi = 0.0050$ and 0.0350 with no orifice on the pressure surface. This permits a more detailed coverage of the pressure response near the leading edge of a centrally located blade without significantly interrupting the evaluation of cascade periodicity near the leading edge on the pressure surface.

BEST DOCUMENT AVAILABLE

Finally, an array of ten miniature transducers were mounted in the tunnel sidewall in the plane of the blade leading edges, as shown schematically in Fig. 8. (For simplicity these locations are depicted as being slightly forward of the leading edge plane although they were actually coincident with the plane.) The gap fraction location, η, of each transducer relative to the suction surface of blade 6 is listed in Table 2b. It is seen that these locations were selected to yield an increased placement density near each blade surface, several paired points relative to mid-gap (i.e., 1 and 10, 3 and 9, 4 and 8, 5 and 7), and two paired points having periodic relationships to blades 6 and 7 (i.e., 1 and 4 are to blade 6 as 8 and 10 are to blade 7).

BEST DOCUMENT AVAILABLE

TEST PROGRAM AND DATA ACQUISITION

Calibration Procedures

Prior to testing, all pressure transducers were calibrated. In most cases a small vacuum chamber was used, either to calibrate individual pressure transducers or entire instrumented blades. The pressure within the chamber was reduced to approximately 84 cm H_2O (33 in H_2O) below atmosphere in several steps, and transducer voltage output was recorded at each step. Several constant-temperature pressure cycles were recorded over a range of temperatures from -12°C (10°F) to 24°C (76°F) to simulate temperature ranges anticipated during testing. In some instances, for previously installed sidewall transducers, a vacuum line was applied directly to each transducer orifice to subject the transducer to the same range of pressures. In addition, selected transducers were subjected to occasional spot checks, using the vacuum line, to verify a previously measured sensitivity.

All calibration data were evaluated by least squares fit. The results were uniformly linear with correlation coefficients of 0.998 or greater. A small scatter in sensitivity with temperature of approximately ±2% per 55.6°C (100°F) was noted, but it was determined that this was within the manufacturer's specifications for these devices. In general, the tranducers and their associated circuitry performed reliably and yielded self-consistent results throughout the test program.

Test Plan

A total of 96 test conditions were run. These were comprised of all possible combinations of two mean camber line incidence angles (α_{MCL} = 2 deg, 6 deg), two pitching amplitudes ($\bar{\alpha}$ = 0.5, 2 deg), three frequencies (f = 9.2, 15.5, 19.2 Hz, and, for a constant velocity of 61 m/sec, or 200 ft/sec, this was equivalent to reduced frequencies $k = c\omega/2V = \pi cf/V$ = 0.072, 0.122, 0.151), and eight interblade phase angles (σ = 0 deg, ± 45 deg, ± 90 deg, ± 135 deg, 180 deg). In addition, two data runs were taken at each test condition. This was necessary because the number of desired data locations (47) exceeded the number of available data system channels (26). Hence, a relay was employed to switch between Mode 1, which contained all twenty blade-6 channels, five wall channels, and blade motion, and Mode 2, which contained all nineteen blade leading edge channels, six wall channels, and blade motion. Redundancy between modes was confined to the three leading edge stations on blade 6, one sidewall station, and blade motion. A tabulation of all data channels for each mode is contained in Table 3. In this table the blade location is coded by a three symbol array denoting blade number, suction or pressure surface, and location sequence from leading edge. Wall stations are numbered consecutively. The numerical value for each location is either blade chord fraction, x, or sidewall gap fraction, η.

BEST DOCUMENT AVAILABLE

Steady Data Acquisition and Reduction

Prior to the unsteady test sequences run at each mean camber line incidence angle, α_{MCL}, detailed steady-state tests were run. This was done to validate and document steady-state cascade periodicity over both leading and trailing edge cascade planes, and to obtain steady-state surface pressure measurements over the blade chord for subsequent use in comparisons with steady and unsteady theory. In addition, downstream flowfield measurements were taken that yielded cascade static pressure rise, flow turning, and blade loss.

These steady-state pressure data from tunnel and blade pneumatic sources were passed through two 48-port scanivalves and temporarily stored on a floppy disk together with calibration pressures and keyboard input quantities (e.g., run and point number, barometric pressure, ambient temperature, etc.) via a Perkin Elmer 7/16 minicomputer and associated peripheral equipment. The data were immediately transferred to a PDP-6 computer for processing on-line to provide tunnel flow velocity, and remained stored for subsequent detailed analysis of all pressure distributions.

An initial cross tunnel total pressure survey was taken to ensure that the exit flow from the inlet honeycomb was undistorted and parallel to the desired flow direction. With the exception of the sidewall boundary layer, which was removed ahead of the cascade leading edge plane, the upstream core flow was found to have a uniform total pressure distribution with a nominal deviation from the mean of less than ± 5 mm H_2O (±0.2 in H_2O). This is equivalent to a velocity deviation of approximately one percent relative to the free stream. A further indication of flow uniformity is shown in Fig. 9 in which the steady velocity profiles upstream and downstream of the cascade are shown. These values were calculated from a single total pressure measurement upstream of the blade row and two arrays of sidewall static pressures measured along lines parallel to the plane of the cascade, approximately one blade chord upstream and downstream of the leading and trailing edge planes. In this figure the vertical locations of all eleven blades and the upper and lower tunnel boundaries are also included along the ordinate.

With the assumption of a uniform total pressure field, the upstream velocity distributions in Fig. 9 are seen to be uniform to within ± 2 percent relative to the nominal velocity over the central measurement region (i.e., blades 3 through 9). The upstream velocity decrease near floor and ceiling are inferred from local sidewall static pressure increases. Downstream velocities show even greater uniformity. The small deviation in velocity between blades 4 and 5 (at .65 tunnel height) is a local sidewall phenomenon caused by the wake of the upstream wedge probe, and did not affect measurements at center span.

Steady-state chordwise pressure distributions for the two incidence angles tested are presented in Fig. 10. (These results differ from previous measurements cited in Ref. 4 by the reference p/q at the leading edge stagnation

BEST DOCUMENT AVAILABLE

point which is now zero instead of -1.0. With this change in reference p/q it is seen that the measurements of Ref. 4, denoted by dashed lines through solid symbols, compare favorably with those of the current experiment, particularly near the leading edge. Differences between the two sets of measurements are confined to the trailing edge region and are attributable to minor differences in tailboard settings.) There is a marked contrast in pressure distribution between α_{MCL} = 2 deg and 6 deg. It is obvious that α_{MCL} = 2 deg represents a low load condition, and it was specifically chosen to represent a condition on a cambered, thick blade that approximates the unloaded classical flat plate. The selection of α_{MCL} = 6 deg satisfied two requirements: 1) to provide data on a modestly loaded but unstalled cascade (based on the unstalled behavior of the steady chordwise pressure distribution and other evidence cited below), and 2) to examine the unsteady periodic behavior of a load condition run previously (Ref. 4) over a wide range of parameters.

As in Ref. 4, several other steady-state parameters were measured. Cascade pressure rise was obtained from the downstream wall static pressure change, and is indicated by the tic marks and the numerical values at the trailing edge of each plot in Fig. 10. It is seen that these values are in reasonable agreement with values that would be obtained from extrapolations of the surface pressure distributions to the trailing edge. In addition, flow turning through the cascade, $\Delta\theta$, was measured using the upstream and downstream wedge probes, and total pressure loss coefficient, Zp, was measured at center span using a 20-tube total pressure rake downstream of the blade row. Values for all three parameters are plotted as circled points in Fig. 11, and are compared with the earlier results of Ref. 4, which are plotted as triangular points. The consistency of the detailed agreement at α_{MCL} = 6 deg confirms the repeatability of the experiment. In addition, this figure shows overall trend agreement for both experiments, from α_{MCL} = 2 deg to 10 deg. Finally, the predicted minimum loss of Zp = 0.02 at α_{MCL} = 6 deg (cf. Ref. 4) is strongly confirmed by both experiments.

Unsteady Data Acquisition and Initial Reduction

During unsteady testing, OCWT data are collected by two systems, one which stores and computes pertinent steady-state parameters and provides on-line monitoring of external flow conditions (cf. previous section), and one which collects and stores all unsteady, high response data for subsequent processing. The latter will now be described briefly.

Unsteady blade and sidewall pressures and blade angular displacement are obtained as time varying voltages which are conditioned and amplified in an instrumentation package mounted close to the OCWT (to reduce transmission noise of low level signals). These high response transducer outputs are acquired and recorded in digital form for subsequent off-line processing by the Aeromechanics Transient Logging and Analysis System (ATLAS) which accepts up to 26 channels of data (cf. Fig. 12 for a system block diagram). Each channel

BEST DOCUMENT AVAILABLE

may be amplified and filtered as required. The heart of the system is a 26 channel transient recorder which digitizes and stores each channel simultaneously at sampling rates up to 200 kHz as selected by the operator. System control is provided by a Perkin Elmer 7/16 minicomputer system which interfaces with the operator through a graphics display terminal. The data system is capable of self-calibration using a built in programmable voltage standard which is under computer control. The system offers several modes of operation ranging from fully manual, where each step in the sequence (calibration, acquisition, and recording) is under operator control with the capability of aborting at any time, to fully automatic where these tasks are computer controlled according to preset parameters. Data acquisition may be initiated manually, by the computer, or on receipt of an external trigger pulse. For this program, the system was run in the manual-trigger mode. Typically, the operator at the computer console instructs the system to acquire data, using the preprogrammed software on the minicomputer program disk and several specific instructions pertinent to the particular experiment in progress. Acquired data, consisting of 1024 time-correlated samples for each active channel, can be spot-checked by the operator by displaying the contents of the memory of each channel on a built in scope, or can be recorded directly on a digital magnetic tape for subsequent off-line processing.

The acquisition rate for all unsteady data was set at 1000 samples/sec. Thus, for the three nominal test frequencies, f = 9.2, 15.5, 19.2 Hz, there were 9.4, 15.9, and 19.7 cycles of data available for analysis, or conservatively, there were 9, 15, and 19 full cycles available. Data for each channel were Fourier analyzed, primarily to provide first, second, and third harmonic results for ease in analyses, but also to provide a compact means of data storage for subsequent use. These data have been completely tabulated in a companion data report (Ref. 8) in which each run/point combination is fully documented and described, and the data are arranged in several convenient forms. In each case a total of 10 harmonics are displayed for each unsteady channel. It is seen that this is well within the bounds of the conventional sampling theorem (Ref. 9) requiring 2 or more samples/cycle in the highest harmonic of interest. A summary of these pertinent cycle parameters is presented in Table 4.

Unsteady data for each pressure channel were reduced to dimensionless time history form by successive multiplications of the raw ATLAS output (in computer counts) by the ATLAS calibration constant for each channel (volt/count) and the calibration constant for each transducer (psi/volt); the results were then divided by the wind tunnel free stream dynamic pressure (psi) and by the blade pitching amplitude (rad). Thus, in all subsequent discussions, it is understood that the unsteady pressure coefficient is the result of the following reduction,

$$Cp\ (\chi,t) = \frac{p\ (\chi,t)}{q\ \bar{\alpha}} \qquad (1)$$

BEST DOCUMENT AVAILABLE

where p and q have the same dimensions. Data for each channel were then Fourier analyzed, as described earlier, and presented in both component format and in amplitude and phase angle format. All results are harmonically referenced to the blade pitching motion except where otherwise noted. Specific manipulations of the data for each phase of the analyses that follow are described within each section.

BEST DOCUMENT AVAILABLE

UNSTEADY RESULTS

Analysis

Many of the analytical techniques used in reducing data or preparing the reduced data for examination have been used before (cf. Refs. 1-4), and a full derivation would not normally be warranted. However, in view of the extended analyses needed for periodicity evaluation, it is obvious that some analytical background should be provided. This has been done by gathering all relevant equations into Appendix 1, which has the added advantage of providing continuity of development. The topics covered in Appendix 1 are: basic definitions of notation and major quantities, Gaussian integration of pressures to obtain normal force and pitching moment, definition of aerodynamic damping, Fourier representation of time histories, and gapwise phase shift for periodicity comparisons. It should be noted, however, that the order in which the results are discussed below in this section is not necessarily the order of the exposition of the underlying analysis in Appendix 1.

All of the results described in the ensuing sections have been operated on by the analyses of Appendix 1. With few exceptions, these descriptions cover only the major observed trends in the reduced data -- a complete and detailed graphical or verbal description of the myriad results produced during the course of this investigation is clearly beyond the scope of the present document. However, a companion data report, comprised of computer printout of all relevant reduced data for all cases run, has been published (Ref. 8). From it the reader can reproduce all of the results described in this report, and can also construct any other desired output for direct study or comparison.

Gapwise Periodicity

The use of cascade data to represent turbomachinery behavior has always been predicated on the blade-to-blade periodicity of the cascade. In the past, steady state periodicity was routinely checked and, in most cases, required as part of the data acceptance procedure. This is not the case with unsteady periodicity, for several reasons. For example, increased numbers of high response transducers (or other data sources) on more than one blade and correspondingly increased numbers of signal conditioning and data acquisition channels produce significantly more data and represent considerably more cost than conventional unsteady tests. Nevertheless, such a test has been a recognized need for several years.

BEST DOCUMENT AVAILABLE

It is believed that the current experiment is the first systematic and detailed examination of unsteady periodicity in an oscillating cascade. As noted earlier, high response instrumentation has been confined to the leading edge regions of five blades grouped in the central region of the cascade and placed on both sides of the fully instrumented center blade (cf. Table 2a). In the discussion that follows, reference will be made to the two suction surface locations as 0.012U and 0.062U, and to the pressure surface location as 0.012L. Data presented in this report will be limited to a typical set, and the reader will be referred to the listed results in Ref. 8 for more detail.

Of the twelve possible combinations of incidence angle, pitching amplitude, and reduced frequency, only four will be discussed in detail. A survey of all results has shown that the data vary only superficially with reduced frequency (for the range tested) and only the k = 0.151 conditions have been selected for display. Figures 13 through 16 and 17 through 20 contain gapwise distributions of pressure amplitudes and pressure phase angles, respectively, for all incidence angles and amplitudes. Each figure has results for all interblade phase angles, and within each panel the two suction surface measurements are depicted by solid symbols (circle for 0.012U and triangle for 0.062U) and the pressure surface measurement by the open square (for 0.012L). In each case only the first harmonic component is plotted.

Figures 13 and 14 show the gapwise pressure amplitudes for 2 ± 0.5 deg and 2 ± 2 deg to be relatively level. This is particularly true for 0.062U in both plots, and less true for 0.012L in Fig. 14. For the suction surface leading edge station (0.012U), the measured results are level in both figures, with more scatter evident in Fig. 14 than in Fig. 13. No significant departures from these results are observed at the two lower frequencies (cf. Ref. 8). A systematic (but preliminary) study of the possible causes for the scatter in Fig. 14 was inconclusive, and is briefly discussed in Appendix 2. In general, these results show the cascade to be acceptably periodic in pressure amplitude response for both pitching amplitudes at α_{MCL} = 2 deg.

The situation is somewhat altered for α_{MCL} = 6 deg in Figs. 15 and 16. For both amplitudes the second suction surface station (0.062U) is still level, indicating good periodicity, and the pressure surface station (0.012L) is generally level with only mild deviations from completely periodic behavior. However, at 0.012U there are strong gapwise gradients in Fig. 15 for 6 ± 0.5 deg, which are reversed and somewhat scattered, but still strong in Fig. 16 for 6 ± 2 deg. This would suggest a significant loss in leading edge periodicity at α_{MCL} = 6 deg, but a recovery to periodic behavior within 5 percent of the chord aft of the leading edge. Once again, little change is evident for the other two reduced frequencies. It is probable that this reduced periodicity near the leading edge is associated with the increase in cascade loading.

BEST DOCUMENT AVAILABLE

Figures 17 and 18 are plots of the gapwise distribution of first harmonic pressure phase angle measured at each of the three blade stations for 2± 0.5 deg and 2± 2 deg. (Note that 0.012U and 0.062U are referred to the left scale and 0.012L to the right scale.) The phase angle for any blade is referenced to the motion of blade n by the procedure derived in Appendix 1. Thus, once again a flat distribution signifies good periodicity. With the exception of the results for $\sigma = 0$ deg, the distributions are essentially flat, with the best periodicity indicated by the distributions in Fig. 18 for 2 ± 2 deg. The gapwise phase gradient for $\sigma = 0$ deg may be associated with the so-called acoustical resonance phenomenon which occurs near $\sigma = 0$ deg for the test conditions of this experiment. This is discussed briefly in Appendix 3.

When these data are compared with data for the two lower frequencies (cf. Ref. 8) it is found that there is virtually no change for 2 ± 2 deg at all frequencies. There is also little change for 2 ± 0.5 deg at $k = 0.122$, but there is an appreciable increase in the scatter for $k = 0.072$. A plausible explanation for this is as follows. If there is a constant level of noise in the measured signal associated with background wind tunnel disturbances, it will form a larger portion of the $\bar{\alpha} = 0.5$ deg data than of the $\bar{\alpha} = 2$ deg data. Hence, the $\bar{\alpha} = 2$ deg data will have less scatter on this basis. Also, the lower frequency data is processed over fewer cycles than the higher frequency data because of the fixed memory and constant acquisition rate used (cf. Table 4). Consequently, non-coherent signals will have less influence on higher frequency data and the $k = 0.122$ and 0.151 data will have less scatter than the data for $k = 0.072$.

Similar trends are observed for 6 ± 0.5 deg and 6 ± 2 deg in Figs. 19 and 20, with greater scatter at ± 0.5 deg than at ± 2 deg, strong gapwise gradients for $\sigma = 0$ deg, and a generally level behavior elsewhere. As before, recourse to the data in Ref. 8 shows that the scatter tends to increase at the lower frequencies at ± 0.5 deg, with less tendency to do so at ± 2 deg.

Overall, this experiment has shown that the cascade blade response in its present configuration is periodic at the lowest load condition ($\alpha_{MCL} = 2$ deg) for most parameter values tested but has a gapwise gradient in phase angle at $\sigma = 0$ deg. Further, there is a significant gapwise gradient in magnitude at the airfoil leading edge over a wide range of σ at the modest load condition ($\alpha_{MCL} = 6$ deg), but within 5 percent of the chord aft of the leading edge the amplitude response is again periodic. Phase periodicity for $\alpha_{MCL} = 6$ deg is comparable to that for the low load condition. Thus, for these two load conditions the measured data satisfy the periodicity condition over most of the operating ranges and over most of the blade leading edge region, lending credence to the belief that the unsteady data obtained in this experiment are valid data. This belief is considerably strengthened below when the data are compared with theory.

BEST DOCUMENT AVAILABLE

Aerodynamic Damping and Stability

The most direct, global parameter that can be obtained from the unsteady pressure distributions over the entire blade chord is the aerodynamic damping parameter, Ξ. This is shown in Appendix 1 to be equal and opposite to the quadrature (or out of phase) component of the pitching moment coefficient per unit amplitude, and represents a measure of system stability in single degree of freedom torsional flutter (i.e., a system is stable if $\Xi > 0$). It has been measured and reported on many times for the current cascade model (Refs. 1-4) and certain of these past results are available for comparison with those of the current test.

All of the aerodynamic damping parameter values for this test have been extracted from Ref. 8, are listed in Table 5, and are plotted in various forms in Figs. 21 through 24. In the first three figures Ξ is plotted versus σ, and each panel represents either $\alpha_{MCL} = 2$ or 6 deg, with amplitudes of $\bar{\alpha} =$ 0.5 or 2 deg represented within each panel by open circles or triangles, respectively. In addition, data from Ref. 4 for $\alpha = 6 \pm 2$ deg, represented by solid triangles, are included in the right hand panel of each of these figures, and in Fig. 21 a theoretical plot for a flat plate airfoil (from Ref. 4, based on the theory of Smith in Ref. 10) is included for comparison with the data.

Gross trends are similar for all plots. Damping increases with σ over the ranges $45 < \sigma < 180$ and $-180 < \sigma < -45$ deg, and decreases sharply for $-45 < \sigma < 45$ deg. The crossover from stable to unstable damping with increasing σ occurs at $\sigma > 0$, and from unstable to stable damping at $\sigma < 180$ deg. (Note that $\sigma = +180$ deg and $\sigma = -180$ deg are actually the same point, and that damping trends over σ through this common point are continuous.) No significant trends with amplitude are discernable in any plot, although the effects of amplitude appear to be smaller for $\alpha_{MCL} = 6$ deg (right panels of Figs. 21-23) than for $\alpha_{MCL} = 2$ deg.

The agreement between current and previous (Ref. 4) damping data for $\alpha = 6 \pm 2$ deg (open and closed triangular symbols, respectively, in right hand panels of Figs. 21-23) is very good. Not only are trends strongly corroborated, but close agreement between damping measurements at common values of σ is seen to exist, confirming the ability of the OCWT to provide self-consistent, repeatable data from tests run at different times. The single plot of Smith's theory for the flat plate (Ref. 10) is included to show the general trend agreement with data, but also to point up the sharp disagreement between flat plate theory and experiment in the absolute value of the damping parameter. The significance of this will become clear later when experimental pressure data are compared with both flat plate theory and with a more advanced theory embodying actual blade shape in its formulation.

BEST DOCUMENT AVAILABLE

Figure 24 is an alternative view of the data in Fig. 22, but with incidence angle as the parameter of comparison within each panel. Here it is seen that increased incidence angle has a mitigating effect on the maximum and minimum values of Ξ attained; i.e., there is a greater excursion from maximum damping to minimum damping for $\alpha_{MCL} = 2$ deg than for $\alpha_{MCL} = 6$ deg.

Chordwise Distributions

The aerodynamic damping and stability calculations described above are obtained by integrating the chordwise pressure distributions on the center airfoil. Hence, it is useful to examine these distributions with the object of relating the observed changes from case to case, to changes in the measured damping of the previous section.

There are essentially two sets of parameter variations to be discussed here: first, the effects of varying σ over the entire range for a single incidence angle and pitching amplitude combination and for constant frequency, and second, the effects of varying both incidence and pitching amplitude for two equal and opposite values of σ, again at constant frequency. (A study of the results tabulated in Ref. 8 shows only minor trend changes with k for the range tested here.) For each of these parameter sets the data are first presented in terms of the real and imaginary parts, and then presented in terms of amplitude and phase angle, all plotted versus chord fraction. For all cases discussed in this section only the chordwise pressure difference will be studied.

In Fig. 25 the real (circles) and imaginary (triangles) parts of the pressure difference coefficient are plotted versus chord fraction. The eight panels shown represent the eight values of σ, ranging from $\sigma = -135$ deg at the upper left to $\sigma = 180$ deg at the lower right. In this figure $\alpha = 2 \pm 0.5$ deg and $k = 0.072$. Two things are to be noted here: the significant change in the relationship between real and imaginary parts as σ becomes greater than 0 deg and again as σ reaches 180 deg, and the wide variation of leading edge values of both real and imaginary parts as σ varies. Over the range $-180 < \sigma < 0$ deg the real part at the leading edge is a large positive number and the imaginary part is a modest-to-large negative number. The real part is still positive over the remaining range of σ, but now the imaginary part is also positive. These changes affect the response phase angle, which was shown earlier (Ref. 4) to have a dominant effect on stability.

BEST DOCUMENT AVAILABLE

Figure 26 has the same display format as Fig. 25, but now the plotted points represent the magnitude of the pressure difference coefficient (circles) and the pressure difference phase angle (triangles). These quantities are referenced to the left and right hand ordinate scales, respectively. (The prominent horizontal tic marks denote the $\phi_{\Delta p} = 0$ level.) It is seen that over the range $-180 < \sigma < 0$ deg the combination of real and imaginary parts from Fig. 25 yield a negative response phase angle over the forward portion of the blade. Here the pressure difference response lags the motion, and according to the results in Ref. 4, this motion is stable, as confirmed by the plots in Fig. 21. Conversely, over the remaining range of σ the pressure response leads the motion and the resulting motion is unstable. It should be noted that this simplistic view of stability based on the leading edge pressure phase angle is possible only because the pressure difference near the leading edge is many times greater than the pressure difference elsewhere on the blade. The only accurate measure of stability is obtained from the computation of work per cycle or of aerodynamic damping (cf. Appendix 1).

Two interblade phase angles, $\sigma = \pm 45$ deg, have been selected to display the effects of incidence angle and pitching amplitude on the unsteady pressure distribution for constant reduced frequency. Real and imaginary parts are plotted in Fig. 27, and amplitude and phase angle in Fig. 28, providing parallel comparisons with Figs. 25 and 26, respectively. The most striking observation to be made here is the apparent lack of variation for σ held constant (i.e., across each row of panels). The differences that do become evident are subtle and are concentrated near the leading edge. For example, the absolute value of the real and imaginary parts, or the amplitude of the pressure difference magnitude, increases with pitching amplitude for constant incidence angle. A mixed behavior with incidence occurs, with all of these quantities decreasing with incidence at $\bar{\alpha} = 0.5$ deg, and with no specific trend at $\bar{\alpha} = 2$ deg. Except for minor data scatter, the phase angle distributions are virtually the same for each σ. Thus, the observation made in Ref. 4, that the dominant parameter affecting stability is the interblade phase angle, is reiterated here. Furthermore, the major effect of the leading edge response noted in Ref. 1 is confirmed by the present study, in which minor changes in stability parameter levels are controlled by changes in leading edge parameter values.

An examination of the tabulations in Ref. 8 will reveal that 10 harmonics are listed for each measuring station for every run and point. Individual surface responses are presented as well as the differences that are used in computing loads and stability values. A further examination of these results

BEST DOCUMENT AVAILABLE

will show that significantly higher harmonic levels were encountered at $\bar{\alpha}$ = 0.5 deg than at $\bar{\alpha}$ = 2 deg. It is shown in Appendix 4 that these higher harmonic responses were probably associated with longitudinal wind tunnel disturbance waves affecting both surfaces equally, and that their effects disappeared on taking the pressure differences used in computing loads.

Comparison With Theory

Selected cases from these experimental results were chosen for comparison with the unsteady theory of Verdon and Caspar (Ref. 11) for a blade having non-zero thickness and camber, operating in a subsonic, compressible flow. The basis of this theory is the unsteady perturbation of the potential function about the steady-state condition. Hence it was necessary as an initial step to match the steady theory to the measured steady-state pressures. In the following comparisons this is the only adjustment made to produce agreement between theory and experiment.

Comparisons were made at both incidence angles tested, but were restricted to a single value of k = 0.122. At α_{MCL} = 2 deg the data and theory were compared at four values of interblade phase angle, σ = ± 45 and ± 135 deg, and at α_{MCL} = 6 deg only the data at σ = -45 and -135 deg were compared with theory. The initial steady potential flow was adjusted to the data for best fit at α_{THEORY} = -0.27 and 2.23 deg, corresponding to α_{MCL} = 2 and 6 deg, respectively. Plots showing the matched steady-state agreement for these two cases are shown in Fig. 29, in which the experimental distributions are the same as in Fig. 10. These and the following unsteady distributions have been inverted to conform to the computer-generated plots from the theory. It is seen that, within the scope of the present study, which was largely exploratory, a good match between steady theory and experiment has been achieved. It is not unusual for incidence angle discrepancies to occur between theory and experiment in making such a match because 1) the experimental cascade is finite in extent while the theory represents an infinite cascade, and 2) no provision was made for adjusting the results for downstream diffusion associated with the presence of sidewalls and their growing boundary layers. These and other factors could have been refined for a better match in flow geometry, but such an effort would have been contrary to the needs of the present study.

In Fig. 30 the real and imaginary parts (circles and squares) of the measured unsteady pressure difference coefficient for α = 2 ± 0.5 deg are compared with the Verdon/Caspar "real blade" theory (solid lines) and the flat plate version of this theory (dashed lines) at σ = ± 45, ± 135 deg. In all cases except σ = 45 deg the agreement of the data with the Verdon/Caspar real blade theory is better than with flat plate theory, and without exception the agreement with

BEST DOCUMENT AVAILABLE

Verdon/Caspar theory is excellent. At this incidence angle no distinction can be made between the data for the two separate amplitudes since they too are in nearly perfect agreement, and of course, the normalized theoretical values for the two amplitudes are identical.

In Fig. 31 the theory and experiment for α_{MCL} = 6 deg are compared at σ = -135 and -45 deg in the left and right panels, respectively. Here the experimental distributions have measurable differences at their leading edges, so the upper and lower panels are for $\bar{\alpha}$ = 0.5 and 2 deg. As before, the real blade theory is independent of amplitude and is the same for upper and lower panels at each σ. Furthermore, the flat plate theory is independent of incidence so the plots in Fig. 31 are identical to those in Fig. 30 for σ = -135, -45 deg. Once again the agreement between real blade theory and the measured results is excellent, and this more complete theory is shown to be superior to the flat plate theory.*

It is recognized that within the scope of this study, only a small sample of the measured data could be compared with theory. Nevertheless, within this limited survey, two major facts emerge clearly: 1) the real blade theory, when once adjusted to the steady load distribution, is consistently in excellent agreement with the measured unsteady results, and 2) the flat plate theory is shown to be useful in supplying trend information, but in most cases is inadequate to predict the details of unsteady loading. It should be noted that this inability of the flat plate theory to predict integrated load results is evident in Fig. 21 and in the several comparable figures in Ref. 4 for aerodynamic damping. Although no aerodynamic damping predictions from the real blade theory were available for inclusion here, the consistent agreement of unsteady pressure distribution with this theory would lead to an expectation of agreement in damping also.

Intergap Sidewall Variations

Unsteady sidewall pressure measurements were made along the leading edge plane between blades 6 and 7, with slight overlaps into adjacent passages. The geometric setup is shown in Fig. 8 and pertinent transducer locations in gap fraction, η, relative to blade 6 suction surface are given in Tables 2 and 3. These data were obtained to give some insight into the unsteady "far field" behavior of an oscillating cascaded airfoil. Although data were taken for every parameter variation of the test program, this portion of the test was meant to be exploratory in nature and was largely outside the scope of the main program. Only a few cases have been analyzed in this study, although all of the data are available in Ref. 8.

---

* The small deviation in the real part of the Verdon/Caspar theory near the trailing edge appears to be caused by the difficulty of accurately capturing the singular behavior in unsteady pressure at a sharp trailing edge with a finite difference approximation.

BEST DOCUMENT AVAILABLE

This brief analysis of the unsteady sidewall pressures is restricted to a few selected plots of first harmonic pressure coefficient amplitude and phase angle. The amplitude variation is straightforward and involves nothing more than a compilation of amplitude data from consecutive Mode 1, Mode 2 printouts found in Ref. 8. Interpretation of the phase angle data requires a simple transformation. By definition, an interblade phase angle of σ implies that the response of blade n+1 leads that of blade n by σ, and it is reasonable to assume that any point in the free field surrounding each blade is similarly out of phase by σ relative to the same point in the free field of the appropriate adjacent blade. For simplicity, the assumption is made here that the intergap response phase angle can be adjusted by a linear intergap variation with σ to achieve periodicity. In other words, since all data are referenced to blade 6 by the data reduction procedure, and η is measured from blade 6, then if ϕ_{s1} is the local first harmonic sidewall phase angle, an adjusted value may be computed from $\phi^*_{s1} = \phi \quad \eta\sigma$.

The intergap variation of pressure magnitude and adjusted phase angle is plotted in Figs. 32 and 33 for a single value of k = 0.151 and for α_{MCL} = 2 and 6 deg, respectively. Data for $\bar{\alpha}$ = 0.5 and 2 deg are represented by circles and triangles. Open symbols denote data plotted at the measurement point and solid symbols denote data artificially transferred by one gap from the measurement point. Superficially both sets of data have the same general behavior. Pressure amplitude rises sharply as a blade is crossed from pressure to suction surface, and then decays across the gap. From the well correlated behavior of $\bar{C}_{ps_1}$ for both amplitudes within each figure, and the definition of Eq. (1), it appears that the measured static pressure in the free field varies directly with $\bar{\alpha}$. There is also a sharp change in adjusted phase angle across the blade, with a nearly linear rise in ϕ^*_{s1} as the gap is traversed. It would appear that the linear gapwise adjustment in phase angle is valid, although there is some scatter in the data.

Significant differences are apparent between the two figures. The jump in magnitude across the blade is larger for α_{MCL} = 6 deg than for 2 deg, which would imply that the free field perturbation also varies with steady blade loading. Similarly, the phase change across the blade is also larger for α_{MCL} = 6 deg than for 2 deg.

Examination of the remaining sidewall data tabulated in Ref. 8 shows that similar amplitude behavior is seen for all interblade phase angles and that similar phase behavior is seen for all negative interblade phase angles. Furthermore, positive interblade phase angles produce a reversal in the slope of the response phase angle variation. It is obvious that this limited exposure to the sidewall data is insufficient to do more than lead to some initial speculations. Clearly, a deeper study of the available data in Ref. 8 is required and should be undertaken, together with a theoretical study of the free field using the analysis of Ref. 11 for further comparison and validation of the theory.

BEST DOCUMENT AVAILABLE

Additional Comparisons

The observed changes in pressure levels with σ in Figs. 13-16 and in pressure phase angle with σ in Figs. 17-20 suggests a systematic variation with σ that is borne out in Fig. 34. The data points are taken from the 2 ± 2 deg, k = 0.151 case at χ = 0.012U and clearly show a symmetric pressure amplitude and skew-symmetric phase angle behavior relative to either σ = 0 or 180 deg. These results are typical, and a spot check of the data in Ref. 8 shows a consistent pattern emerging for virtually all other cases. (Indeed, a casual examination of Figs. 13-20 confirms this behavior for virtually all cases.)

Also displayed in Fig. 34 are solid lines denoted as "fitted theory." An oscillating aperture analysis has been performed in Ref. 12 in which the two sides of a two-dimensional opening oscillate sinusoidally with a phase shift, σ, between their motions, in the presence of a fluid stream. A velocity perturbation analysis is performed from which a perturbation pressure field can be inferred, having the form $\bar{C}_p = A + B\sqrt{2-2\cos\sigma}$. A and B are free constants by virtue of the lack of specificity in this simplified formulation. This theory is fitted to the experimental data by evaluating A and B such that the curve passes through the measured values at σ = 0 and 180 deg. The resulting excellent agreement between fitted theory and measured data leads to the obvious conclusion that the observed σ-variations in the measured data are directly related to the geometric constraints of the inlet aperture. Several comparable examples of this type of two-point fitted agreement are included in Ref. 12.

The phase "agreement" shown in the lower panel of Fig. 34 is necessarily contrived, primarily to allow both measured and theoretical results to coexist on the same plot. The data are referred to the left ordinate and the theory to the right ordinate, and because this is phase information, dependent on the ratio of real and imaginary quantities, no free constants exist. Nevertheless, both phase variations have the same continuous and (nearly) linear behavior across σ = ± 180 deg and both exhibit a strong positive jump at σ = 0 deg. Again there is strong evidence that unsteady aperture geometry is an important factor in real blade response.

Further corroboration of this type of behavior is seen in the results of an unsteady turbine cascade experiment described in Ref. 13 and elaborated on in Ref. 14. This experiment was conducted on a cascade configuration that is significantly different from the subject of this report: turbine blades, 20 percent thick, with 112 deg turning at an inlet Mach number of 0.52, versus compressor blades, 6 percent thick, with 10 deg turning, at an inlet Mach number

BEST DOCUMENT AVAILABLE

of 0.18. The pressure amplitude, plotted versus σ in Fig. 17 of Ref. 13 for an aft station on the blade, or in Fig. 44 of Ref. 14 for a forward station on the blade, has substantially the same form as the result in the upper panel of Fig. 34. In addition, the phase angle behavior in Fig. 18 of Ref. 13 or in Figs. 52-54 of Ref. 14 is similar to the result in the lower panel of Fig. 34. Here the comparison is more difficult to make by virtue of differences in several of the defining parameters of the turbine and compressor cascades. Nevertheless, the general pattern of agreement between these two sets of data is further evidence of a strong geometric interaction controlling the leading edge aerodynamics.

BEST DOCUMENT AVAILABLE

CONCLUSIONS AND OBSERVATIONS

Preliminary Remarks

This investigation is the latest in a series of tests of oscillating blades in cascade conducted at UTRC. While the previous tests focused separately on individual phenomena such as aerodynamic damping or surface pressure response, the current test has concentrated on several items, making it one of the most comprehensive and self-consistent unsteady aerodynamic cascade experiments known to date. Specifically, it is believed that this experiment has examined, in detail, unsteady cascade periodicity for the first time. In addition, it has confirmed the previous tentative results for aerodynamic damping, has shown self-consistency and agreement in overall cascade performance, has provided verification of a "real blade" unsteady aerodynamic theory, and has produced a large body of unsteady aerodynamic data for future study.

In this section are listed a set of conclusions reached and observations made in the course of this study. They are segregated below in two groups, comprising the primary and secondary findings of the experiment. Within each group they are enumerated in the approximate order of their appearance in the text.

Primary Findings

1. In general, for the two load conditions tested, the measured data satisfy the periodicity condition over most of the operating ranges and over most of the blade leading edge region. Specific observations follow below:

   a) The cascade is periodic in pressure amplitude response at all measuring stations for both pitching amplitudes tested at $\alpha_{MCL} = 2$ deg.

   b) Pressure amplitude periodicity deteriorates somewhat at $\alpha_{MCL} = 6$ deg at the leading edge station, but returns to periodic behavior within 5 percent of the chord aft of the leading edge.

   c) Pressure phase angle is periodic at all incidence angles and all amplitudes of motion, with the exception of the condition $\sigma = 0$ deg where a strong gapwise gradient is observed. This is believed to be associated with a cascade acoustical resonance condition.

2. In confirmation of the results of previous tests, interblade phase angle, σ, is still the most important parameter affecting the stability of oscillating cascaded airfoils.

BEST DOCUMENT AVAILABLE

3. In comparing the measured chordwise pressure distribution with the unsteady theory for a thick, cambered, cascaded airfoil, the agreement was consistently excellent for both incidence angles tested.

4. The same comparison with flat plate theory showed similar trends but, in general, was only in fair agreement when judged relative to the "real blade" theory.

Secondary Findings

5. Steady state measurements of cascade pressure rise, flow turning, and total pressure loss are in agreement with previous tests and with predicted minimum loss.

6. Aerodynamic damping increases monotonically with σ over the range $45 < \sigma < 315$ deg (or equivalently over the contiguous ranges $45 < \sigma < 180$ and $-180 < \sigma < -45$ deg). It decreases sharply over the range $-45 < \sigma < 45$ deg.

7. The crossover from stable to unstable aerodynamic damping with increasing σ occurs at $\sigma > 0$ deg and from unstable to stable at $\sigma < 180$ deg for the parameter ranges tested.

8. Also for the parameter ranges tested, no significant damping trends with amplitude are discernable.

9. Agreement between current and previously measured aerodynamic damping data for $\alpha = 6 \pm 2$ deg is very good.

10. Comparison between current aerodynamic damping data and the damping prediction from the Smith flat plate theory shows trend agreement as before, but disagrees in the absolute values of the parameters.

11. Increased incidence angle has a mitigating effect on the maximum and minimum values of aerodynamic damping attained; i.e., there is a greater excursion from maximum to minimum damping for $\alpha_{MCL} = 2$ deg than for 6 deg.

12. Chordwise pressure distributions are relatively unaffected by changes in reduced frequency for the range tested.

13. The effect of σ on chordwise pressure is to change the response phase angle near the leading edge from lag (in the stable regime for $-180 < \sigma < 0$ deg) to lead (in the unstable regime for $0 < \sigma < 180$ deg).

14. The pressure difference near the leading edge is many times greater than the pressure difference aft of the leading edge, confirming observations from previous studies.

BEST DOCUMENT AVAILABLE

15. Only minor changes in the pressure distributions are observed with variations in α_{MCL}, $\bar{\alpha}$, and k for constant σ over the ranges tested.

16. Sidewall intergap pressure magnitude rises sharply as a blade is crossed from pressure to suction surface, and then decays across the gap. In general its behavior is periodic.

17. The sidewall pressure magnitude is everywhere proportional to $\bar{\alpha}$; its peak value increases with steady blade loading.

18. The sidewall intergap pressure phase angle varies monotonically across the gap and readjusts abruptly across the blade. In general its behavior is periodic.

19. A comparison of the leading edge pressure magnitude variation with σ and a two-point "fitted theory" for an oscillating aperture shows excellent agreement. This agreement suggests that the observed σ-variations in the measured data are directly related to the geometric constraints of the inlet aperture.

20. A similar comparison of measured and predicted phase angle variation with σ leads to the same conclusion.

21. This suggested dependence on inlet geometry is further corroborated by a qualitative comparison with results from a turbine experiment cited in the text.

BEST DOCUMENT AVAILABLE

BLANK PAGE

APPENDIX 1

DERIVATION OF RELEVANT EQUATIONS

For convenience this Appendix is devoted to the derivations of the major equations used in the text. Although these equations represent standard concepts and most have been derived elsewhere, there is sufficient subtlety in their definitions and use to warrant their collection in this Appendix. It should be noted that all unsteady aerodynamic loads have an implicit normalization with respect to the pitching amplitude, $\bar{\alpha}$, in accordance with the definition of unsteady pressure coefficient from Eq. (1),

$$Cp\ (\chi,t) = \frac{p\ (\chi,t)}{q\ \bar{\alpha}} \tag{1}$$

If blade 6 (the center reference blade) is the only one under consideration, no distinctive notation will be used, and the pressure coefficient in Eq. (1) can be expressed in either complex exponential form or in component form as

$$\begin{aligned} C_p(\chi,t) &= \bar{C}_p(\chi)e^{i\left(\omega t + \phi_p(\chi)\right)} \\ &= \left(C_{p_R}(\chi) + iC_{p_I}(\chi)\right)\ e^{i\omega t} \end{aligned} \tag{2}$$

(If however, any other of the n blades are being considered, a superscript notation denoting the specific blade will be employed. This will be demonstrated later.) The subscripts R and I denote the so-called real and imaginary components of C_p, but physically can be interpreted as the components of the pressure response that are in phase and out of phase with respect to the motion,

$$\alpha(t) = \bar{\alpha}e^{i\omega t} \tag{3}$$

In terms of the amplitude and phase angle,

$$\left.\begin{aligned} C_{p_R}(\chi) &= \bar{C}_p(\chi)\ \cos\phi_p(\chi) \\ C_{p_I}(\chi) &= \bar{C}_p(\chi)\ \sin\phi_p(\chi) \\ \bar{C}_p(\chi) &= \sqrt{C_{p_R}^2(\chi) + C_{p_I}^2(\chi)} \\ \phi_p(\chi) &= \tan^{-1}\left(C_{p_I}(\chi)/C_{p_R}(\chi)\right) \end{aligned}\right\} \tag{4}$$

BEST DOCUMENT AVAILABLE

where $\phi_p(\chi)$, as defined here, is positive for the pressure leading the motion. Similar relationships involving in and out of phase components and their amplitudes and phase angles will exist for all other quantities, but for brevity will not be repeated here.

The pressure difference, ΔC_p, will be an important quantity, and will be obtained from the difference between the pressures on the upper (or suction) and lower (or pressure) surfaces, denoted by subscripts U and L. Thus,

$$\Delta C_p(\chi,t) \equiv - \left| C_{p_U}(\chi,t) - C_{p_L}(\chi,t) \right| \tag{5}$$

It should be noted that only components, and not magnitudes or phase angles, can be differenced, or

$$\Delta C_p(\chi,t) = \left(\Delta C_{p_R}(\chi) + i\Delta C_{p_I}(\chi) \right) e^{i\omega t} \tag{6}$$

where

$$\Delta C_{p_R}(\chi) = - \left(C_{p_{UR}}(\chi) - C_{p_{LR}}(\chi) \right) \tag{7}$$

Another expression for Eq. (6), illustrating the notation for the phase angle of the pressure difference, is

$$\Delta C_p(\chi,t) = \Delta \bar{C}_p(\chi)\, e^{i\left(\omega t + \phi_{\Delta p}(\chi)\right)} \tag{8}$$

For a continuous distribution of the pressure over the entire blade surface the unsteady normal force and unsteady pitching moment coefficients per unit amplitude about the airfoil pivot axis at χ_p are given by

BEST DOCUMENT AVAILABLE

$$C_N(t) = \int_0^1 \Delta C_p(\chi,t)d\chi \tag{9}$$

$$C_M(t) = \int_0^1 (\chi_p - \chi)\ \Delta C_p(\chi,t)\ d\chi \tag{10}$$

(where the phase lead angles associated with $\bar{C}_N$ and $\bar{C}_M$ are denoted by ϕ_N and ϕ_M, respectively). However, in this experiment a discrete array of transducers was used, necessitating a numerical integration of the pressures. As in earlier OCWT experiments (Refs. 1-4) a ten point Gaussian quadrature was performed over the forward 91 percent of the chord, and a three point interpolation through the data at $\chi = 0.86$, 0.91, and through $\Delta C_p(1.0) = 0.0$ at the trailing edge was used to complete the integration. For convenience, this procedure will be summarized below.

The usual Gaussian integration formula for the area under $f(\xi)$ over the interval $0 \leq \xi \leq 1$ is

$$A = \int_0^1 f(\xi)d\xi \approx \sum_{j=1}^{J} W_j f(\xi_j) \qquad (0 \leq \xi \leq 1) \tag{11}$$

where the W_j are integration weighting coefficients. For a conventional ten point Gaussian integration, the measuring stations, ξ_j, are prescribed by the locations of the zeroes of the 10th degree Legendre polynomials over the interval $0 \leq \xi \leq 1$ (cf. Refs. 15, 16). It is seen from the values of ξ_j listed in Table 6 that for normal trailing edge thickness distributions, insertion of a transducer at the 10th station ($\xi_{10} = 0.987$) would be physically impossible. Hence, it was decided to place the rearmost transducer at $\chi = 0.91$ and rewrite Eq. (11) as an integration over two regions,

$$A = \int_0^z f(\chi)d\chi + \int_z^1 f(\chi)d\chi \tag{12}$$

BEST DOCUMENT AVAILABLE

The transformation

$$\chi = z\zeta \tag{13}$$

in the first integral yields

$$A = z\int_0^1 f(\xi)d\xi + \int_z^1 f(\chi)d\chi$$

and use of Eq. (11) yields

$$A = z\sum_{j=1}^{J} W_j f(\xi_j) + \int_z^1 f(\chi)d\chi \tag{14}$$

At the 10th station, $\chi_{10} = 0.91$ by construction and $\xi_{10} = 0.986954$ from Table 6, hence $z = 0.92203$. Table 6 also contains lists of weighting coefficients, W_j, and physical coordinates, χ_j. The actual numerical integrations were carried out by replacing $f(\xi)$ by the appropriate quantity to be integrated, both in the Gaussian sum and in the three-point interpolation integral to the trailing edge.

System stability is obtained from a computation of the work per cycle, and its conversion to an aerodynamic damping parameter. The general form of the work coefficient is given by

$$C_W = \oint \mathrm{Re}\left\{\bar{\alpha}\, C_M(t)\right\} d\alpha_R \tag{15}$$

(In this formula the previously normalized $C_M(t)$ is multiplied by the normalizing pitching amplitude, $\bar{\alpha}$, to express the work coefficient in its conventional form). For a pure sinusoidal moment response,

$$\begin{aligned}\mathrm{Re}\left\{\bar{\alpha}\, C_M(t)\right\} &= \bar{\alpha}\,\mathrm{Re}\left\{\bar{C}_M\, e^{i(\omega t + \phi_M)}\right\} \\ &= \bar{\alpha}\,\bar{C}_M \cos\left(\omega t + \phi_M\right)\end{aligned} \tag{16}$$

BEST DOCUMENT AVAILABLE

From Eq. (3),

$$\alpha_R = \bar{\alpha} \cos\omega t$$

$$d\alpha_R = -\bar{\alpha} \sin\omega d(\omega t) \tag{17}$$

and substitution into Eq. (15) ultimately yields

$$C_N = \pi\bar{\alpha}^{-2} \bar{C}_M \sin \phi_M \tag{18}$$

From Refs. 1-4, the aerodynamic damping parameter is defined by

$$\Xi = - C_N / \pi\bar{\alpha}^{-2} \tag{19}$$

and hence, from Eq. (18),

$$\Xi = - \bar{C}_M \sin \phi_M = - C_{M_I} \tag{20}$$

(Note that this result differs in form from the results in Refs. 1-4 because the C_M in these equations is implicitly normalized with respect to $\bar{\alpha}$).

In the more general case, the response will not be a pure sinusoid, but will contain higher harmonics as well. Accordingly, in the present experiment the time histories of all response functions were decomposed into their harmonics by conventional techniques. In the analysis that follows, only the time-varying portion of the signal will be considered, and the steady component will be ignored. This is in keeping with procedures employed in the experiment in which ac coupling was employed that automatically removed the steady state portion of any signal.

BEST DOCUMENT AVAILABLE

A general notation will now be introduced, applicable to any of the several coefficients being analyzed. If $F(\omega t)$ is some periodic function of ωt, then its unsteady part can be represented by

$$F(\omega t) = \sum_{k=1}^{\infty} \bar{F}_k \, e^{i\left(k\omega t + \phi_j\right)} \tag{21}$$

where ϕ_k is the phase lead of the kth harmonic relative to the motion. This may be rewritten as

$$\begin{aligned} F(\omega t) &= \sum_{k=1}^{\infty} \bar{F}_k \, e^{i\phi_k} e^{ik\omega t} \\ &= \sum_{k=1}^{\infty} \left(\bar{F}_k \cos \phi_k + i\bar{F}_k \sin \phi_k\right) e^{ik\omega t} \\ &= \sum_{k=1}^{\infty} \left(F_{kR} + iF_{kI}\right) e^{ik\omega t} \end{aligned} \tag{22}$$

so, by definition,

$$\left.\begin{aligned} F_{kR} &= \bar{F}_k \cos \phi_k \\ F_{kI} &= \bar{F}_k \sin \phi_k \\ \bar{F}_k &= \sqrt{F_{kR}^2 + F_{kI}^2} \\ \phi_k &= \tan^{-1}\left(F_{kI} \,/\, F_{kR}\right) \end{aligned}\right\} \tag{23}$$

which is parallel in every way to Eq. (4). Hence, for any unsteady pressure,

$$C_p(\chi,t) = \sum_{k=1}^{\infty} \bar{C}_{p_k} \, e^{i\left(k\omega t + \phi_{pk}\right)} \tag{24}$$

where the individual components are now given by

BEST DOCUMENT AVAILABLE

$$C_{p_{kR}} = \bar{C}_{pk} \cos \phi_{pk}$$

$$C_{pkI} = \bar{C}_{pk} \sin \phi_{pk} \tag{25}$$

Similarly, for C_N and C_M,

$$C_N(t) = \sum_{k=1}^{\infty} \bar{C}_{Nk} e^{i\left(k\omega t + \phi_{Nk}\right)} \tag{26}$$

$$C_M(t) = \sum_{k=1}^{\infty} \bar{C}_{Mk} e^{i\left(k\omega t + \phi_{Mk}\right)} \tag{27}$$

Insert this last equation into Eq. (15) to compute work per cycle of the generalized moment response. The result is

$$\begin{aligned} C_W &= \oint R_e \left\{ \bar{\alpha} \sum_{k=1}^{\infty} \bar{C}_{Mk} e^{i\left(k\omega t + \phi_{Mk}\right)} \right\} d\alpha_R \\ &= \oint \bar{\alpha} \sum_{k=1}^{\infty} \bar{C}_{Mk} \cos\left(k\omega t + \phi_{Mk}\right) \left[-\bar{\alpha} \sin\omega t d(\omega t)\right] \\ &= -\bar{\alpha}^2 \sum_{k=1}^{\infty} \bar{C}_{Mk} \oint \cos\left(k\omega t + \phi_{Mk}\right) \sin\omega t d(\omega t) \end{aligned} \tag{28}$$

and by orthogonality it is easily shown that only the first harmonic term, $k = 1$, survives. Hence, in general,

$$C_W = \pi \bar{\alpha}^2 \bar{C}_{M1} \sin \phi_{M1} \tag{29}$$

BEST DOCUMENT AVAILABLE

and Eq. (20) becomes

$$\Xi = - \bar{C}_{M1} \sin \phi_{M1} = - C_{MI_1} \tag{30}$$

Finally, as noted in the main text of this report, unsteady blade-to-blade periodicity along the cascade leading edge plane is best evaluated by examining the gapwise distribution of pressure coefficient (both amplitude and phase angle) for common transducer locations. To facilitate this a superscript notation has been adopted to denote blade number (i.e., $\bar{C}_p^{(n)}(\chi)$ and $\phi_p^{(n)}(\chi)$ for amplitude and phase angle of blade n at chordwise station χ). Normally, a single chordwise location will be examined at any one time, so the functional dependence on χ will be dropped for notational simplicity.

Before the amplitude and phase relationships can be developed, it is useful to derive a simple phase shifting algorithm for higher harmonic phase angles relative to the first harmonic phase angle. Suppose a given periodic wave containing all harmonics, and referenced to a particular datum, is expressed in the general form

$$\sum_{k=1}^{\infty} C_k \cos k\psi \tag{31}$$

and suppose the datum (or origin) is shifted by a phase angle δ_1, such that the general form becomes

$$\sum_{k=1}^{\infty} C_k \cos k \left(\psi + \delta_1\right) \tag{32}$$

In the original formulation of Eq. (31) this is equivalent to rewriting the argument of the cosine with some (as yet) undetermined phase shift for each harmonic in the form

$$\sum_{k=1}^{\infty} C_k \cos \left(k\psi + \delta_k\right) \tag{33}$$

BEST DOCUMENT AVAILABLE

Since the wave form is invariant, the arguments of the cosines in Eqs. (32) and (33) must be identical, leading to

$$k(\psi + \delta_1) = k\psi + \delta_k$$

or

$$\delta_k = k\delta_1 \tag{34}$$

Simply stated, this shows that if a multiharmonic wave is shifted by δ_1 in the first harmonic, then the phase shift of the kth harmonic is $k\delta$. The required amplitude and phase relationships for periodicity may now be derived.

The reference motion was measured on blade 6 in this experiment. This motion is adapted from Eq. (3) to read

$$\alpha^{(6)} = \bar{\alpha}^{(6)} e^{i\omega t} \tag{35}$$

Accordingly, the first harmonic pressure response (at some unspecified chordwise location) is rewritten from Eq. (2) as

$$C_{p_1}^{(6)} = \bar{C}_{p_1}^{(6)} e^{i\left(\omega t + \phi_{p_1}^{(6)}\right)} \tag{36}$$

and similarly, the kth harmonic response is

$$C_{p_k}^{(6)} = \bar{C}_{p_k}^{(6)} e^{i\left(k\omega t + \phi_{p_k}^{(6)}\right)} \tag{37}$$

BEST DOCUMENT AVAILABLE

where, in general, $\phi_{pk}^{(6)}$ is the phase lead of the kth harmonic response component of blade 6 relative to the motion of blade 6. Under ideal conditions, for an interblade phase angle, σ, between adjacent blades, and for the same amplitude of motion for all blades, the motion for the nth blade is given exactly by

$$\begin{aligned} \alpha^{(n)} &= \alpha^{(6)} e^{i(n-6)\sigma} \\ &= \bar{\alpha}^{(6)} e^{i[\omega t + (n-6)\sigma]} \end{aligned} \tag{38}$$

(Note that a positive value of σ implies that the motion of blade n leads the motion of blade n-1 by σ.) On this basis, the first and kth harmonic pressure response for blade n is related to the blade 6 response by

$$C_{p_1}^{(n)} = C_{p_1}^{(6)} e^{i(n-6)\sigma} \tag{39}$$

$$C_{p_k}^{(n)} = C_{p_k}^{(6)} e^{ik(n-6)\sigma} \tag{40}$$

where the kth harmonic phase shift in Eq. (40) is a direct consequence of Eq. (34). Now expand both sides of Eq. (40) separately. In analogy with Eq. (37), the left hand side of Eq. (40) will be referred to the motion of blade 6 by introducing a general kth harmonic phase angle relative to the time reference, $k\omega t$,

$$C_{p_k}^{(n)} = \bar{C}_{p_k}^{(n)} e^{i\left(k\omega t + \theta_k^{(n)}\right)} \tag{41}$$

By virtue of the instrumentation used in the experiment, $\theta_k^{(n)}$ is the actual kth harmonic response phase angle measured on blade n relative to the motion of blade 6. Similarly, the right hand side of Eq. (40) becomes

$$C_{p_k}^{(6)} e^{ik(n-6)\sigma} = \bar{C}_{p_k}^{(6)} e^{i\left(k\omega t + \phi_{p_k}^{(6)}\right)} e^{ik(n-6)\sigma} \tag{42}$$

BEST DOCUMENT AVAILABLE

With the assumption that the amplitudes of all blades are equal, the arguments of the exponentials in Eqs. (41) and (42) may be set equal. On cancelling $k\omega t$, the result for the generalized kth harmonic is

$$\theta_k^{(n)} = \phi_{p_k}^{(6)} + k(n-6)\sigma \tag{43}$$

or, on solving for $\phi_{pk}^{(6)}$,

$$\phi_{p_k}^{(6)} = \theta_k^{(n)} - k(n-6)\sigma \tag{44}$$

It was stated earlier that in the ideal case the blade-to-blade response phase angles would be identical. In Eq. (44), $\theta_k^{(n)}$ is the phase of the kth harmonic pressure response measured on blade n relative to the motion of blade 6. Under the ideal conditions just cited, if $\theta_k^{(n)}$ is adjusted by the quantity $k(n-6)\sigma$, it will yield the phase shift of the kth harmonic response of blade 6 relative to the motion of blade 6, $\phi_{pk}^{(6)}$, since ideally, this is invariant over the entire cascade. However, there is, in reality, some blade to blade variation, so the removal of $k(n-6)\sigma$ from the measured $\theta_k^{(n)}$ on the right side of Eq. (44) must be interpreted as yielding the kth harmonic of the response phase angle of blade n relative to its own motion $\phi_{pk}^{(n)}$, and hence Eq. (44) is rewritten as

$$\phi_{p_k}^{(n)} = \theta_k^{(n)} - k(n-6)\sigma \tag{45}$$

BEST DOCUMENT AVAILABLE

APPENDIX 2

POSSIBLE SOURCES OF GAPWISE PERIODICITY SCATTER

Four possible sources for the observed scatter in the gapwise periodicity data will be identified in this Appendix. In general, the results of this brief examination must remain inconclusive. The first three can be quantitatively assessed and do not appear to be major contributors to the problem while the fourth is impossible to evaluate quantitatively within the scope of this program.

Variation in Cam Eccentricity

The eccentric cams used to produce the sinusoidal pitching oscillations had small variations in their eccentricities as a result of machining tolerances. The analytical design of the cams showed that small errors in eccentricity would be manifested linearly as small errors in amplitude; i.e., if ε is the eccentricity, $\bar{\alpha}$ is the resultant amplitude, and subscripts O and A denote nominal and actual values, then

$$\bar{\alpha}_A/\bar{\alpha}_O = \varepsilon_A/\varepsilon_O \tag{46}$$

For simplicity, all pressures measured in the course of this experiment were normalized by the appropriate nominal amplitude (cf. Eq. (1)). If the resulting pressure coefficient magnitude is denoted by $\bar{C}p_O^{(n)}$ and the actual pressure coefficient magnitude (for the actual amplitude, $\bar{\alpha}_A$ experienced by the blade) by $\bar{C}p_A^{(n)}$, then from Eqs. (1) and (46),

$$\bar{C}p_A^{(n)} = \frac{\bar{C}p_O^{(n)}}{\bar{\alpha}_A/\bar{\alpha}_O} = \frac{\bar{C}p_O^{(n)}}{\varepsilon_A/\varepsilon_O} \tag{47}$$

A "worst case" condition was chosen to apply this correction. This was taken from the upper left panel of Fig. 14 for $\alpha = 2 \pm 2$ deg, $\sigma = -135$ deg, $k = 0.151$, and for 0.012U. The results are summarized in Table 7. All cam eccentricities are listed, together with their ratios to the design value, $\varepsilon_O = 0.103$. Values of the pressure coefficient amplitude plotted in Fig. 14 are listed as $\bar{C}p_O^{(n)}$, and have been "corrected" to actual values by Eq. (47).

BEST DOCUMENT AVAILABLE

It is seen that there is virtually no change in the scatter of pressure data, which is to be expected because the eccentricities are within 2 percent of their average value while the pressure data scatter is over approximately 13 percent of the average pressure. Furthermore, Fig. 14 shows that for 0.012U there is an inconsistent scatter pattern over the range of σ, a significantly different gapwise variation for 0.012L, and no scatter for 0.062U. It can be concluded, therefore, that variations in eccentricity play a small role in the observed scatter of gapwise data.

Variation in Local Dynamic Pressure

In like manner, the possibility that local variation in dynamic pressure might cause some gapwise scatter was investigated. Again, nominal and actual values are denoted by subscripts O and A, and, by the definition of dynamic pressure,

$$q = \frac{1}{2} \rho V^2 \tag{48}$$

a q-corrected version of Eq. (47) may be written as

$$\bar{C}p_A^{(n)} = \frac{\bar{C}p_O^{(n)}}{(V_A/V_O)^2} \tag{49}$$

A further adjustment to the values used in this correction is required because blade locations do not coincide with sidewall static measurement locations. Hence, the "actual" velocity, V_A, in Eq. (49) must be interpolated to represent the free stream value at the blade, and a linear interpolation between static wall locations was used.

All pertinent values are contained in Table 8. The measured velocities together with the height of the measurement station were used to compute the interpolated velocity, V_A, at the blade, and the ratio, V_A/V_O, was computed relative to the tunnel reference velocity V_O = 61 m/sec. This time the values of $\bar{C}p_o^{(n)}$ were taken directly from Ref. 8 for $\alpha = 2 \pm 2$ deg, $\sigma = 135$ deg, $k = 0.122$, and for 0.012U, but this gapwise distribution is substantially the same as that in Fig. 14 for $\sigma = 135$ deg and $k = 0.151$.

BEST DOCUMENT AVAILABLE

Once again there is virtually no change in the scatter of pressure data, $\bar{C}p_A^{(n)}$, as a result of this correction. Furthermore, if q-variations were significant in producing scatter, all blade locations would be expected to participate in the change because, as with cam eccentricity, q is a parameter that affects the entire blade. Clearly this is not the case here, and hence q-variation can also be dismissed as a major contributor to gapwise scatter.

Variation in Transducer Placement

It has been noted that the greatest scatter at $\alpha_{MCL} = 2$ deg occurs near the leading edge where the greatest local pressure gradient occurs. If a transducer orifice were misplaced from its nominal location, this steep gradient could magnify a discrepancy between the desired measured value and the actual measured value by the slope of the gradient, and small random machining errors in orifice placement could lead to larger scatter in the data. Hence, measurements of transducer orifice locations were made for all instrumented blades except blade 6 (which was unavailable at the time), and these values for 0.012U are listed in the second column of Table 9 as x_A. (The nominal value is $x_o = 0.012$.)

It was decided to use the gradient for a theoretical steady flat plate as a first approximation. This has the form

$$\bar{C}p_o^{(n)} = \sqrt{\frac{1-x_o}{x_o}} \tag{50}$$

for x_o and a comparable relationship for $\bar{C}p_A^{(n)}$ and x_A. This time it will be assumed that $\bar{C}p_A^{(n)}$ is the measured value at x_A and the degree to which a correction to $\bar{C}p_o^{(n)}$ reduces scatter will be evaluated. Hence, the relationship between these two quantities becomes

$$\bar{C}p_o^{(n)} = \bar{C}p_A^{(n)} \frac{\sqrt{(1-x_o)/x_o}}{\sqrt{(1-x_A)/x_A}} \tag{51}$$

Values from Table 7 will be used, and in accordance with the statement just made, the $\bar{C}p_o^{(n)}$ values in this table will be listed as $\bar{C}p_A^{(n)}$ in Table 9.

BEST DOCUMENT AVAILABLE

As before, the corrections do not account for the scatter, and in a few locations, make it worse. Hence, this too must be discarded as a possible source.

Variation in Local Blade Contour

From the observations of the data, and the analyses performed above, it would appear that if the scatter is blade-related it would necessarily be a local phenomenon since it appears to have a different behavior for different locations. Hence, one can speculate that local blade-to-blade variations in surface contour near the leading edge station could contribute to some of the observed scatter. However, this is extremely difficult to assess because of the inherent inaccuracies associated with measuring minute surface irregularities in a region of rapid changes (i.e., the leading edge) and the additional difficulty of interpreting these irregularities in terms of the periodic scatter they may produce. At best, this must remain an open question.

However, this may be carried a bit further. Examination of Fig. 14 and of the tabulated data in Ref. 10 for 0.012U shows that the scatter pattern at any given σ seems to remain the same as k is varied, and is similar for neighboring values of σ, but note that there are significant changes in this scatter pattern from $\sigma = -135$ deg to $\sigma = 0$ deg and further differences to $\sigma = 45$ deg. When this is further evaluated in the light of the patterns shown in Figs. 13, 15, and 16, it is evident that aerodynamic interactions may also be taking place that are dependent on both amplitude, incidence angle, and interblade phase angle. Thus, the only conclusion to be reached, with the present state of knowledge, is that the study of potential sources for the observed data scatter must remain inconclusive.

BEST DOCUMENT AVAILABLE

APPENDIX 3

ACOUSTICAL RESONANCE

The object of the material presented in this Appendix is to show that the acoustical resonance phenomenon is a plausible explanation for the gapwise phase gradient when $\sigma = 0$ deg. However, it is important to note that no proof that the phenomenon exists is claimed or implied.

The concept of acoustical resonance in a cascade has been discussed by many authors, mostly in the context of a singular behavior of the cascade solution in a compressible flow. A more physical approach was recently described in Ref. 17 in which the general formula

$$2\pi\nu \pm \sigma = \frac{2kM\,\tau/C}{\sqrt{1-M^2\sin^2\beta_1^*} \mp M\cos\beta_1^*} \qquad \nu=0,1,2,\ldots \tag{52}$$

is given. Here k is reduced frequency, M is Mach number, τ/c is gap/chord ratio, and β_1^* is stagger angle. This solution represents two possible modes: a forward wave with $\nu = 0$ and use of the upper sign, and a backward wave with $\nu = 1$ and the lower sign. Both of these modes are valid, and both are computed. The parameters used here are:

$$M \leq 0.18$$
$$\tau/c = 0.75$$
$$\beta_1^* = 30 \text{ deg}$$

A straightforward computation for the three test values of k leads to the results given below.

	forward wave $\nu = 0$		backward wave $\nu = 1$	
k	σ (rad)	σ (deg)	σ (rad)	σ (deg)
0.072	0.023	1.3	6.266	-1.0
0.122	0.039	2.2	6.255	-1.6
0.151	0.049	2.8	6.248	-2.0

With these values nested so closely about $\sigma = 0$, it is obvious that the opportunity for resonance exists.

BEST DOCUMENT AVAILABLE

APPENDIX 4

HIGHER HARMONIC BEHAVIOR AND WIND TUNNEL DISTURBANCES

An examination of the tabulations of data in Ref. 8 shows that significant higher harmonic amplitudes exist in the single surface data that disappear on taking the pressure differential across blade 6. An example of this phenomenon is shown in Fig. 35 for 2 ± 0.5 deg at $\sigma = -45$ deg and $k = 0.072$. The three panels across the top are pressure magnitude for the upper and lower surfaces, and the difference across blade 6, and the three panels across the bottom are the response phase angles for these pressures. Within each of the single surface panels and within the pressure difference magnitude panel, the circle, triangle, and square symbols denote the first, second, and third harmonics, respectively. The most striking features of these distributions are: 1) the constant chordwise level of higher harmonic response amplitude for the single surface data, 2) the same behavior for the higher harmonic phase angle distributions, and 3) the equality of the upper surface distributions to the lower surface distributions. By virtue of this equality at each chordwise station, the higher harmonic content of the single surfaces is cancelled on taking the pressure difference. This is evident in the upper right panel where, over most of the chord, the second and third harmonic pressure difference is nearly an order of magnitude smaller than either of the single surface values. No second and third harmonic pressure difference phase angles are plotted in the lower right panel because these data are now scattered and exhibit no trend.

A further sample of this behavior is shown in Figs. 36 and 37. These are spectral histograms for amplitude and phase angle, respectively, of the $\chi = 0.261$ station, chosen to remove it from the immediate effect of the leading edge. The three columns in each figure are for the upper, lower, and differential values, and several cases are presented in the vertical panels. Within each panel the harmonic value is plotted as a vertical line at each harmonic number. The appended numbers above each first harmonic amplitude represent the value for out of scale responses. It is seen that the upper and lower surface spectra, both amplitude and phase angle, are nearly identical for second and higher harmonics, and that the vector subtraction of these equal and in-phase components leads to a significantly smaller differential result.

Some speculation on the origin of this phenomenon is in order. An examination of the data in Ref. 8 reveals the following: 1) the phenomenon is most prominent for 2 ± 0.5 deg and is still in evidence for 6 ± 0.5 deg, 2) the higher harmonic amplitudes have virtually disappeared when $\bar{\alpha} = 2$ deg, and 3) the harmonic distribution shifts as k changes. The first two observations imply that the origin of the higher harmonic behavior is independent of motion amplitude, and may even be constant, since normalization with respect to motion amplitude causes its level to vary inversely with amplitude. The third observation is signi[illegible]t in that it

BEST DOCUMENT AVAILABLE

implies no connection between the frequency of the motion and the frequency of the phenomenon (because for each run and point the Fourier analysis was based on motion frequency). Thus, it may be surmised that the disturbance is a longitudinal wave in the test section, possibly associated with the tunnel dimensions and the flow or source characteristics. This is supported by its disappearance on taking differences.

This phenomenon was not seen before in Refs. 1-4 because 1) previous motion amplitudes were always $\bar{\alpha}$ = 2 deg and at this level the pressure wave is barely discernable, and 2) in this current test the improved data system (ATLAS) was capable of making more precise measurements. Whatever the phenomenon, it is not believed to contribute strongly to first harmonic periodicity scatter (Figs. 13-16) because most of the observed amplitude scatter is at $\bar{\alpha}$ = 2 deg (Fig. 14) where this effect is least evident. There is a possible contribution to phase angle scatter but there is no way to prove this without more extensive tests.

BEST DOCUMENT AVAILABLE

REFERENCES

1. Carta, F. O. and A. O. St. Hilaire: An Experimental Study on the Aerodynamic Response of a Subsonic Cascade Oscillating Near Stall. Project SQUID Technical Report UTRC-2-PU, July 1976.

2. Arnoldi, R. A., F. O. Carta, R. H. Ni, W. N. Dalton, and A. O. St. Hilaire: Analytical and Experimental Study of Subsonic Stalled Flutter. AFOSR-TR-77-0854, July 1977.

3. Carta, F. O. and A. O. St. Hilaire: Experimentally Determined Stability Parameters of a Subsonic Cascade Oscillating Near Stall. Trans. ASME, Jour. of Engineering for Power, January 1978, Vol. 100, pp. 111-120.

4. Carta, F. O. and A. O. St. Hilaire: Effect of Interblade Phase Angle and Incidence Angle on Cascade Pitching Stability. Transactions ASME, Jour. of Engineering for Power, Vol. 102, No. 2, April 1980, pp. 391-396.

5. Johnson, I. A. and R. O. Bullock, ed.: Aerodynamic Design of Axial Flow Compressors. NASA SP-36, 1965.

6. Davis, E. L., Jr.: The Measurement of Unsteady Pressures in Wind Tunnels. AGARD Report 169, March 1958.

7. Carta, F. O. and R. L. O'Brien: Unsteady Aerodynamic Measurement Techniques for Turbomachinery Research. ASME Symposium on Measurement Methods in Rotating Components of Turbomachinery, New Orleans, La., March 1980, ed. B. Lakshminarayana and P. Runstadler, Jr., pp. 177-185.

8. Carta, F. O.: An Experimental Investigation of Gapwise Periodicity and Unsteady Aerodynamic Response in an Oscillating Cascade. Vol. II, Data Report NASA CR 165457, December 1981.

9. Stremler, F. G.: Introduction to Communication Systems. Addison-Wesley Publishing Co., Reading, Mass., 1977, p. 112 et. seq.

10. Smith, S. N.: Discrete Frequency Sound Generation in Axial Flow Turbomachines. Great Britain A.R.C. R. & M. No. 3709, 1971.

11. Verdon, J. M. and J. R. Caspar: Subsonic Flow Past an Oscillating Cascade with Finite Mean Flow Deflection. AIAA Journal, Vol. 18, No. 5, May 1980, pp. 540-548.

BEST DOCUMENT AVAILABLE

REFERENCES (Cont'd)

12. St. Hilaire, A. O.: An Analysis of the Inlet Plane Aerodynamics of an Oscillating Subsonic Cascade: An Evaluation of Experimental Data. United Technologies Research Center Report R81-914838, Prepared for the U.S. Navy, Office of Naval Research, under Contract N00014-79-C-0772, February 1981. (AD-A096077)

13. Rothrock, M. D., R. L. Jay, and R. E. Riffel: Time-Variant Aerodynamics of High-Turning Blade Elements. Presented at the ASME Gas Turbine Conference, Houston, Texas, March 1981, Paper No. 81-GT-123.

14. Jay, R. L., M. D. Rothrock, R. E. Riffel, and G. T. Sinnet: Time-Variant Aerodynamics for Torsional Motion of Large-Turning Airfoils. Detroit Diesel Allison Report EDR 10192, Prepared for the Department of the Navy, Naval Air Systems Command, under Contract N00019-79-C-0087, January 1980.

15. Stroud, A. H. and D. Secrest: Gaussian Quadrature Formulas. Prentice-Hall, Inc., Englewood Cliffs, N. J., 1966.

16. Hornbeck, R. W.: Numerical Methods. Quantum Publishers, Inc., New York, 1975.

17. Carta, F. O.: Aeroelasticity and Unsteady Aerodynamics. Chapter 22 in the Aerothermodynamics of Aircraft Gas Turbine Engines, G. C. Oates, ed., U.S. Air Force Report AFAPL TR 78-52, July 1978.

BEST DOCUMENT AVAILABLE

TABLE 1

DIMENSIONLESS AIRFOIL COORDINATES IN FRACTION OF CHORD

c = 15.24 cm (6 in.)

SUCTION SURFACE		PRESSURE SURFACE	
X	+y/c	X	-y/c
0.0008	0.0020	0.0012	0.0019
0.0046	0.0053	0.0054	0.0042
0.0070	0.0064	0.0080	0.0050
0.0120	0.0083	0.0130	0.0061
0.0244	0.0116	0.0256	0.0077
0.0494	0.0164	0.0507	0.0098
0.0743	0.0204	0.0757	0.0115
0.0993	0.0237	0.1007	0.0129
0.1494	0.0290	0.1506	0.0150
0.1994	0.0331	0.2006	0.0165
0.2495	0.0364	0.2505	0.0177
0.2996	0.0387	0.3004	0.0185
0.3998	0.0411	0.4002	0.0188
0.5000	0.0406	0.5000	0.0176
0.6002	0.0370	0.5998	0.0146
0.7003	0.0306	0.6997	0.0104
0.8003	0.0223	0.7997	0.0069
0.8503	0.0176	0.8497	0.0053
0.9003	0.0127	0.8997	0.0040
0.9502	0.0078	0.9497	0.0032
0.9975	0.0030	0.9973	0.0025

	RADIUS CENTER COORDINATES
L. E. RADIUS/c = 0.0024	X = 0.0024, y/c = 0.0002
T. E. RADIUS/c = 0.0028	X = 0.9972, y/c = 0.0003

BEST DOCUMENT AVAILABLE

TABLE 2

TRANSDUCER ORIFICE LOCATIONS
(FRACTION OF CHORD)

a) Blade Transducers, Fractions of Chord

Blade Number	Values of X	
	Suction Surface	Pressure Surface
6	0.0120 0.0622 0.1478 0.2612 0.3924 0.5297 0.6608 0.7742 0.8598 0.9100	0.0120 0.0622 0.1478 0.2612 0.3924 0.5297 0.6608 0.7742 0.8598 0.9100
3,5,7,9	0.0120 0.0622	0.0120
4	0.0050 0.0120 0.0350 0.0622	

b) Sidewall Transducers, Gap Fraction From Blade 6 Suction Surface

Wall Station Number	Gap Fraction η
1	-0.125
2	0.0
3	0.062
4	0.125
5	0.25
6	0.50
7	0.75
8	0.875
9	0.938
10	1.125

BEST DOCUMENT AVAILABLE

TABLE 3

BLADE DATA CHANNELS

ATLAS CHANNEL NUMBER	MODE 1		MODE 2	
	BLADE OR WALL LOCATION	χ or η	BLADE OR WALL LOCATION	χ or η
1*	a	-	a	-
2*	6S1	0.0120	6S1	0.0120
3*	6S2	0.0622	6S2	0.0622
4	6S3	0.1478	3S1	0.0120
5	6S4	0.2612	3S2	0.0622
6	6S5	0.3924	3P1	0.0120
7	6S6	0.5297	4S1	0.0050
8	6S7	0.6608	4S2	0.0120
9	6S8	0.7742	4S3	0.0350
10	6S9	0.8598	4S4	0.0622
11	6S10	0.9100	5S1	0.0120
12*	6P1	0.0120	6P1	0.0120
13*	6P2	0.0622	5S2	0.0622
14	6P3	0.1478	5P1	0.0120
15	6P4	0.2612	7S1	0.0120
16	6P5	0.3924	7S2	0.0622
17	6P6	0.5297	7P1	0.0120
18	6P7	0.6608	9S1	0.0120
19	6P8	0.7742	9S2	0.0622
20	6P9	0.8598	9P1	0.0120
21	6P10	0.9100	W3	0.062
22	W1	-0.125	W5	0.250
23	W2	0.000	W7	0.750
24*	W4	0.125	W4	0.125
25	W6	0.500	W8	0.875
26	W10	1.125	W9	0.938

* DENOTES REDUNDANT CHANNEL

NOTES:

- Blade location notation ---

  3S2 → blade 3, suction surface, second transducer aft of leading edge (P denotes pressure surface)

- Transducer location values ---

  χ is blade chord fraction
  η is sidewall gap fraction

BEST DOCUMENT AVAILABLE

TABLE 4

UNSTEADY DATA CYCLE PARAMETERS

(1000 samples/sec acquisition to 1024 samples storage)

Nominal Frequency f(Hz)	Number of Cycles for Analysis	Maximum Harmonics from Sampling Theory
9.2	9.4	54
15.5	15.9	32
19.2	19.7	26

BEST DOCUMENT AVAILABLE

TABLE 5

VALUES OF AERODYNAMIC DAMPING PARAMETER

Incidence Angle	Pitching Amplitude	Interblade Phase Angle	Aerodynamic Damping Parameter, Ξ, for f = 9.2 Hz	15.5 Hz	19.2 Hz
α_{MCL}	$\bar{\alpha}$	σ	k = 0.072	0.122	0.151
2	0.5	-135	0.5169	0.5472	0.5689
		- 90	0.7189	0.7506	0.8247
		- 45	0.8922	0.8632	0.8215
		0	0.3039	0.2175	0.2136
		45	-0.5578	-0.5500	-0.4745
		90	-0.5260	-0.3385	-0.3703
		135	-0.3158	-0.1849	-0.2038
		180	0.1163	0.1846	0.2351
	2	-135	0.5194	0.5218	0.5564
		- 90	0.7784	0.8178	0.8442
		- 45	0.8728	0.8455	0.8382
		0	0.2055	0.2266	0.1883
		45	-0.7438	-0.6235	-0.5577
		90	-0.5359	-0.4735	-0.4610
		135	-0.3544	-0.2822	-0.2678
		180	0.0590	0.1252	0.1460
6	0.5	-135	0.2772	0.3423	0.3841
		- 90	0.5688	0.6057	0.6223
		- 45	0.5770	0.5799	0.5673
		0	0.1414	0.1036	0.0812
		45	-0.4287	-0.3421	-0.3083
		90	-0.4355	-0.4348	-0.3796
		135	-0.2806	-0.2171	-0.2440
		180	0.0787	0.0460	0.0639
	2	-135	0.2888	0.3603	0.3803
		- 90	0.6251	0.6561	0.6874
		- 45	0.7034	0.7434	0.7339
		0	0.1708	0.1031	0.0935
		45	-0.4757	-0.3861	-0.3529
		90	-0.4313	-0.3991	-0.3793
		135	-0.2141	-0.2132	-0.2046
		180	0.0588	0.0828	0.1023

BEST DOCUMENT AVAILABLE

TABLE 6

GAUSSIAN QUADRATURE VALUES

Station Number	Gaussian Coordinate	Weighting Coefficient	Physical Coordinate
j	ξ_j	W_j	$x_j = z\,\xi_j$
1	0.013047	0.033336	0.01203
2	0.067469	0.074726	0.06221
3	0.160295	0.109543	0.14780
4	0.283303	0.134633	0.26121
5	0.425563	0.147762	0.39238
6	0.574437	0.147762	0.52965
7	0.716698	0.134633	0.66082
8	0.839705	0.109543	0.77423
9	0.932532	0.074726	0.85982
10	0.986954	0.033336	0.91000

($z = 0.92203$)

BEST DOCUMENT AVAILABLE

TABLE 7

ECCENTRICITY CORRECTION TO PRESSURES

Blade and Cam No.	ϵ_A (inches)	ϵ_A/ϵ_o	$-\bar{C}_{p_o}^{(n)}$	$-\bar{C}_{p_A}^{(n)}$
1	0.1055	1.0243		
2	0.1037	1.0068		
3	0.1051	1.0204	25.412	24.90
4	0.1055	1.0243	24.949	24.36
5	0.1052	1.0214	19.745	19.33
6	0.1002	0.9728	25.401	26.11
7	0.1067	1.0359	22.041	21.28
8	0.1044	1.0136		
9	0.1040	1.0097	19.895	19.70
10	0.1056	1.0252		
11	0.1040	1.0097		

NOTES:

- $\epsilon_o = 0.103$ is the design value
- Values of $\bar{C}_{p_o}^{(n)}$ taken from following conditions

  $\alpha = 2 \pm 2$ deg
  $\sigma = -135$ deg
  $k = 0.1516$
  File 38, Run 8, Point 7
  $X = 0.012$ suction

BEST DOCUMENT AVAILABLE

BEST DOCUMENT AVAILABLE

TABLE 8

LOCAL DYNAMIC PRESSURE CORRECTION TO PRESSURES

Static Tap Location h/h_{TUN}	Measured Velocity V, m/sec	Blade No.	Blade Location h/h_{TUN}	Interpolated Vel. at Blade V_A, m/sec	V_A/V_o	$-\bar{C}p_o^{(n)}$	$-\bar{C}p_A^{(n)}$
0.898	59.6						
0.815	62.0						
-	-	3	0.750	62.2	1.020	24.405	23.43
0.731	62.3						
-	-	4	0.667	61.2	1.004	24.568	24.39
0.648	60.9						
-	-	5	0.583	61.4	1.006	18.860	18.62
0.565	61.5						
0.509	61.0(ref)						
-	-	6	0.500	60.9	0.999	25.173	25.21
0.454	60.7						
-	-	7	0.417	60.6	0.993	20.981	21.27
0.370	60.4						
0.287	59.9						
-	-	9	0.250	59.9	0.982	19.589	20.33
0.204	59.8						
0.120	55.5						

NOTES:

- V_o = 61.0 m/sec is the reference value
- Values of $\bar{C}p_o^{(n)}$ taken from following conditions (cf. Ref. 10)
  - α = 2 ± 2 deg
  - σ = 135 deg
  - k = 0.1223
  - File 28, Run 7, Point 4
  - χ = 0.012 suction

TABLE 9

TRANSDUCER PLACEMENT CORRECTION TO PRESSURES

Blade Number n	Measured First Orifice Location x_A	$\bar{C}p_A^{(n)}$	Correction Multiplier Eq. (2-6)	$\bar{C}p_o^{(n)}$
3	0.0128	25.412	1.033	26:26
4	0.0125	24.949	1.021	25.47
5	0.0112	19.745	0.966	19.07
6	-	-	-	-
7	0.0123	22.041	1.013	22.32
9	0.0130	19.895	1.041	20.72

NOTES:

- $x_o = 0.012$ is the reference value
- Values of $\bar{C}p_A^{(n)}$ taken from following conditions
  - $\alpha = 2 \pm 2$ deg
  - $\sigma = -135$ deg
  - $k = 0.1516$
  - File 38, Run 8, Point 7
  - $x = 0.012$ suction

BEST DOCUMENT AVAILABLE

BEST DOCUMENT AVAILABLE

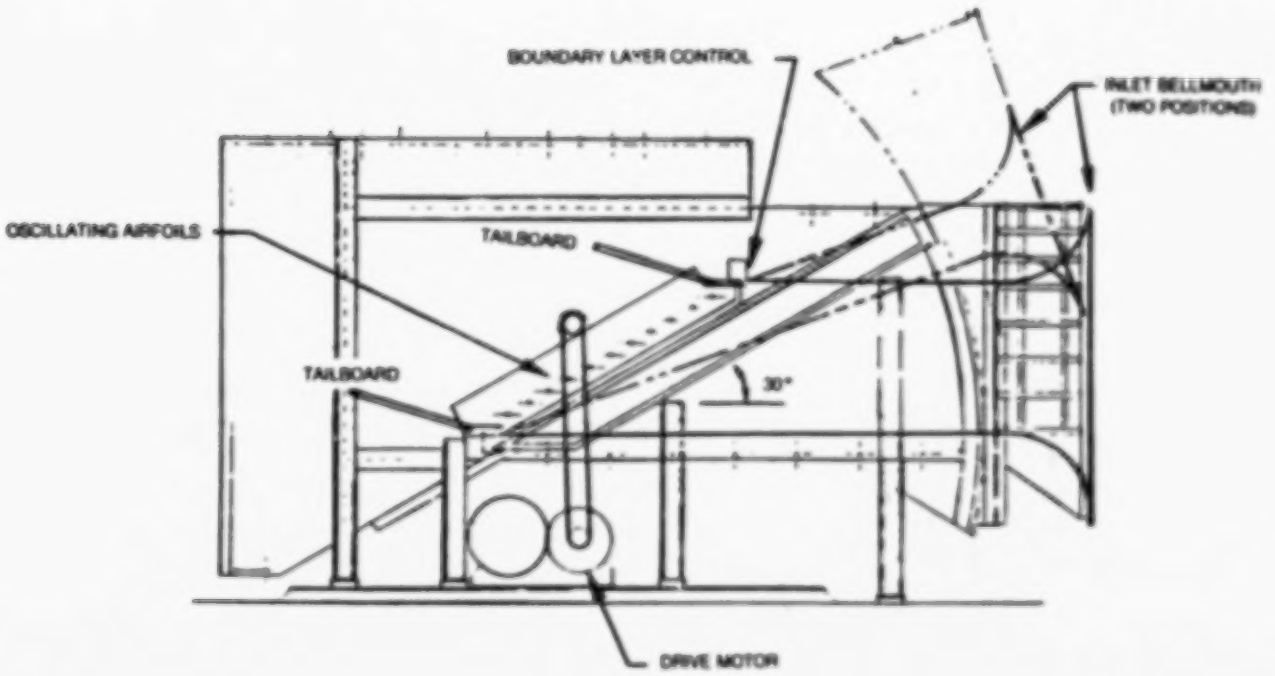

Figure 1 Schematic of Subsonic Oscillating Cascade Wind Tunnel

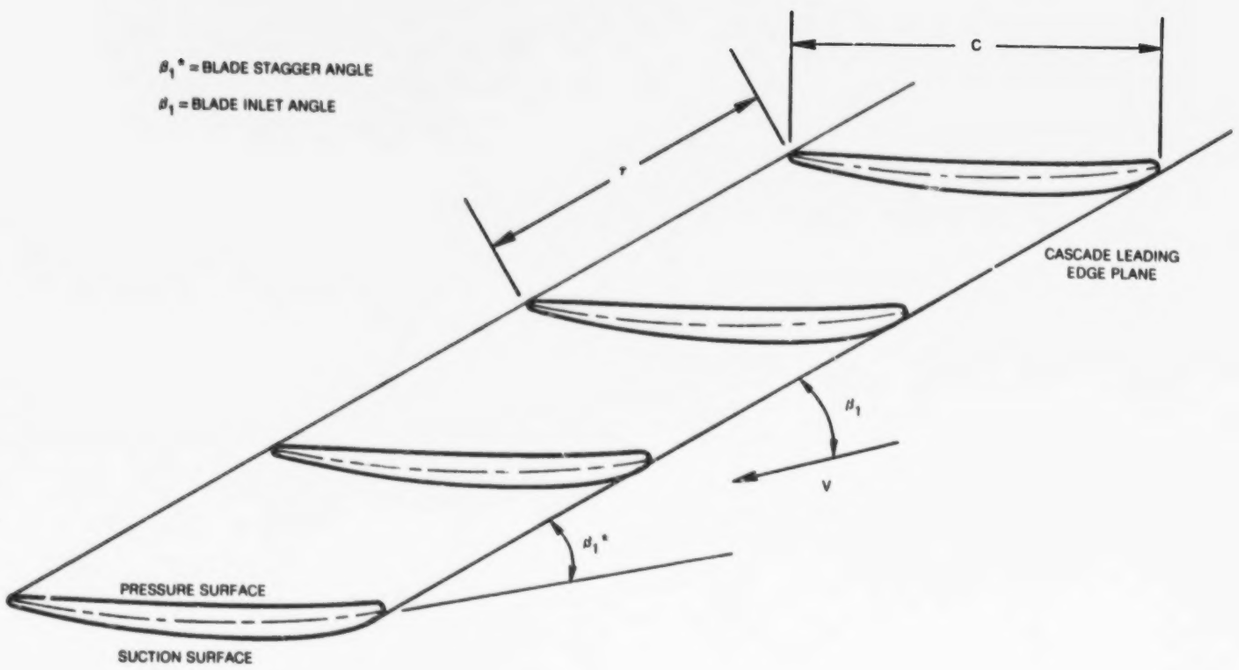

79-03-47-5

Figure 2 Cascade Geometry

BEST DOCUMENT AVAILABLE

BEST DOCUMENT AVAILABLE

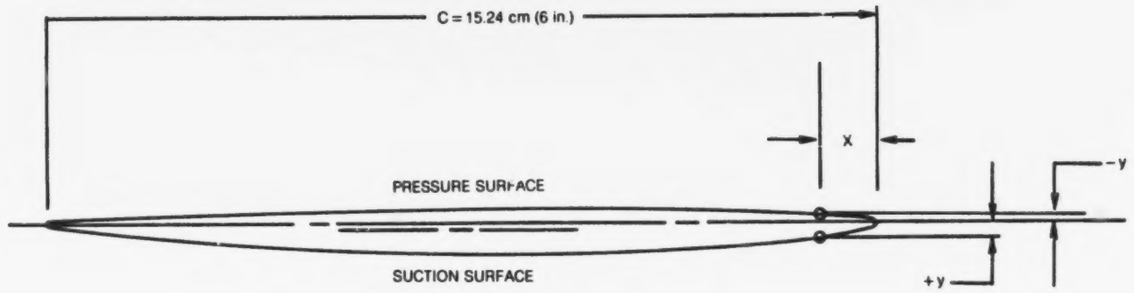

Figure 3 Cascade Blade Profile

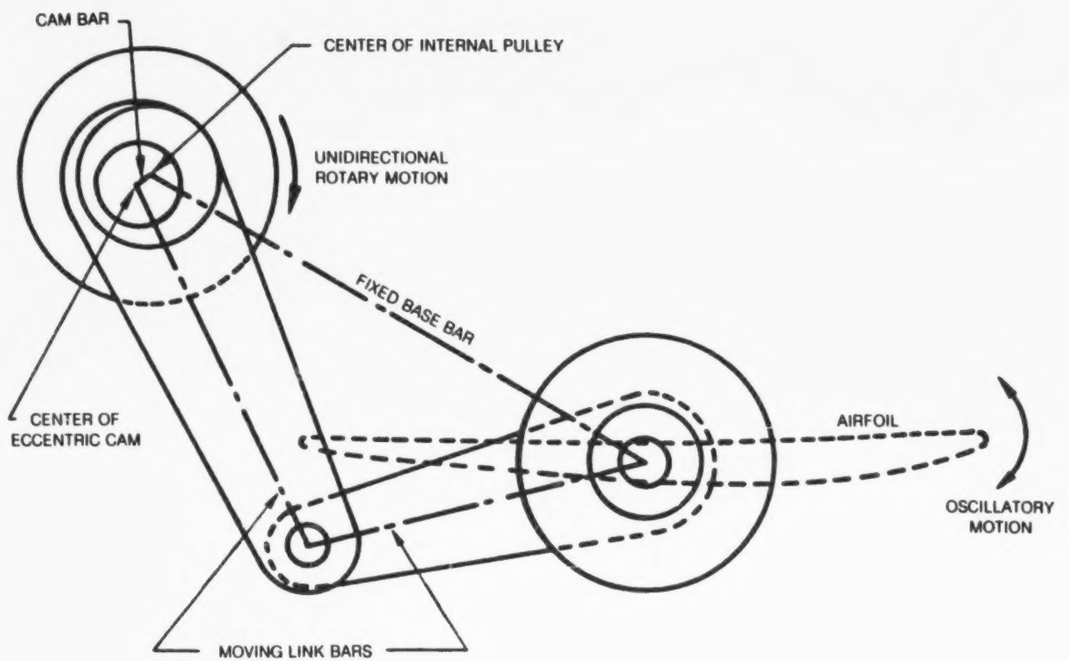

Figure 4 Four-Bar Linkage to Produce Sinusoidal Motion

79-03-114-4

BEST DOCUMENT AVAILABLE

BEST_DOCUMENT_AVAILABLE

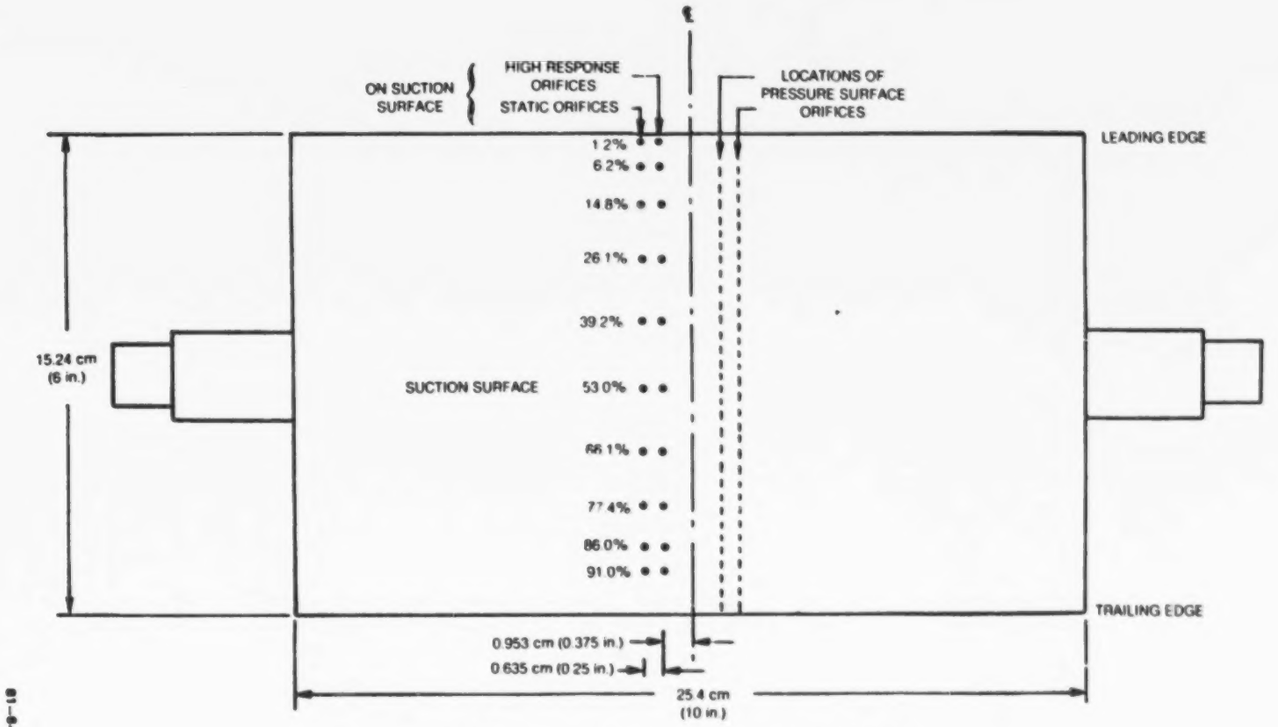

Figure 5 Schematic Plan View of Instrumented Airfoil

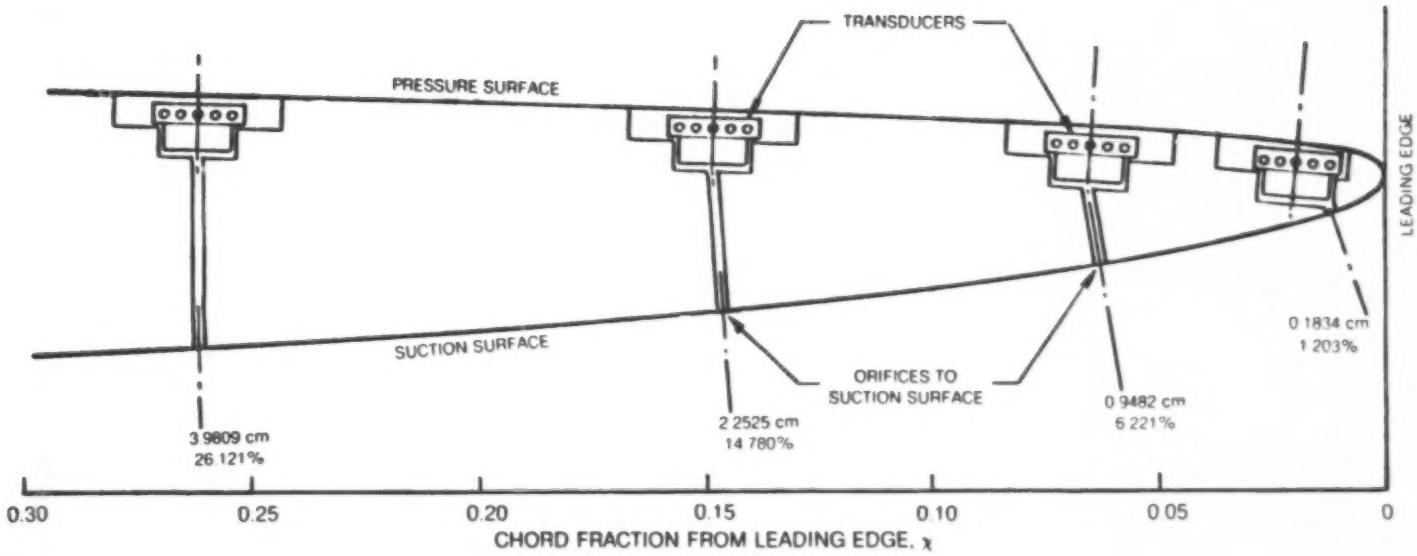

Figure 6 Section View Showing Suction Surface Instrumentation

BEST DOCUMENT AVAILABLE

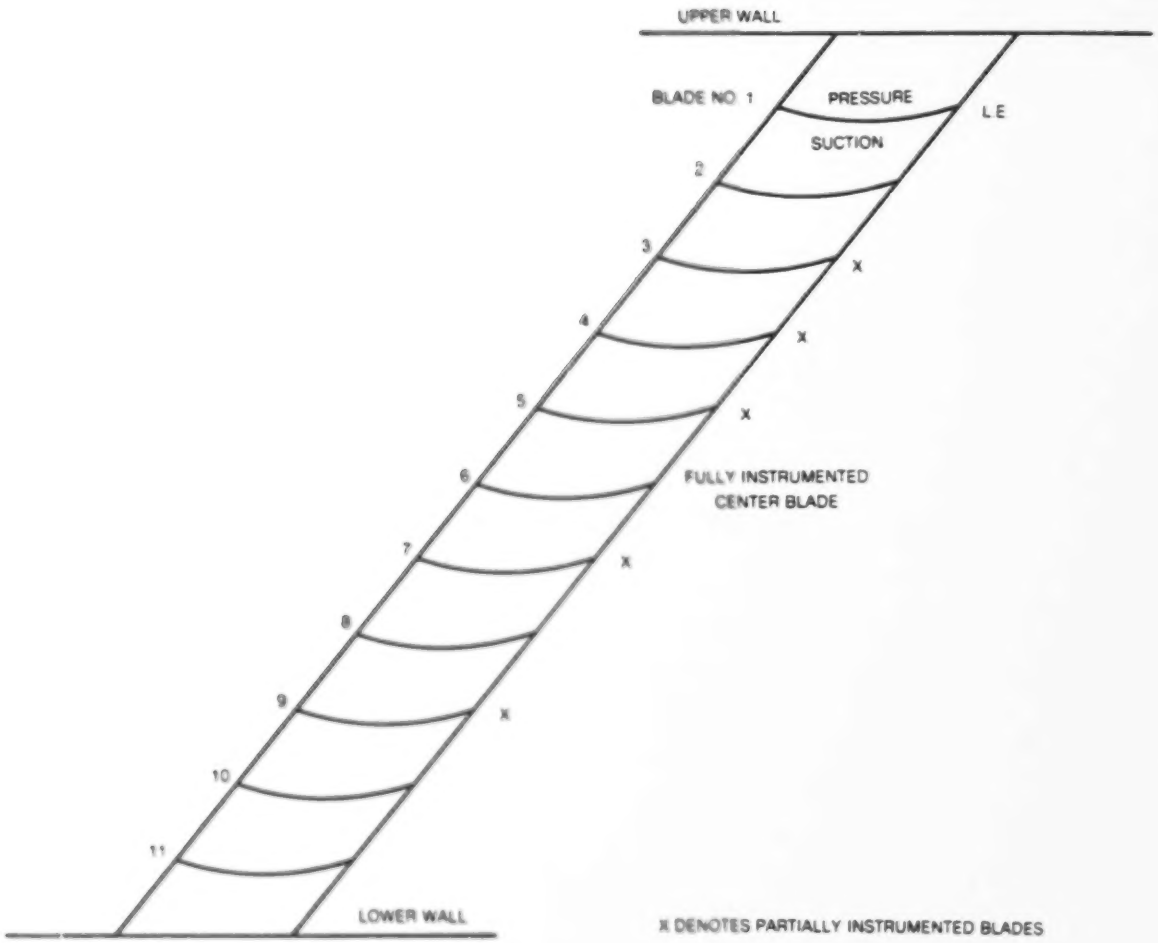

Figure 7 Schematic of Cascade Showing Instrumented Blades

81-6-84-3

BEST DOCUMENT AVAILABLE

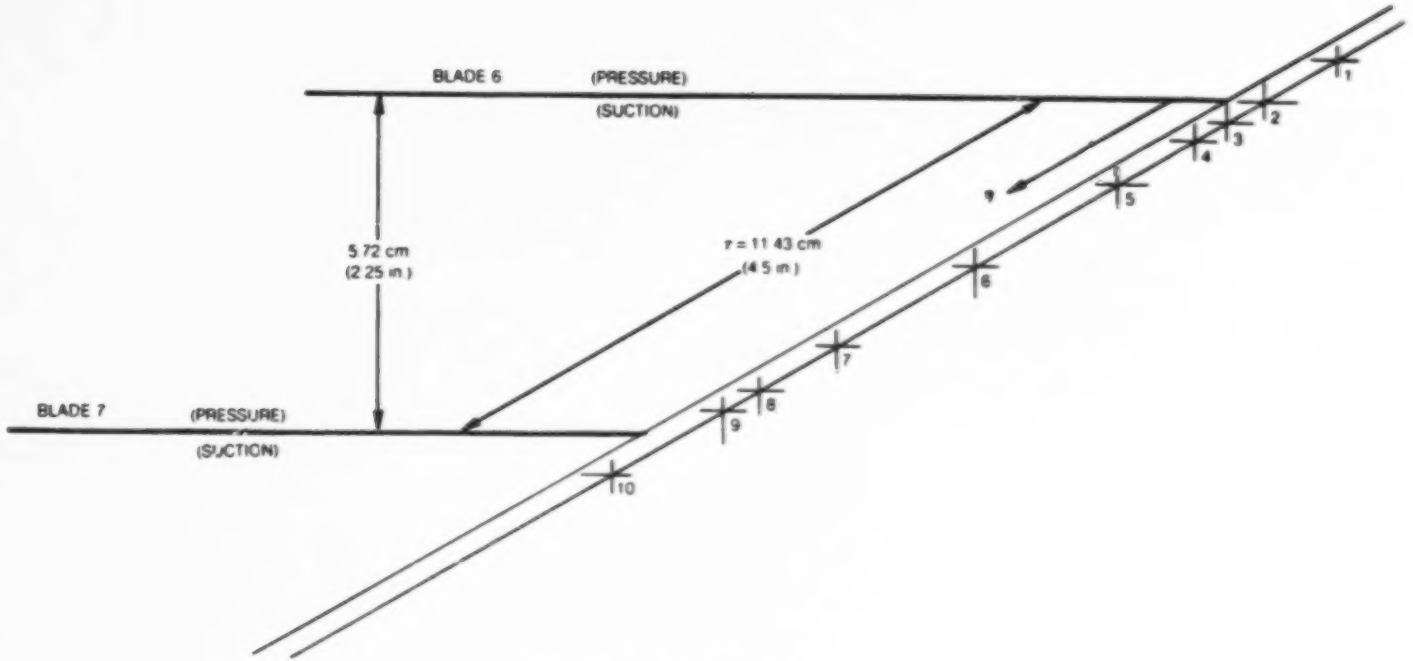

Figure 8 Sidewall Transducer Array

BEST DOCUMENT AVAILABLE

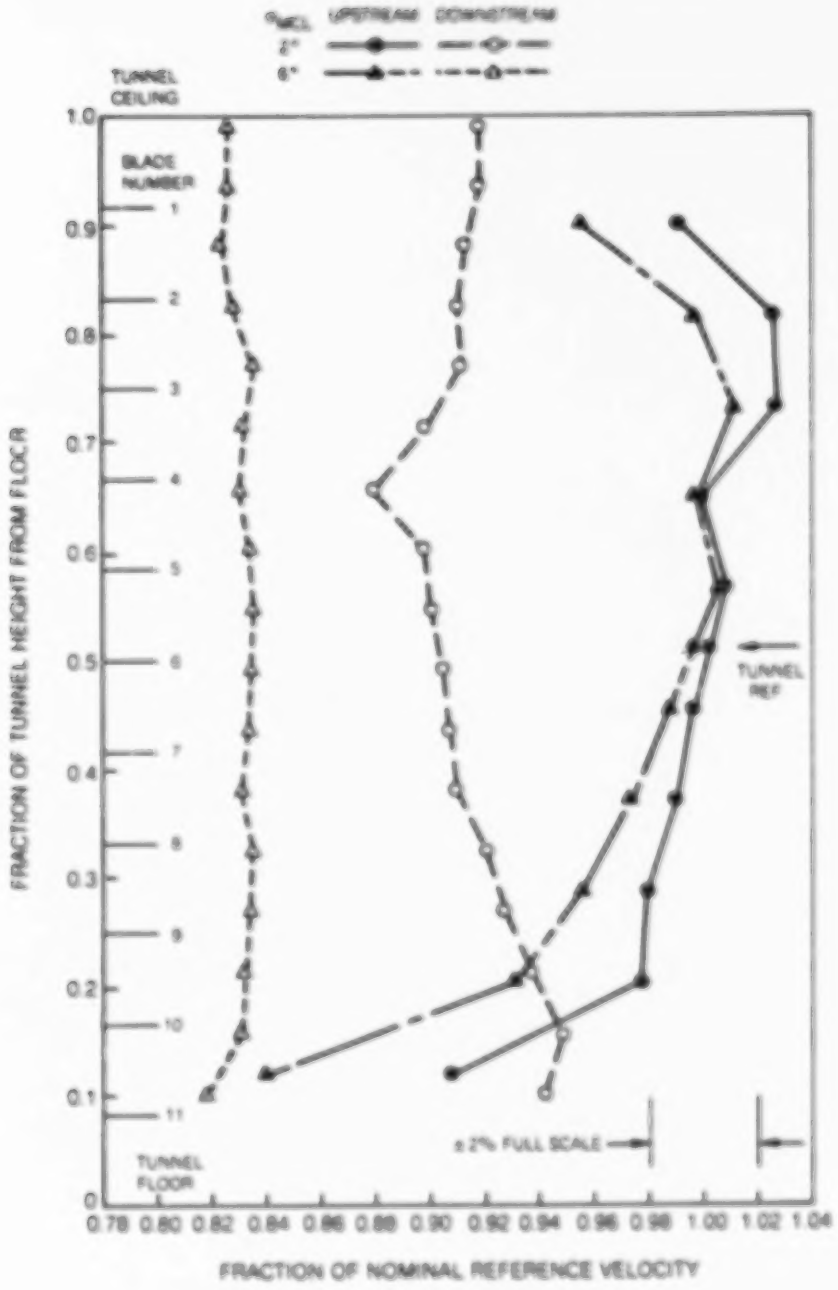

Figure 9 Steady-State Velocity Profiles

BEST DOCUMENT AVAILABLE

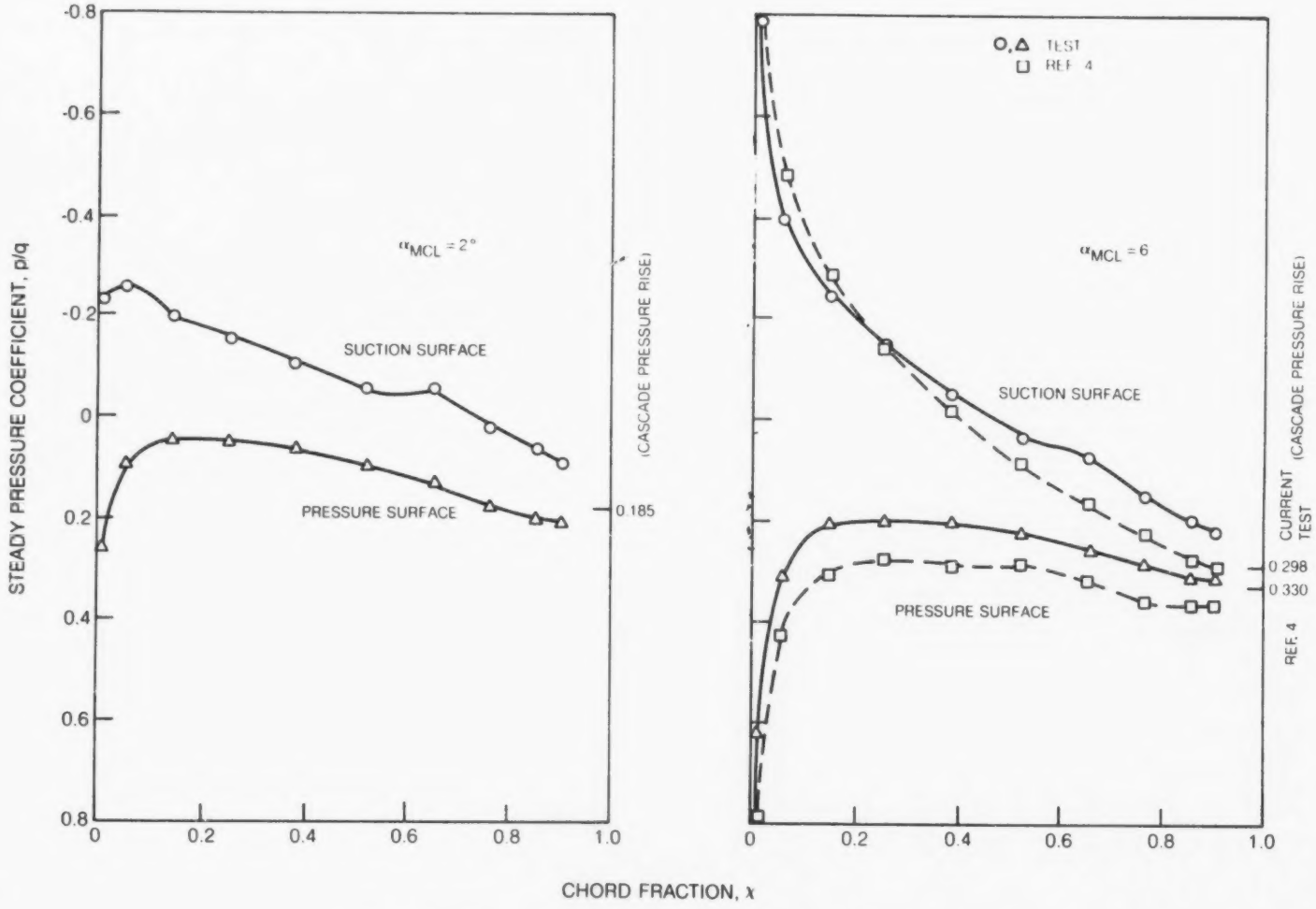

Figure 10 Steady-State Chordwise Pressure Distributions

BEST DOCUMENT AVAILABLE

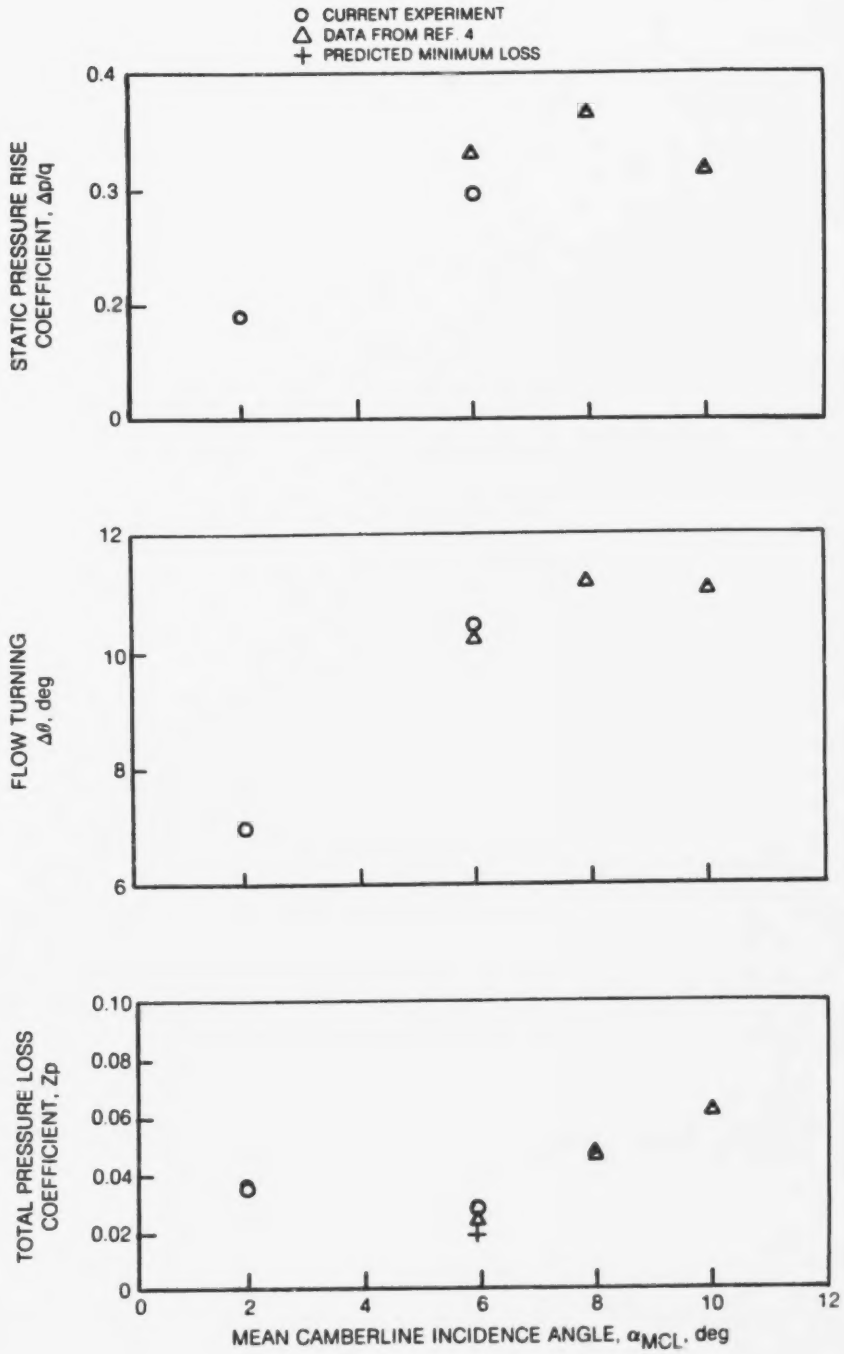

Figure 11 Steady-State Performance Parameters

81-6-84-6

BEST DOCUMENT AVAILABLE

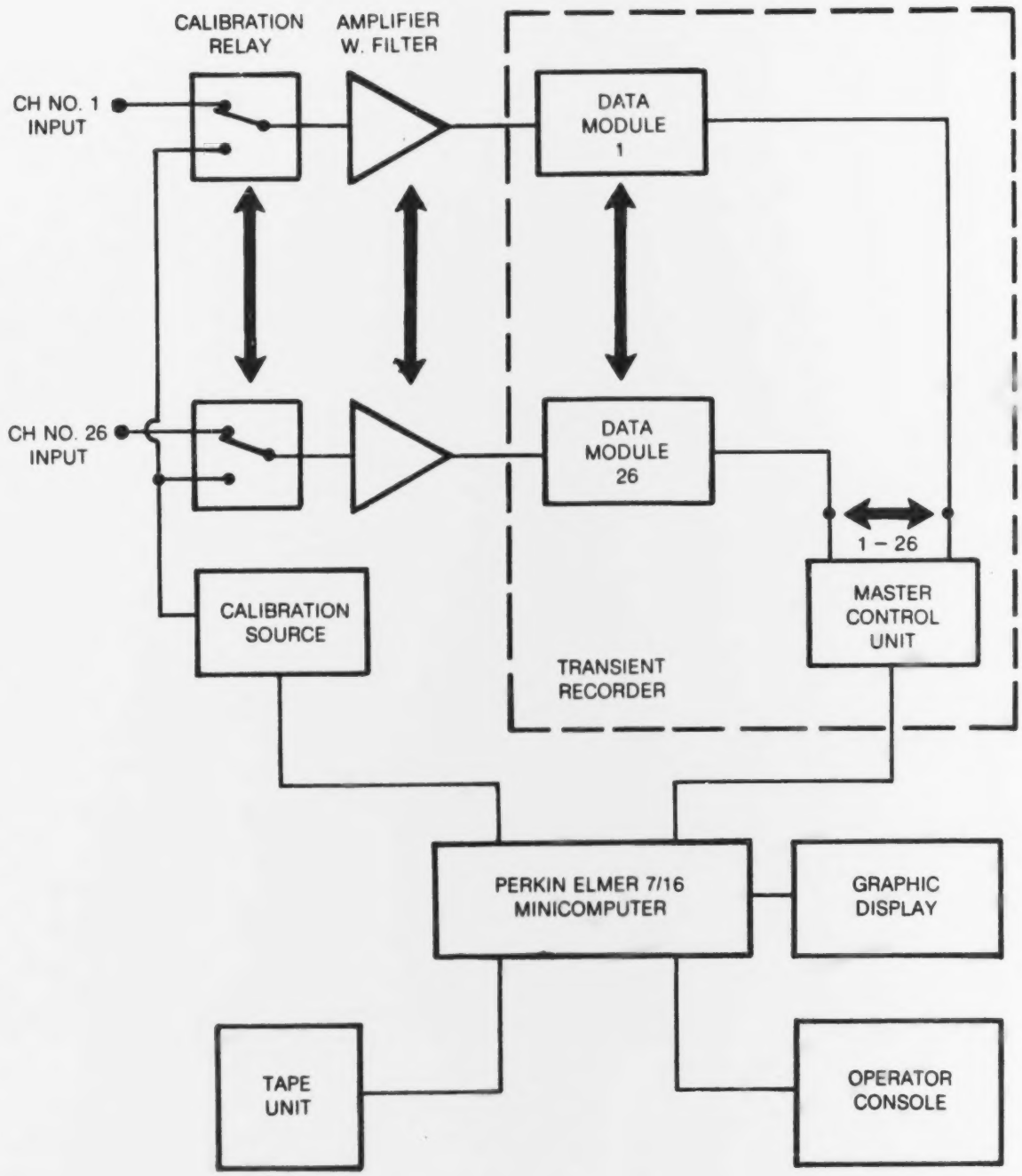

Figure 12 ATLAS Block Diagram

81-2-140-5

BEST DOCUMENT AVAILABLE

BEST DOCUMENT AVAILABLE

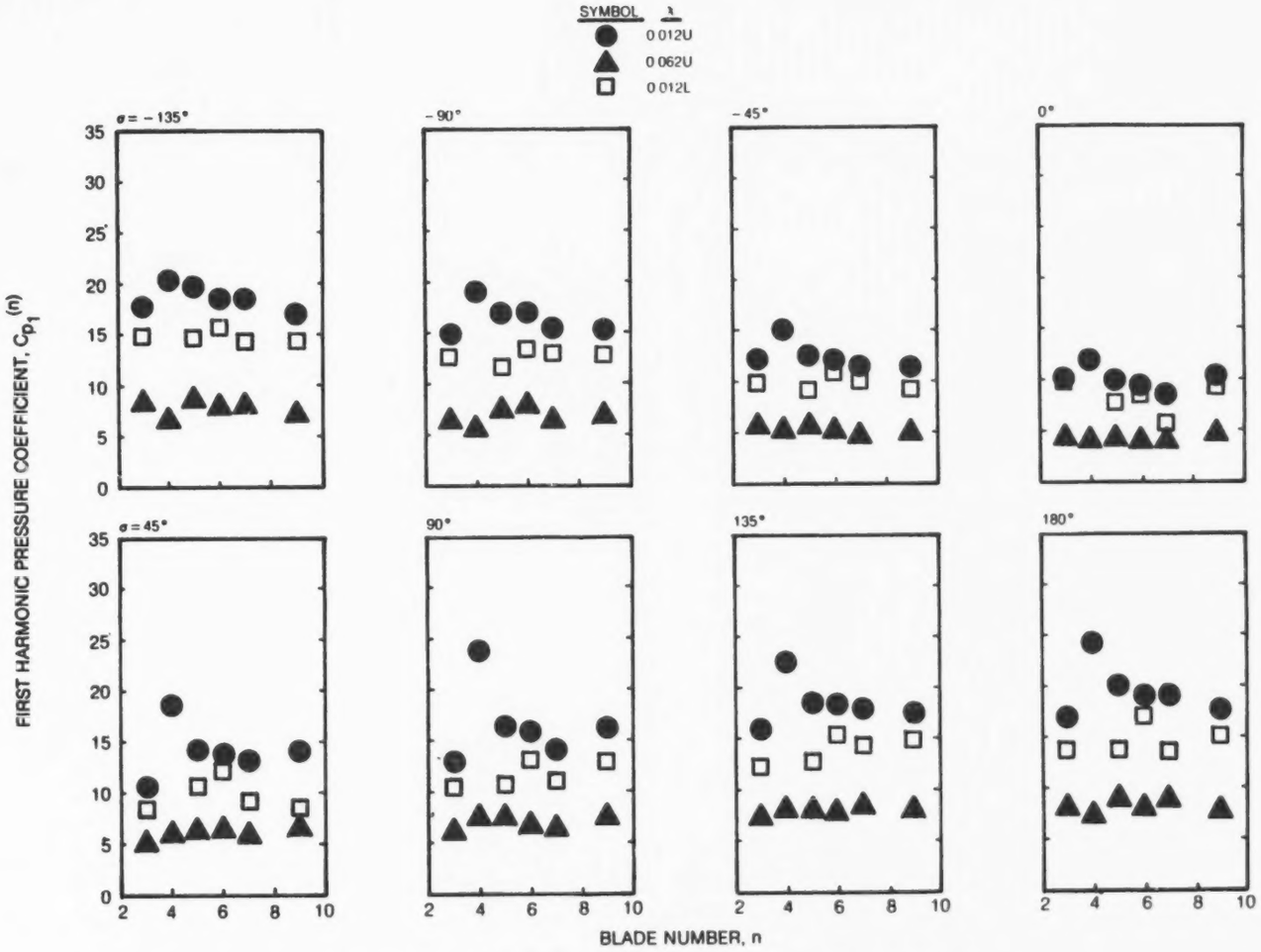

Figure 13 Gapwise Pressure Amplitude for $\alpha = 2° \pm 0.5°$ and $k = 0.151$

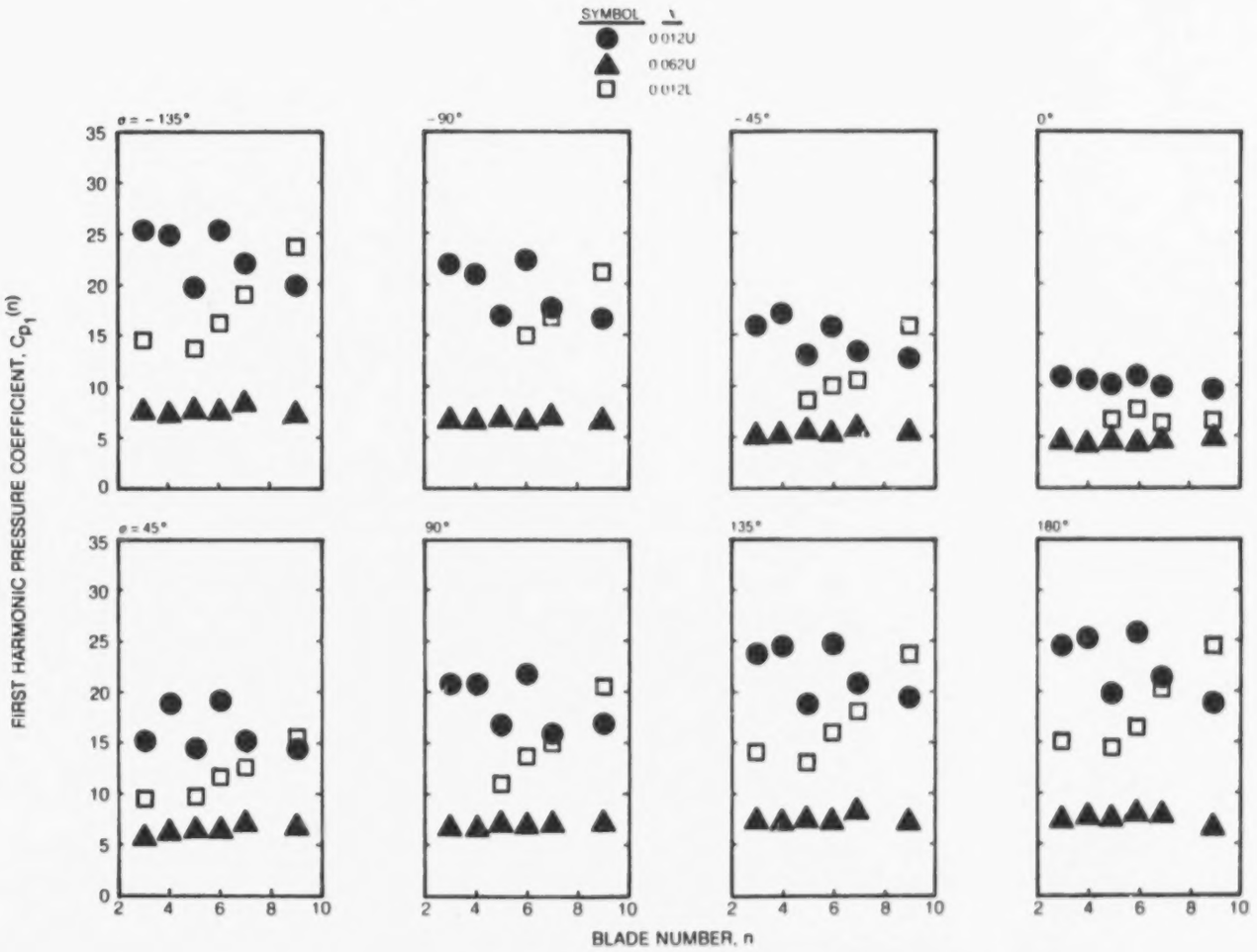

Figure 14 Gapwise Pressure Amplitude for $\alpha = 2° \pm 2°$ and k = 0.151

BEST DOCUMENT AVAILABLE

BEST DOCUMENT AVAILABLE

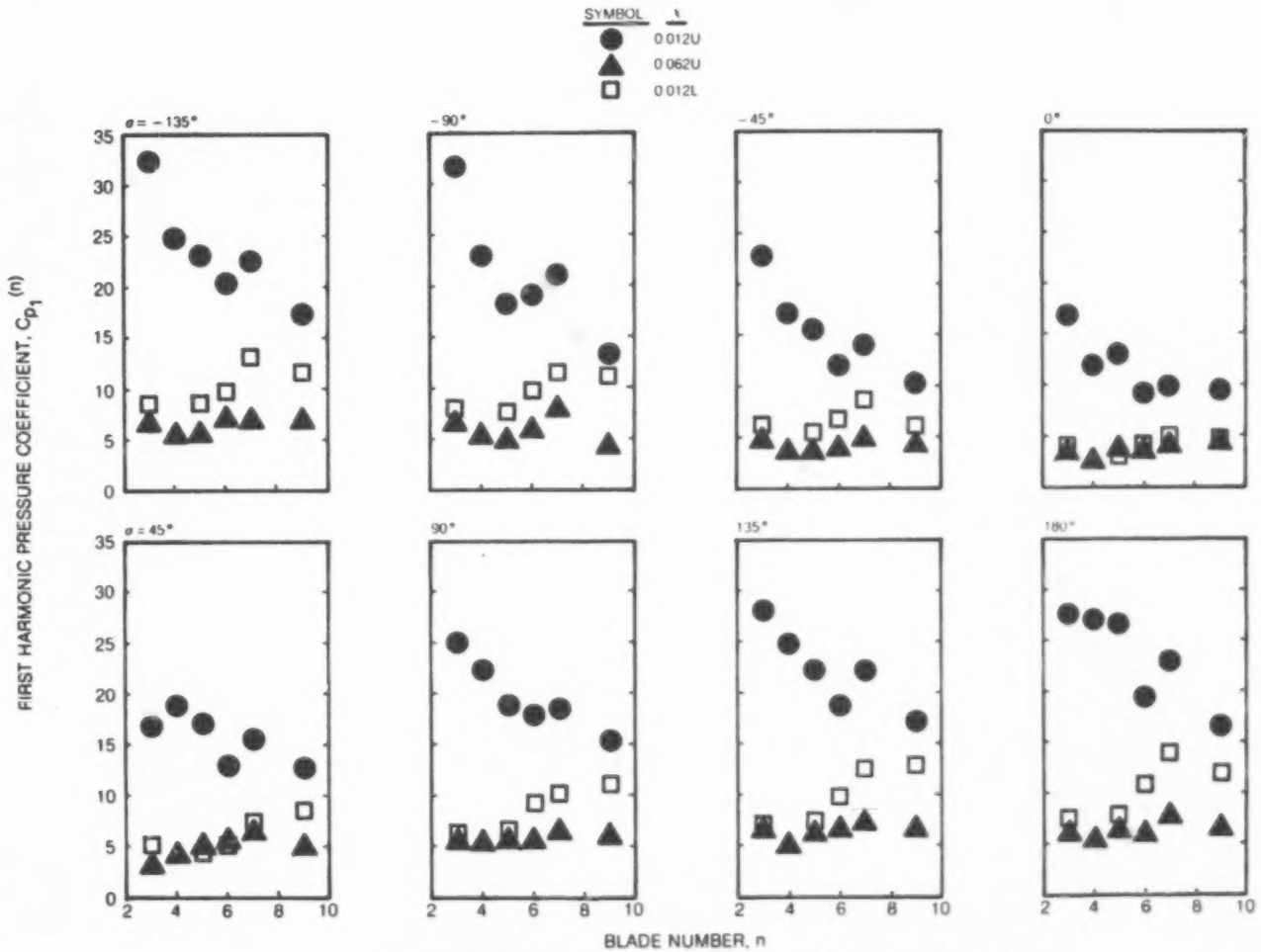

Figure 15 Gapwise Pressure Amplitude for $\alpha = 6° \pm 0.5°$ and $k = 0.151$

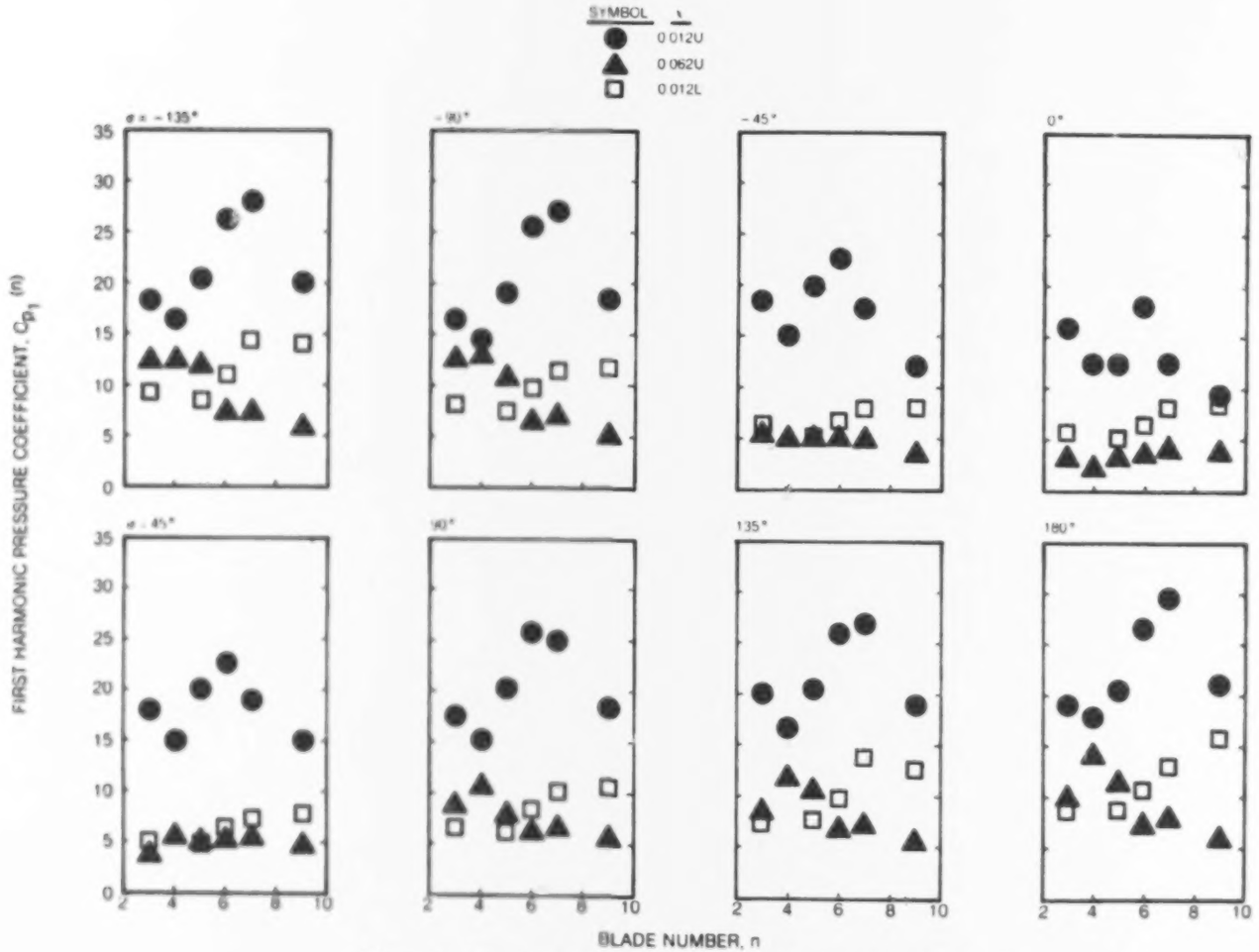

Figure 16 Gapwise Pressure Amplitude for $\alpha = 6° \pm 2°$ and k = 0.151

BEST DOCUMENT AVAILABLE

BEST_DOCUMENT_AVAILABLE

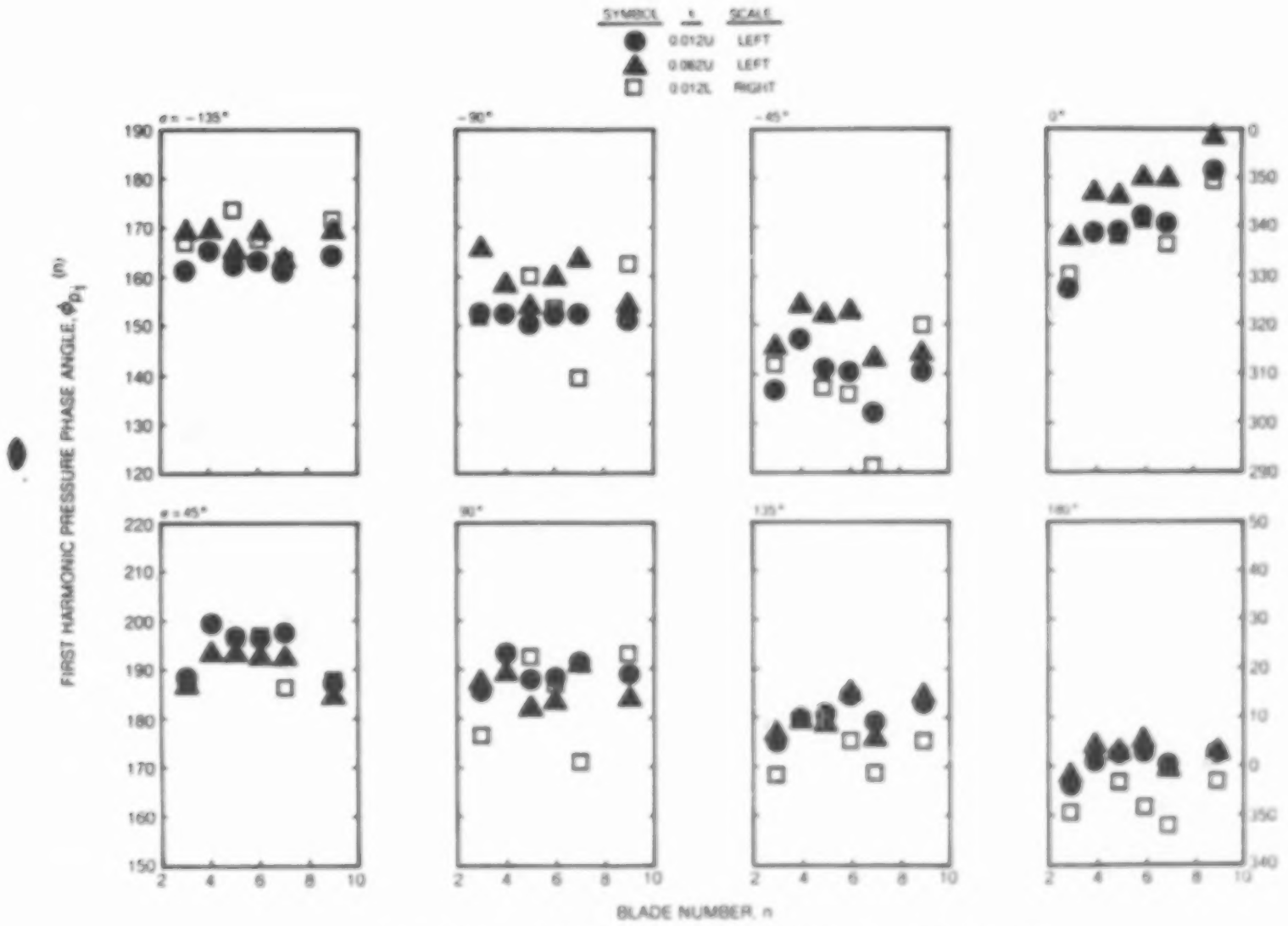

Figure 17 Gapwise Pressure Phase Angle for $\alpha = 2° \pm 0.5°$ and k = 0.151

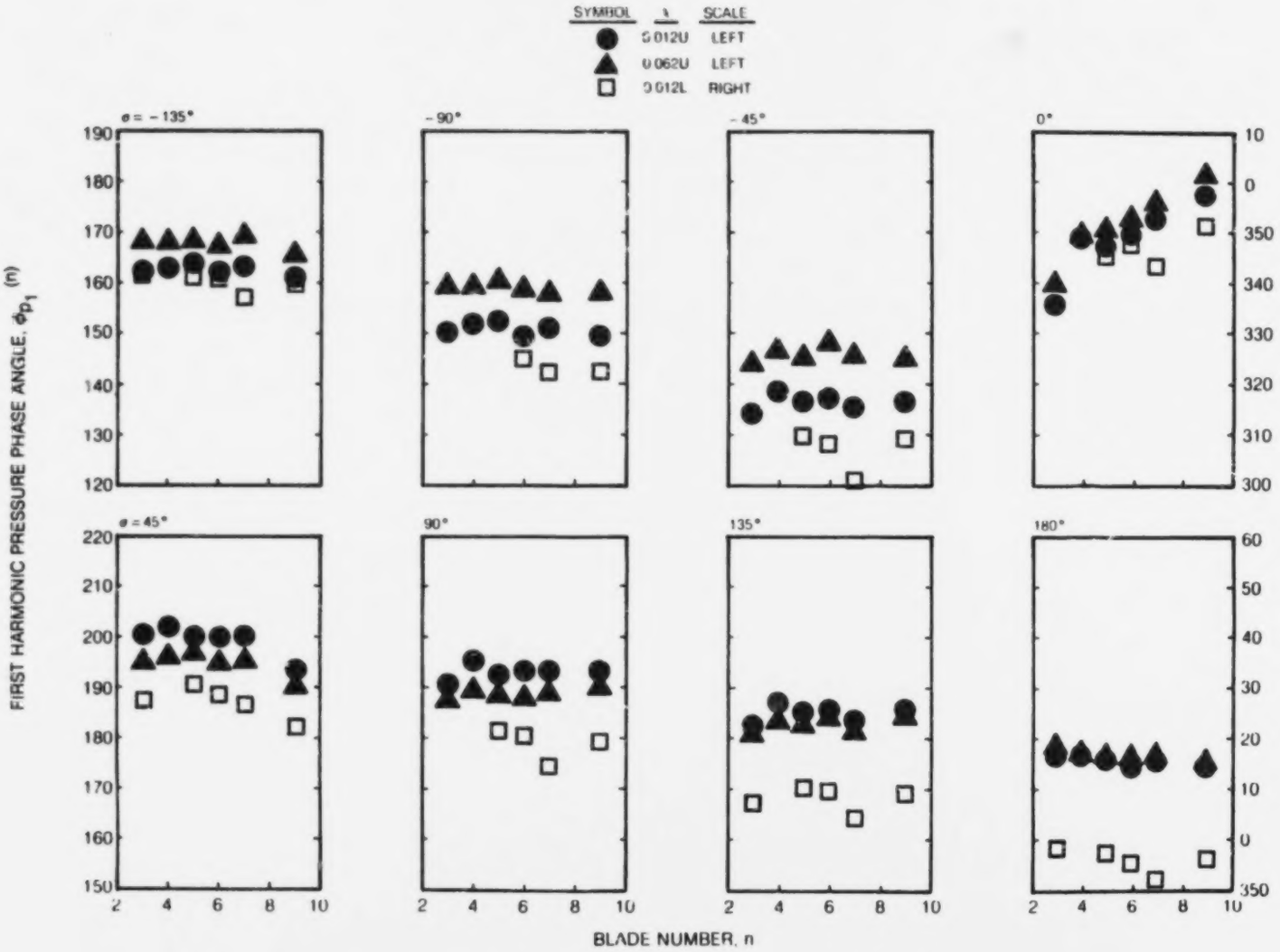

Figure 18 Gapwise Pressure Phase Angle for $\alpha = 2° \pm 2°$ and k = 0.151

BEST DOCUMENT AVAILABLE

BEST DOCUMENT AVAILABLE

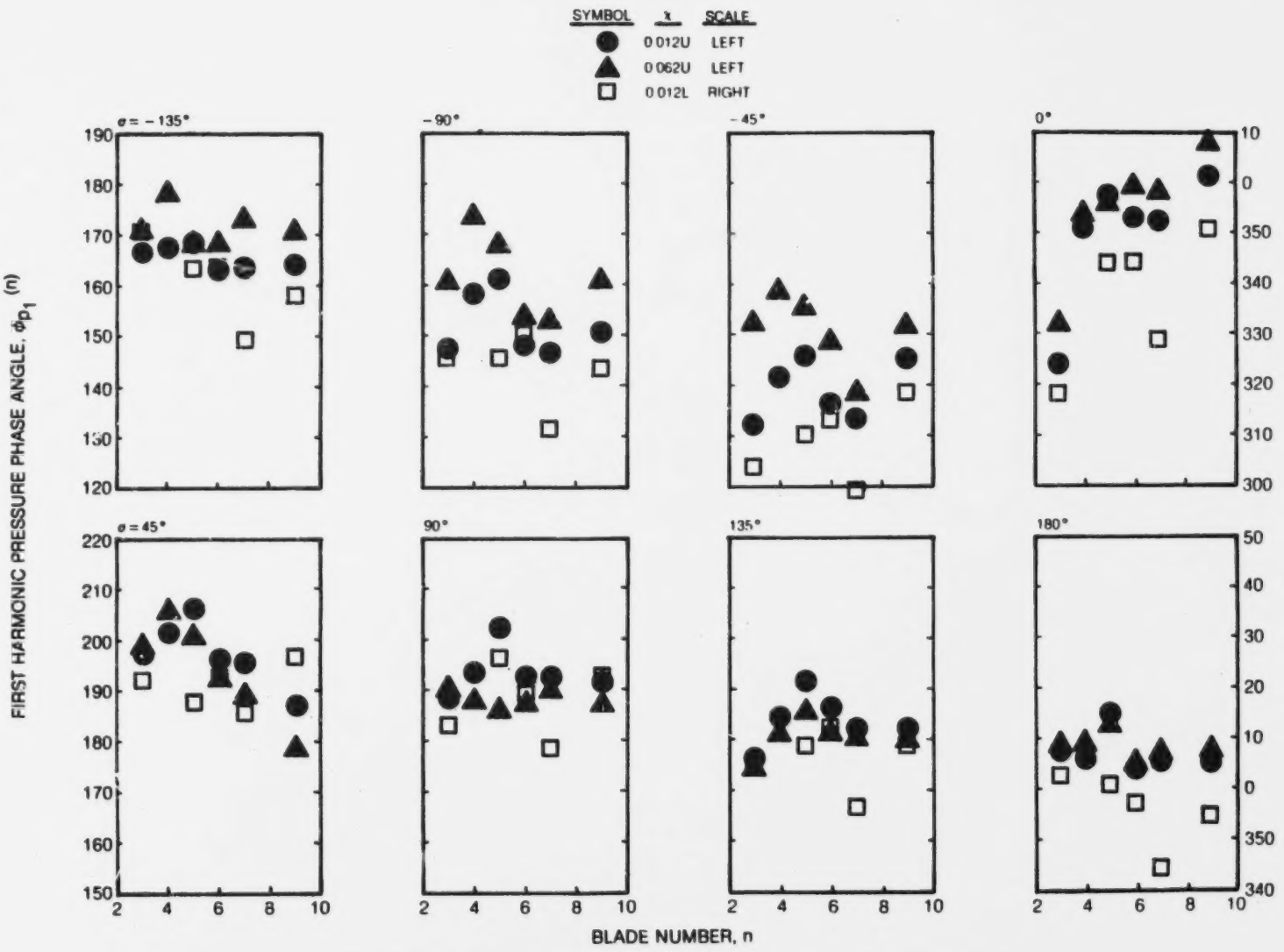

Figure 19 Gapwise Pressure Phase Angle for $\alpha = 6° \pm 0.5°$ and k = 0.151

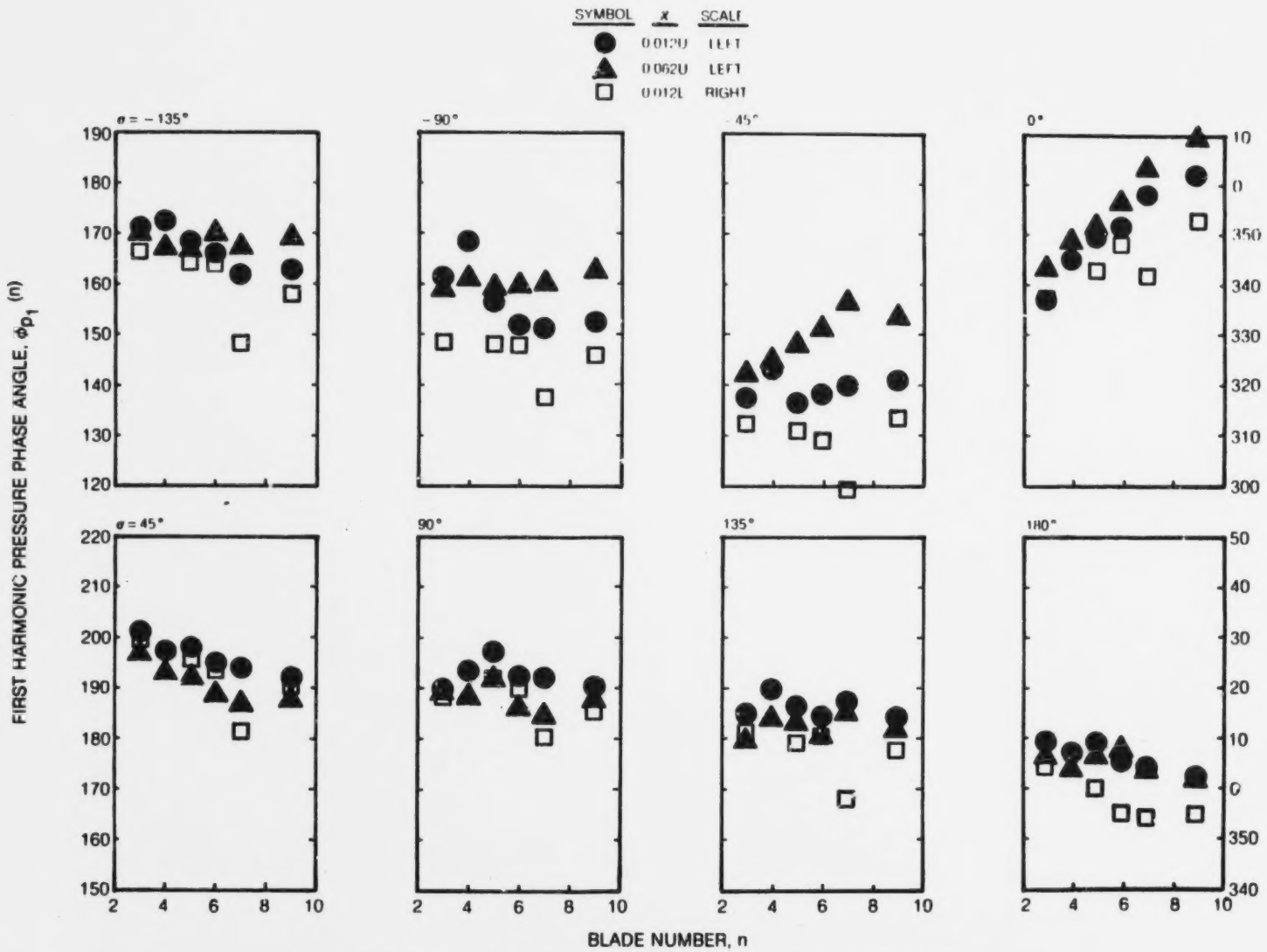

Figure 20 Gapwise Pressure Phase Angle for $\alpha = 6° \pm 2°$ and k = 0.151

BEST DOCUMENT AVAILABLE

BEST DOCUMENT AVAILABLE

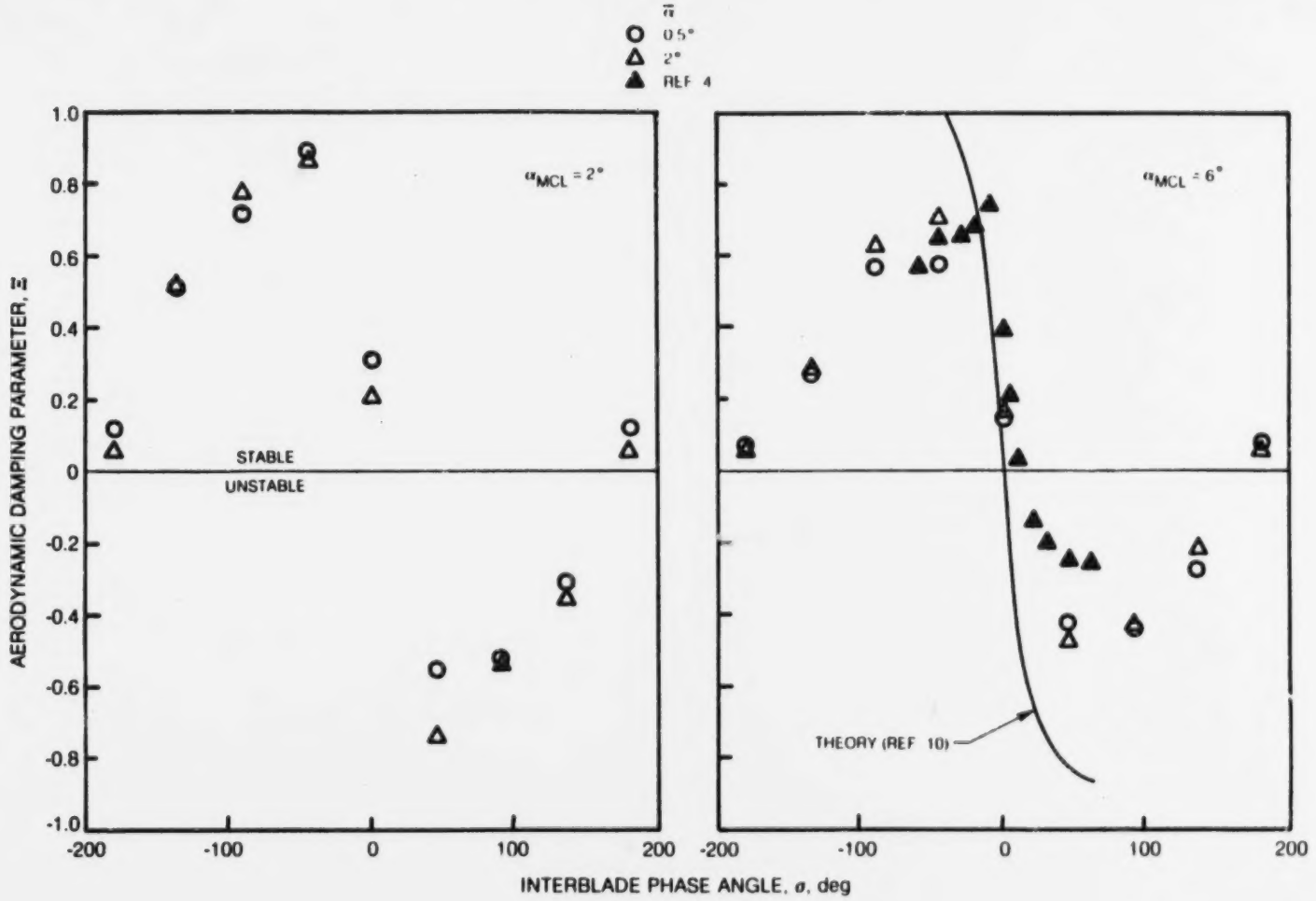

Figura 21. Effect of Pitching Amplitude on Aerodynamic Damping Parameter for k = 0.072

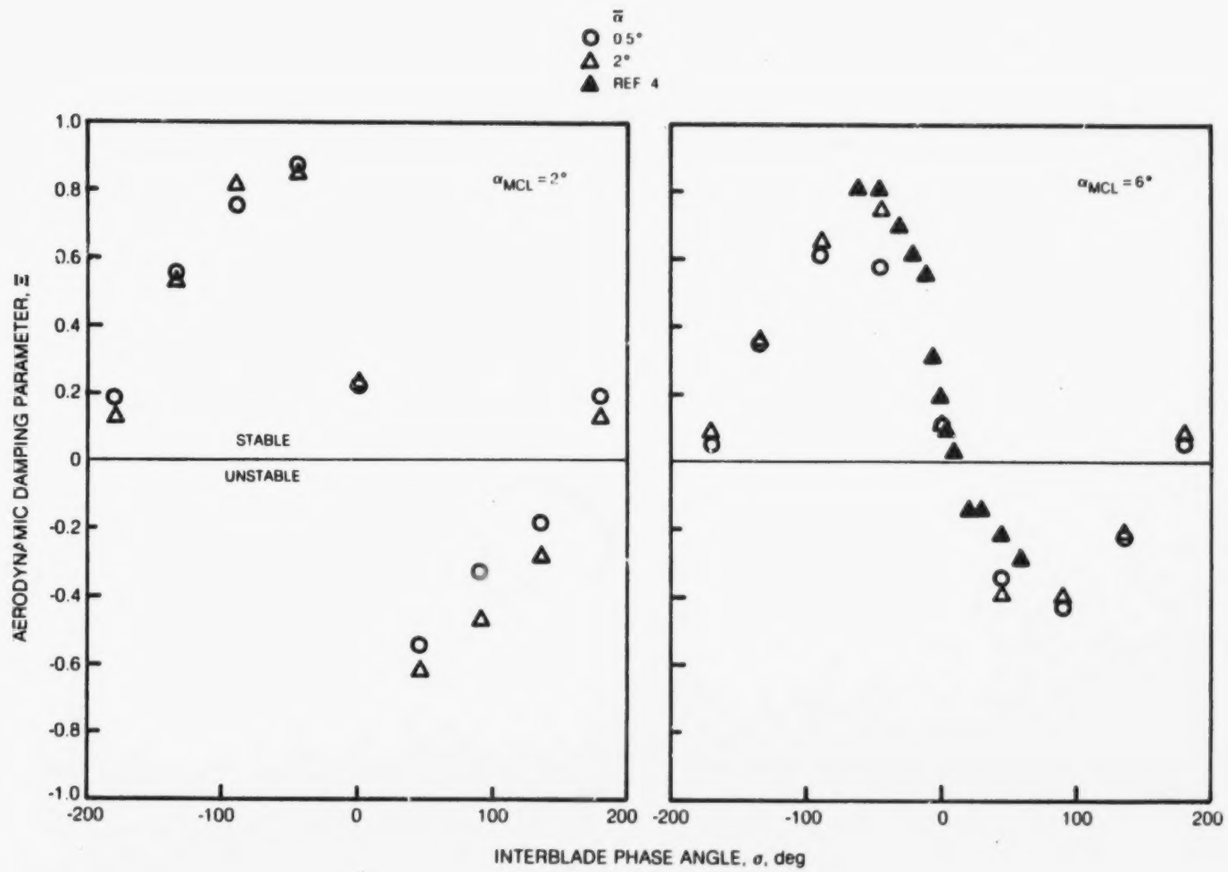

81-6-8-11

Figure 22 Effect of Pitching Amplitude on Aerodynamic Damping Parameter for k = 0.122

BEST DOCUMENT AVAILABLE

BEST DOCUMENT AVAILABLE

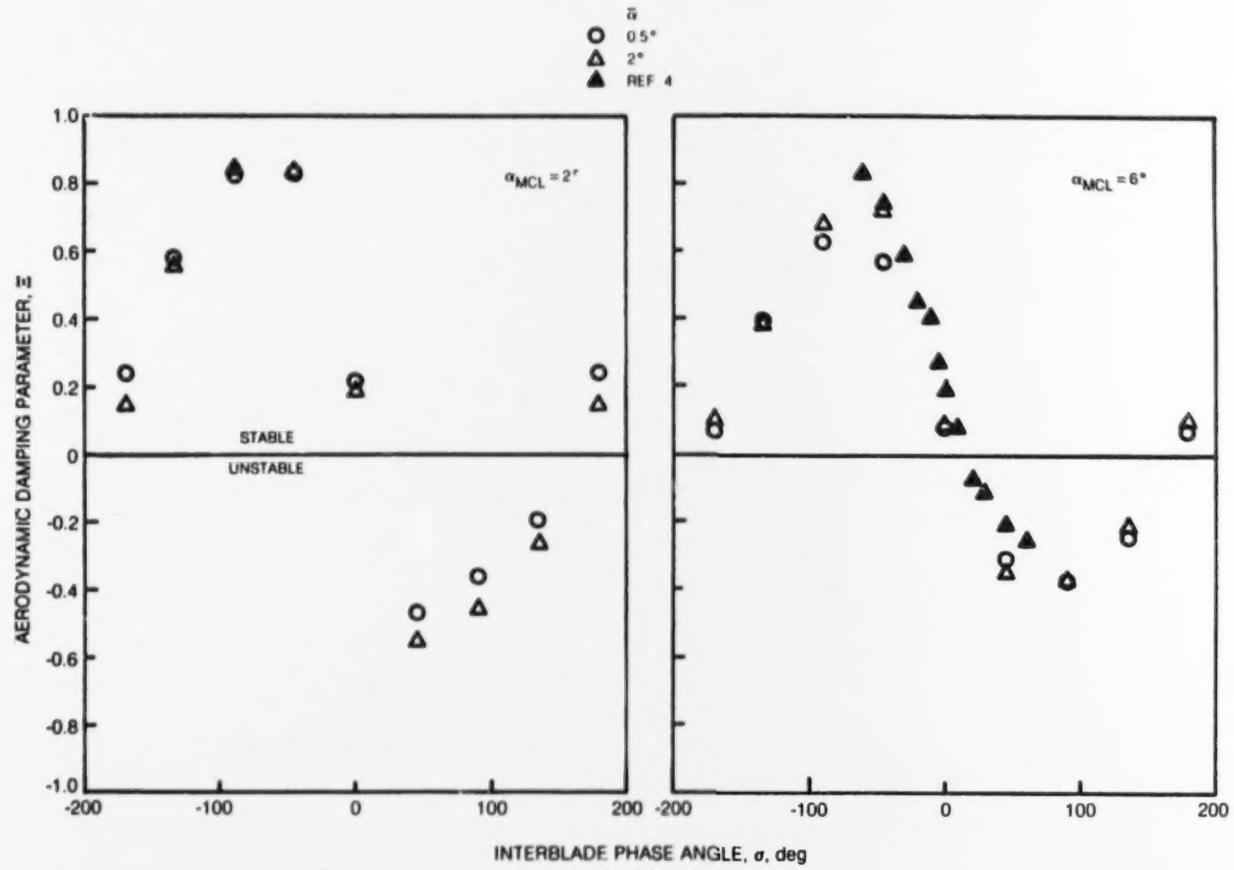

81-6-C4-12

Figure 23 Effect of Pitching Amplitude on Aerodynamic Damping Parameter for k = 0.151

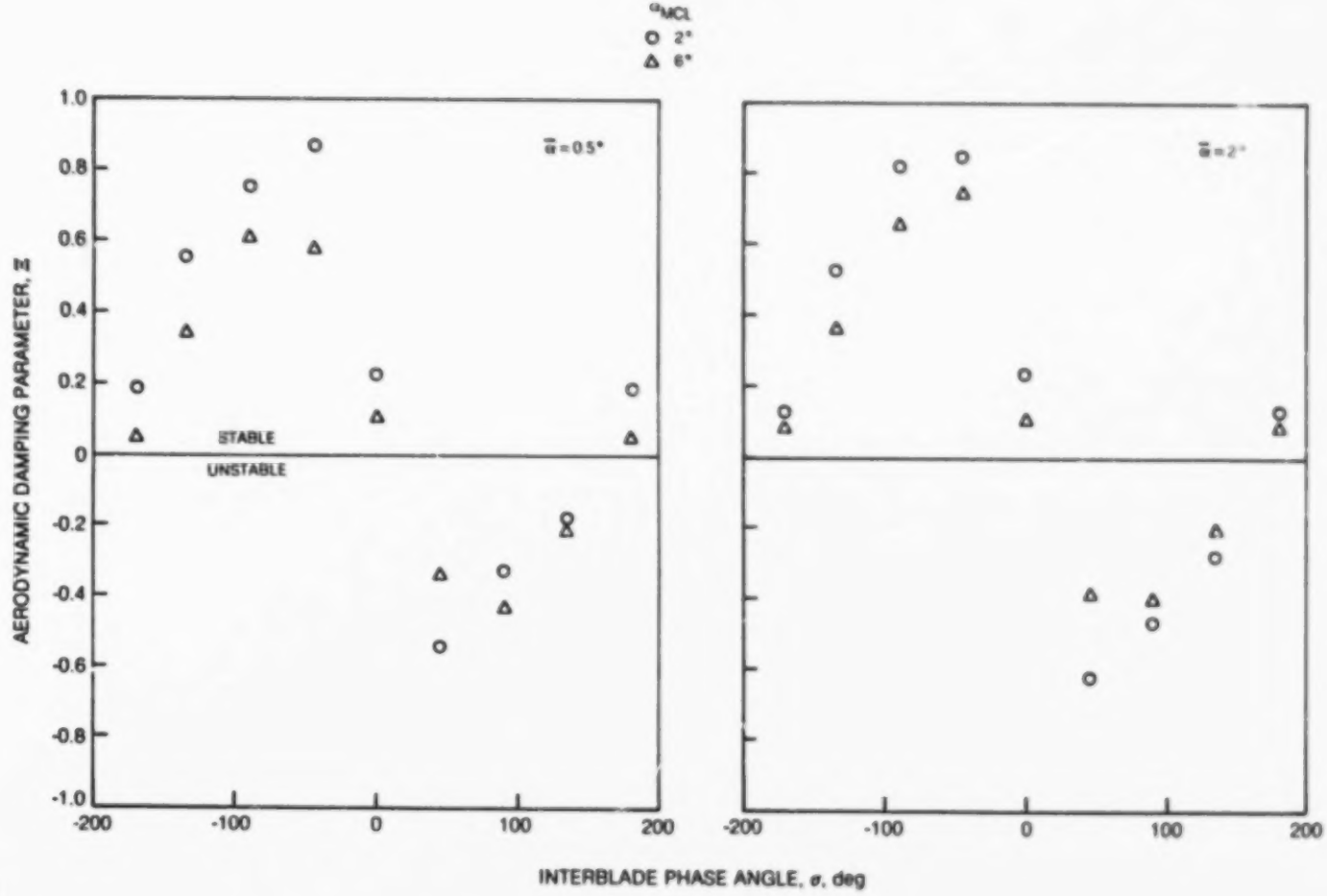

Figure 24 Effect of Incidence Angle on Aerodynamic Damping Parameter for k = 0.122

BEST DOCUMENT AVAILABLE

BEST DOCUMENT AVAILABLE

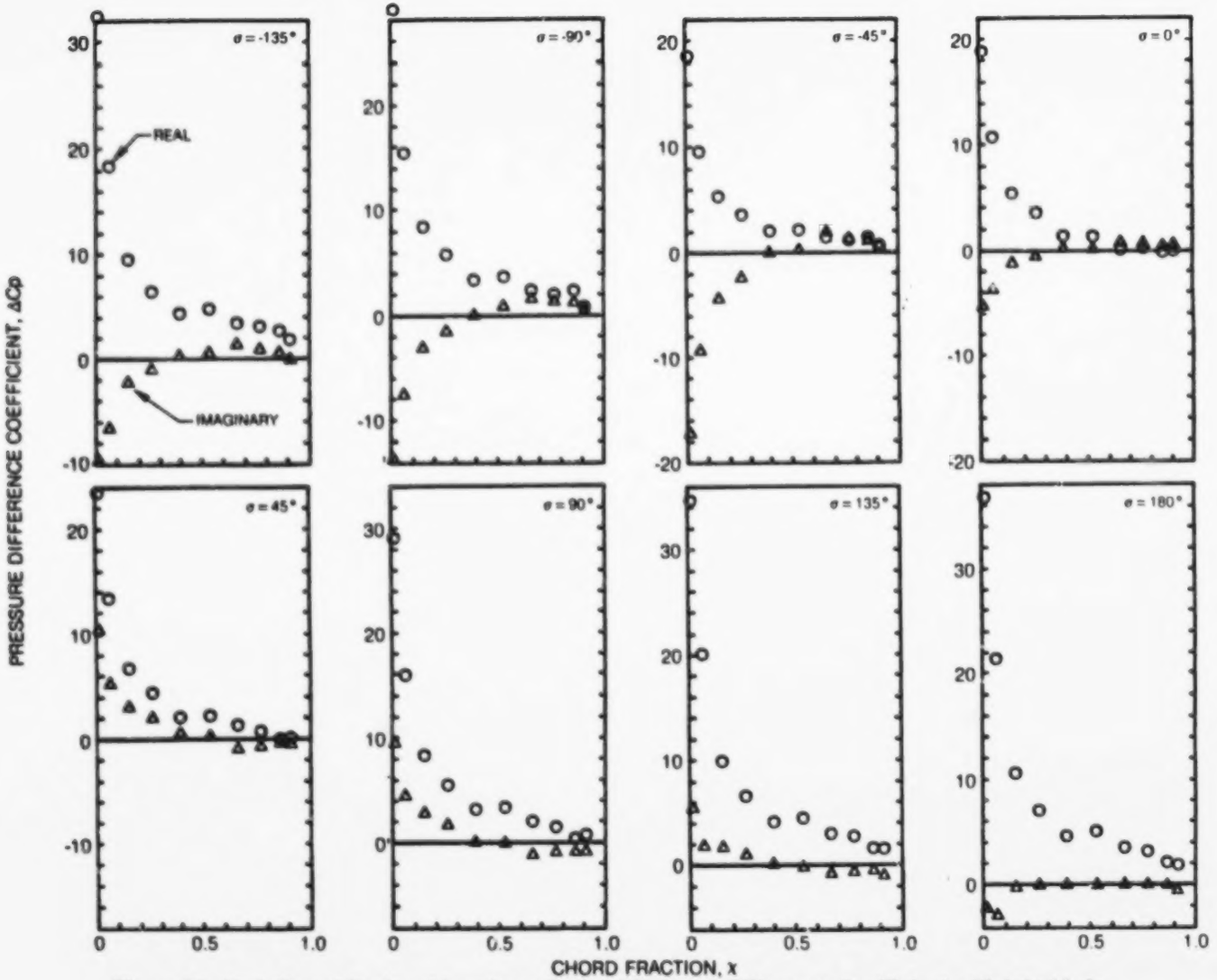

Figure 25 Variation of Real and Imaginary Parts of Pressure Difference Coefficient with Interblade Phase Angle for $\alpha = 2° \pm 0.5°$ and $k = 0.072$

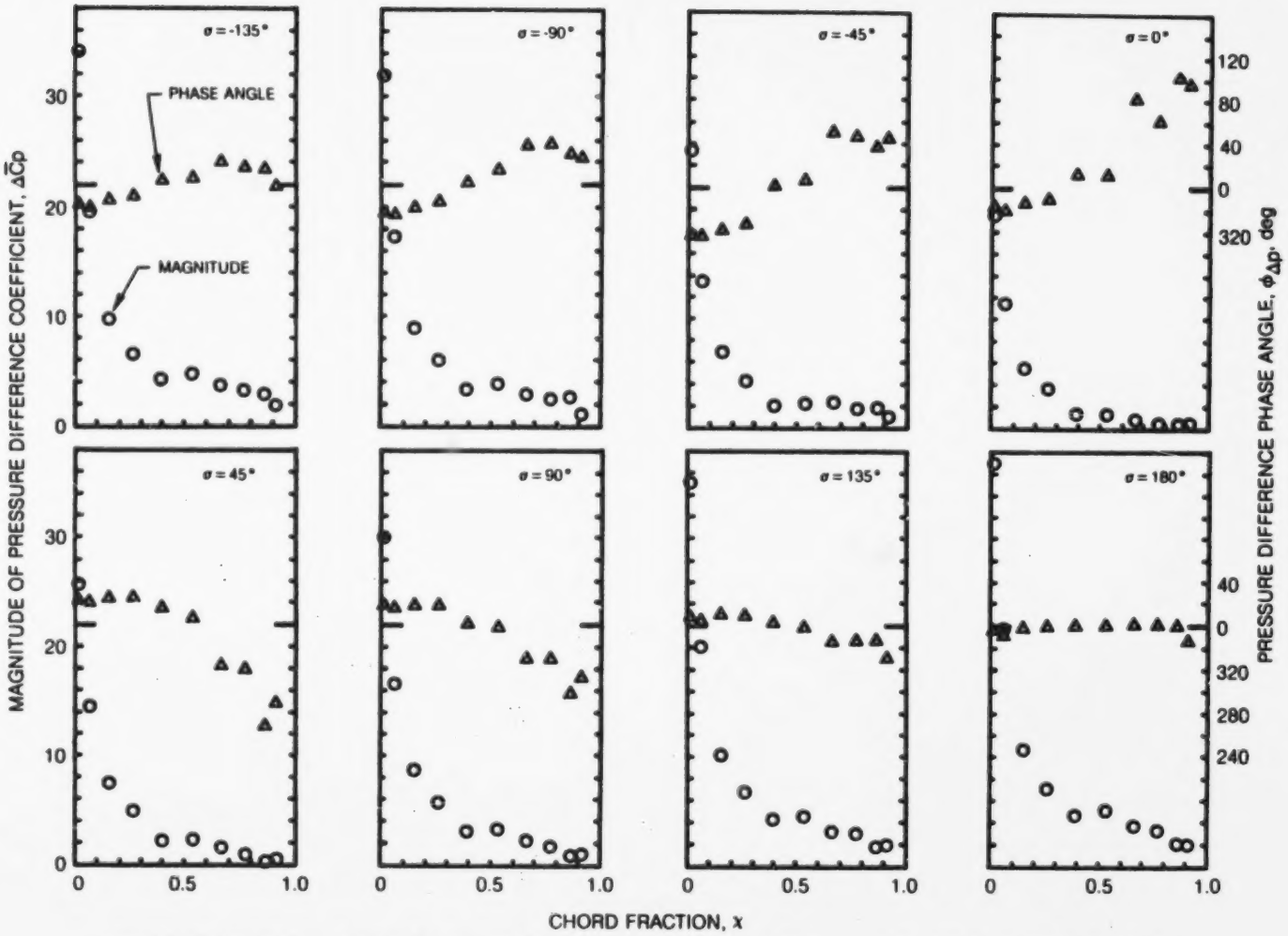

81-6-84-14

Figure 26 Variation of Magnitude and Phase Angle of Pressure Difference Coefficient with Interblade Phase Angle for $\alpha = 2° \pm 0.5°$ AND $k = 0.072$

BEST DOCUMENT AVAILABLE

BEST DOCUMENT AVAILABLE

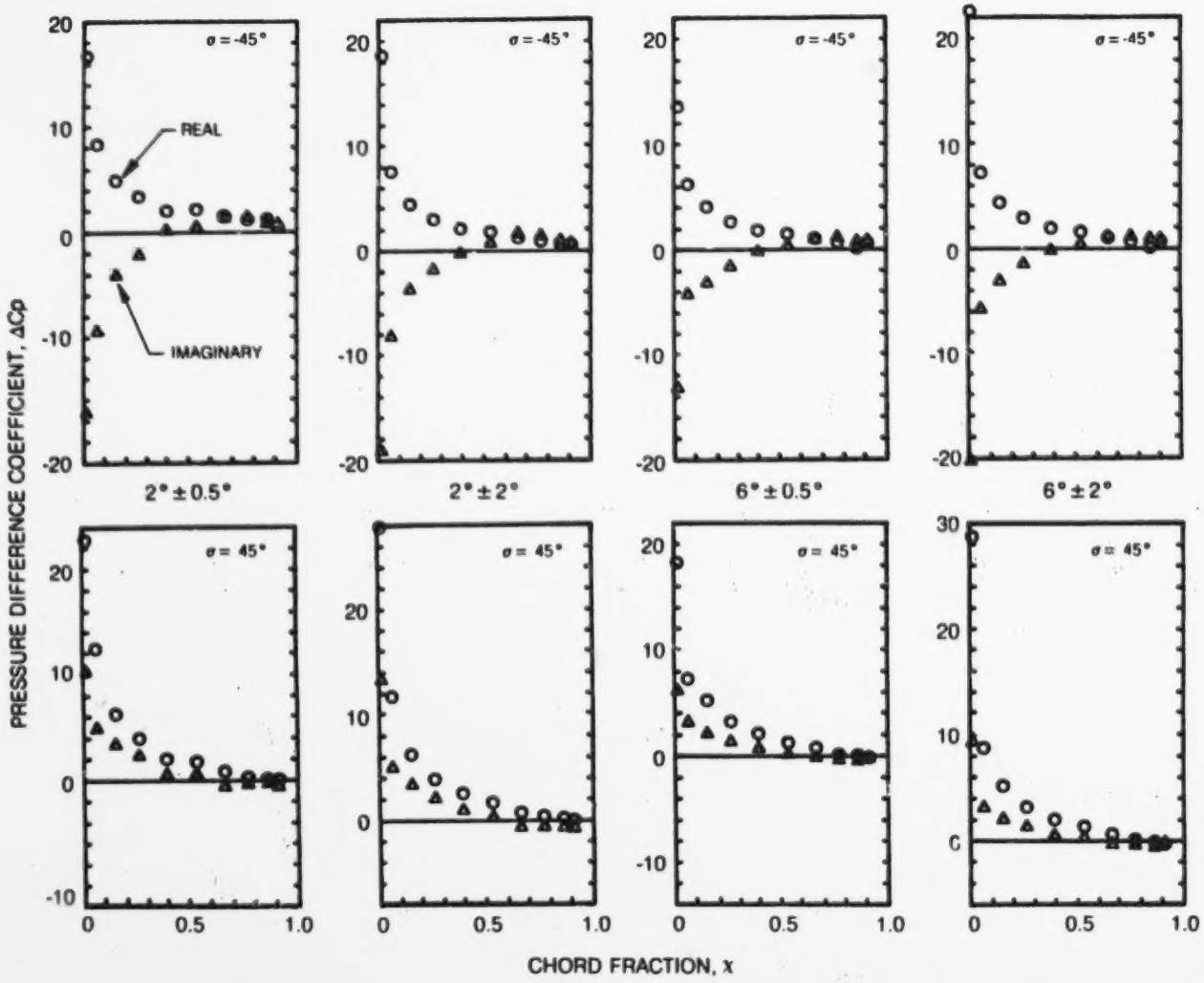

Figure 27 Variation of Real and Imaginary Parts of Pressure Difference Coefficient with Incidence and Pitching Amplitude for σ = ±45° and k = 0.122

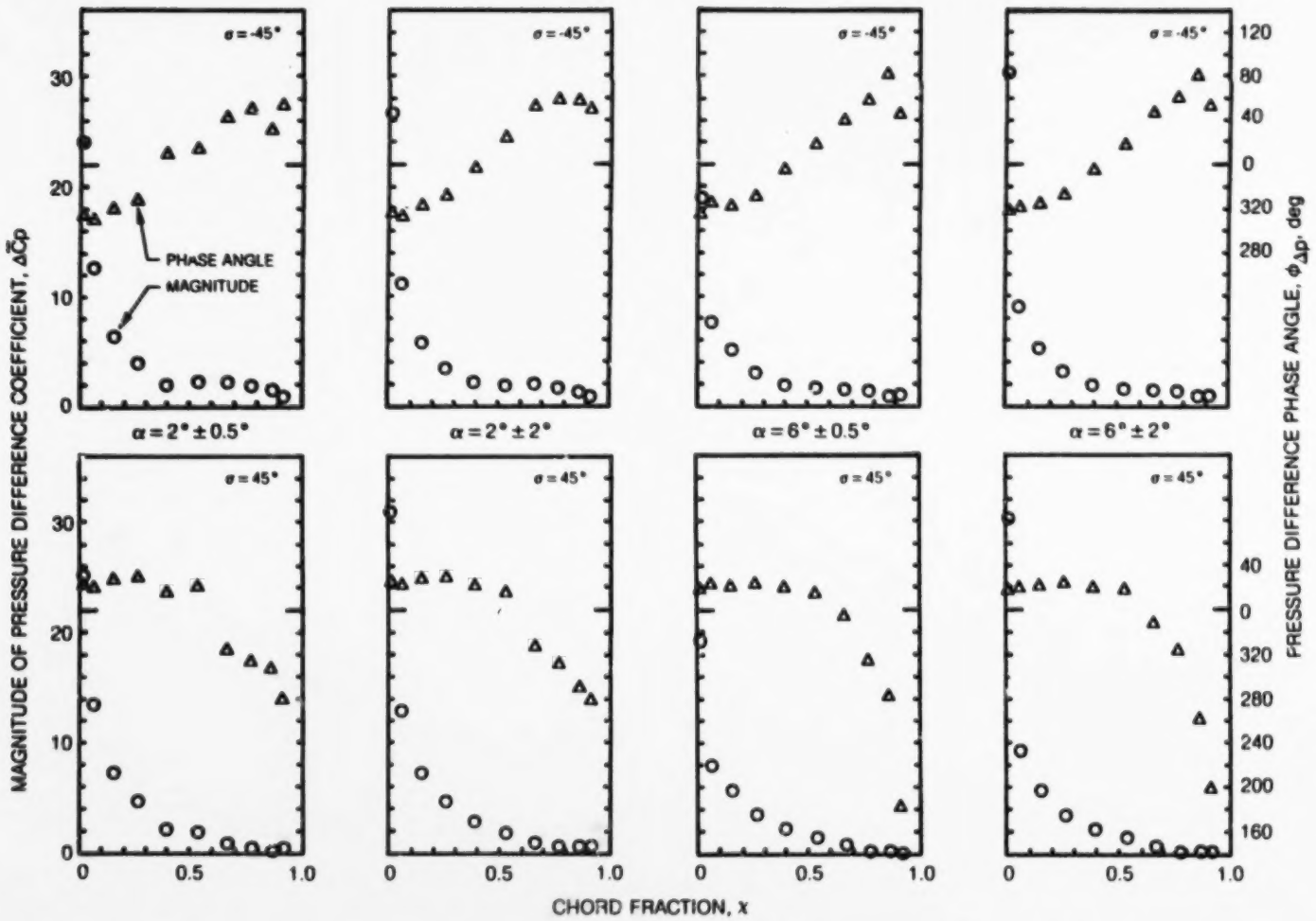

Figure 28 Variation of Magnitude and Phase Angle of Pressure Difference Coefficient with Incidence and Pitching Amplitude for $\sigma = \pm 45$ deg and k = 0.122

BEST DOCUMENT AVAILABLE

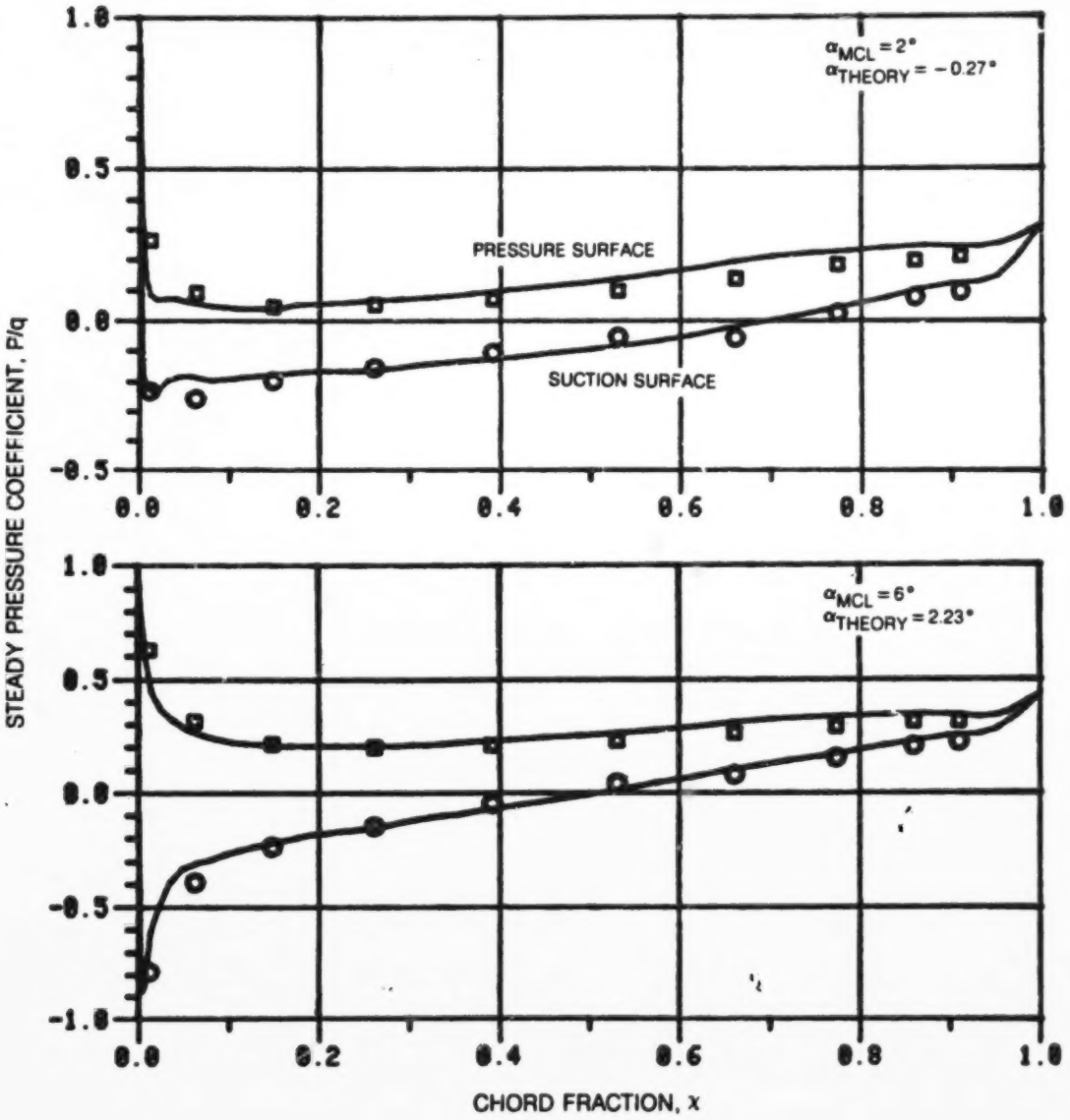

Figure 29 Steady-State Matching of Potential Flow Theory and Experiment

81-6-84-15

BEST DOCUMENT AVAILABLE

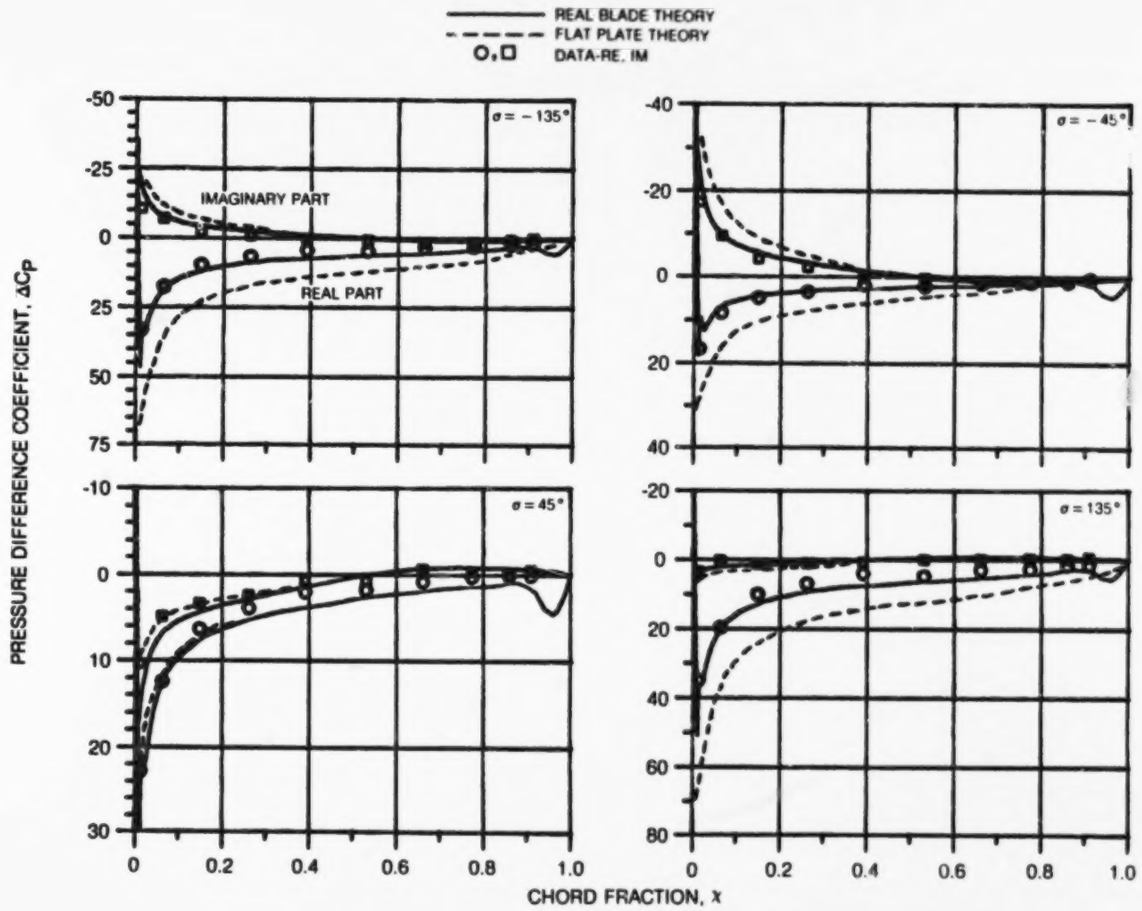

Figure 30. Comparison of Theory and Experiment for $\alpha = 2 \pm 0.5$ deg and $k = 0.122$

BEST DOCUMENT AVAILABLE

BEST DOCUMENT AVAILABLE

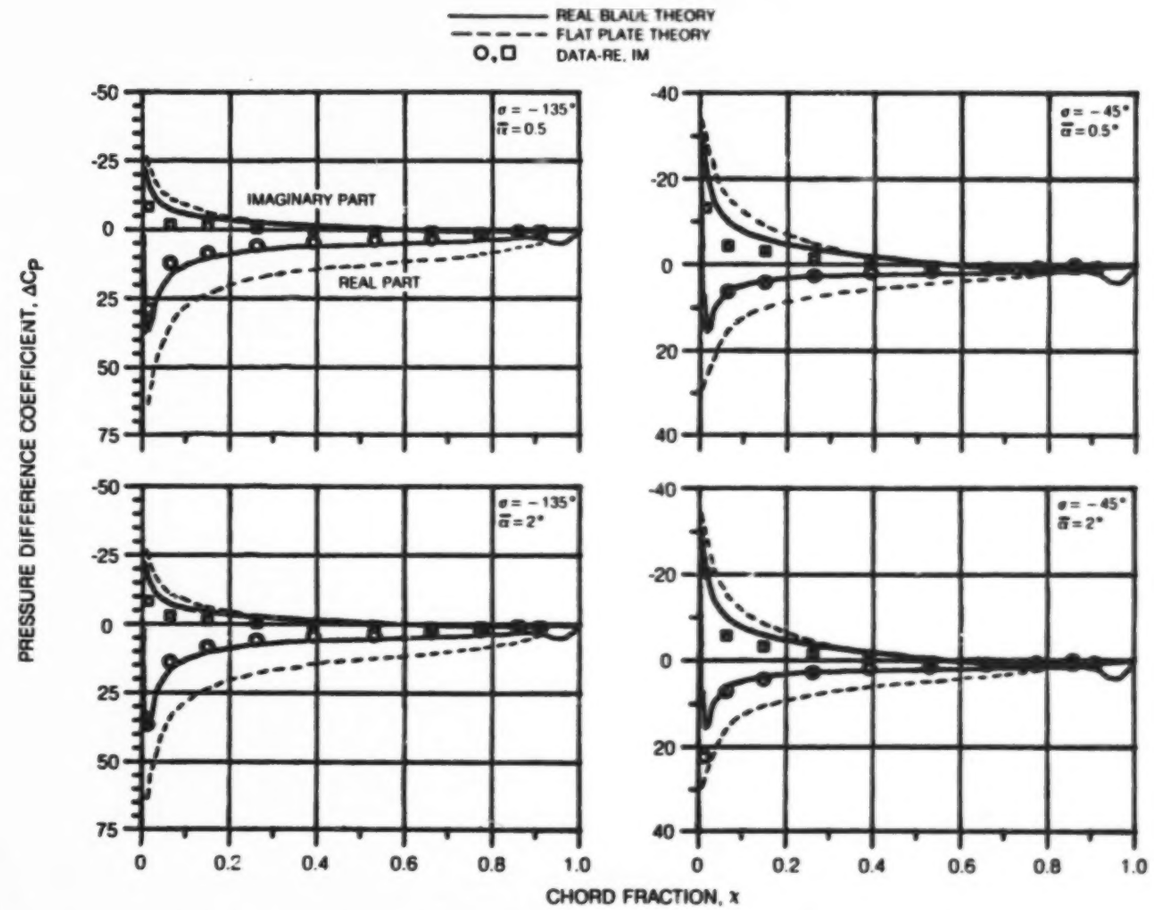

Figure 31. Comparison of Theory and Experiment for $\alpha_{MCL} = 8$ deg and k = 0.122

81-6-94-17

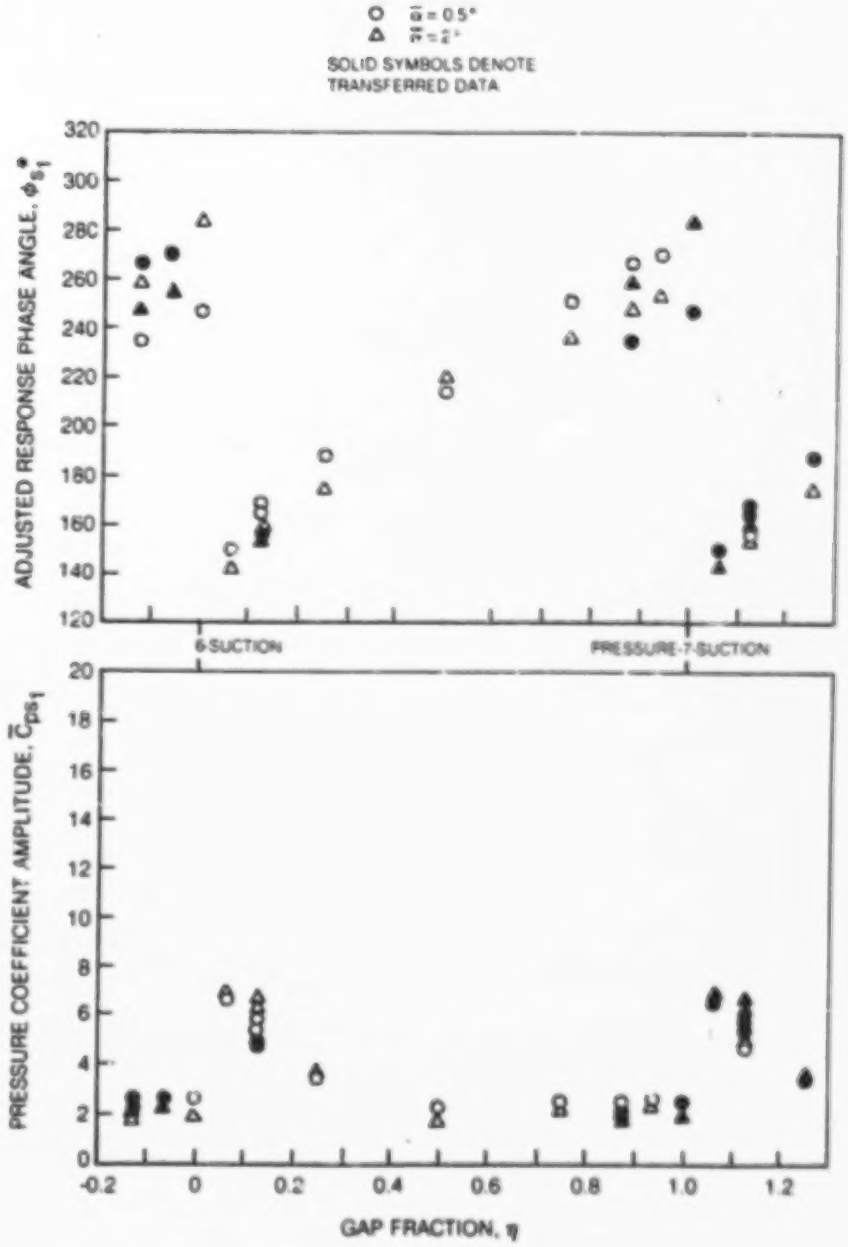

Figure 32 Variation of Intergap Pressure Magnitude and Phase Angle for $\alpha_{MCL} = 2°$, $\sigma = -45°$, and k = 0.151

81-6-84-20

BEST DOCUMENT AVAILABLE

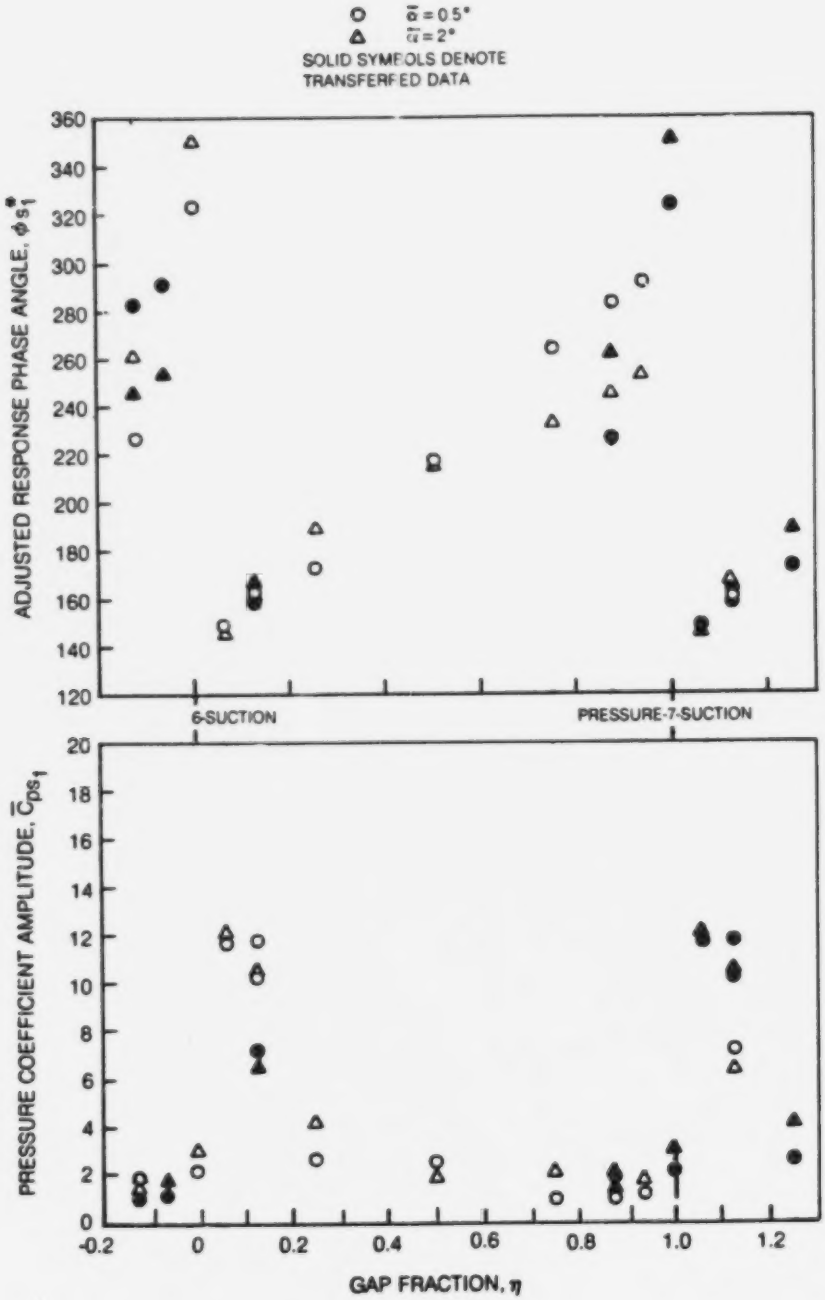

Figure 33 Variation of Intergap Pressure Magnitude and Phase Angle for $\alpha_{MCL} = 6°$, $\sigma = -45°$, and k = 0.151

81-6-84-21

BEST DOCUMENT AVAILABLE

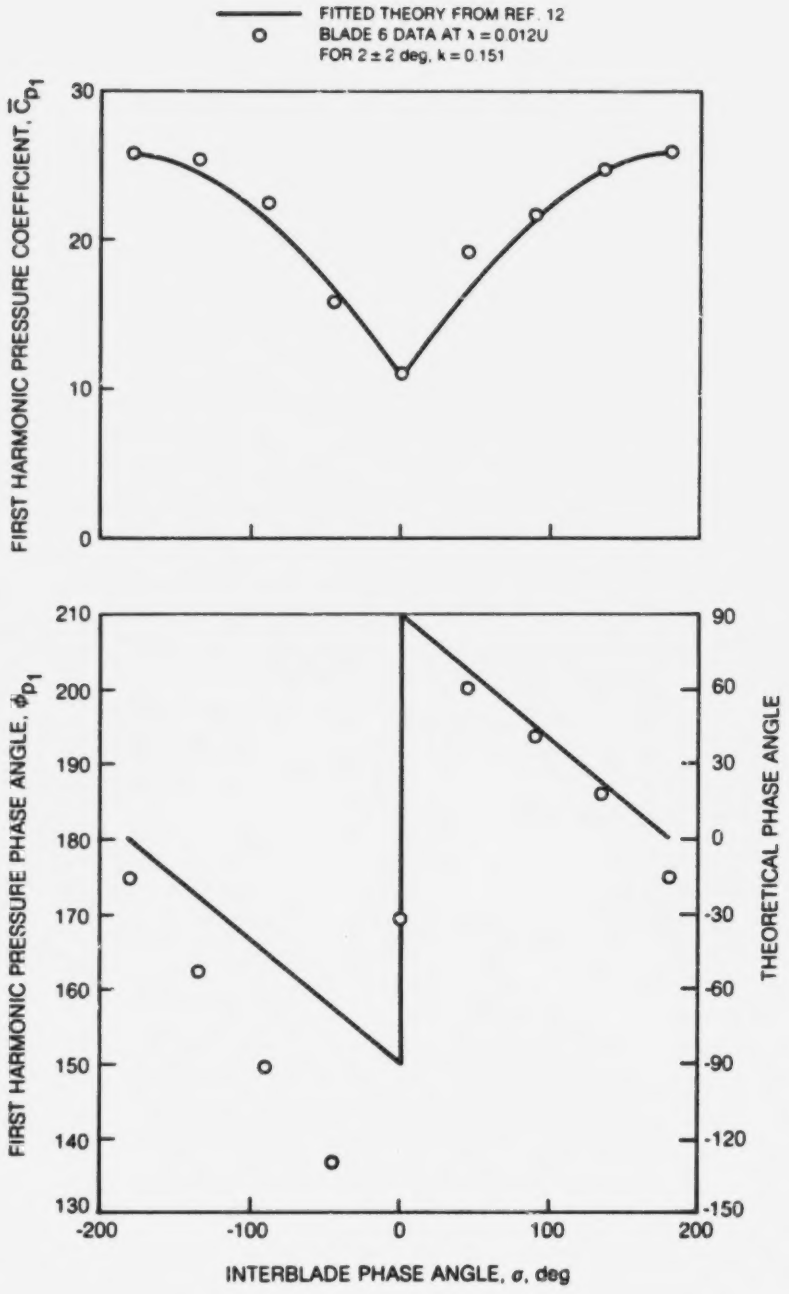

Figure 34 Comparison of Blade Data with Simple Fitted Theory

81-6-84-22

BEST DOCUMENT AVAILABLE

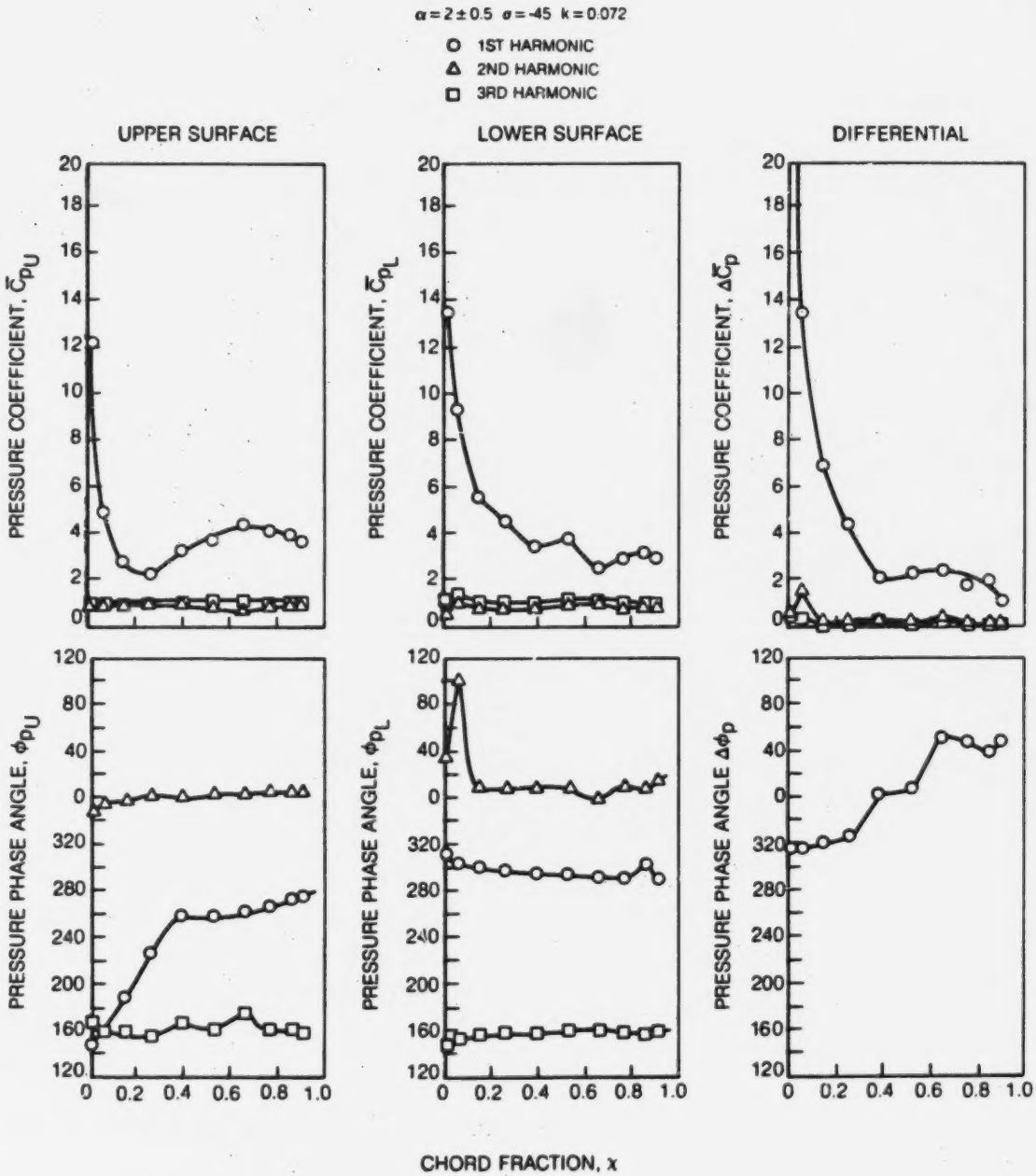

Figure 35 Higher Harmonic Content of Pressure Magnitude and Phase Angle

81-6-157-1

BEST DOCUMENT AVAILABLE

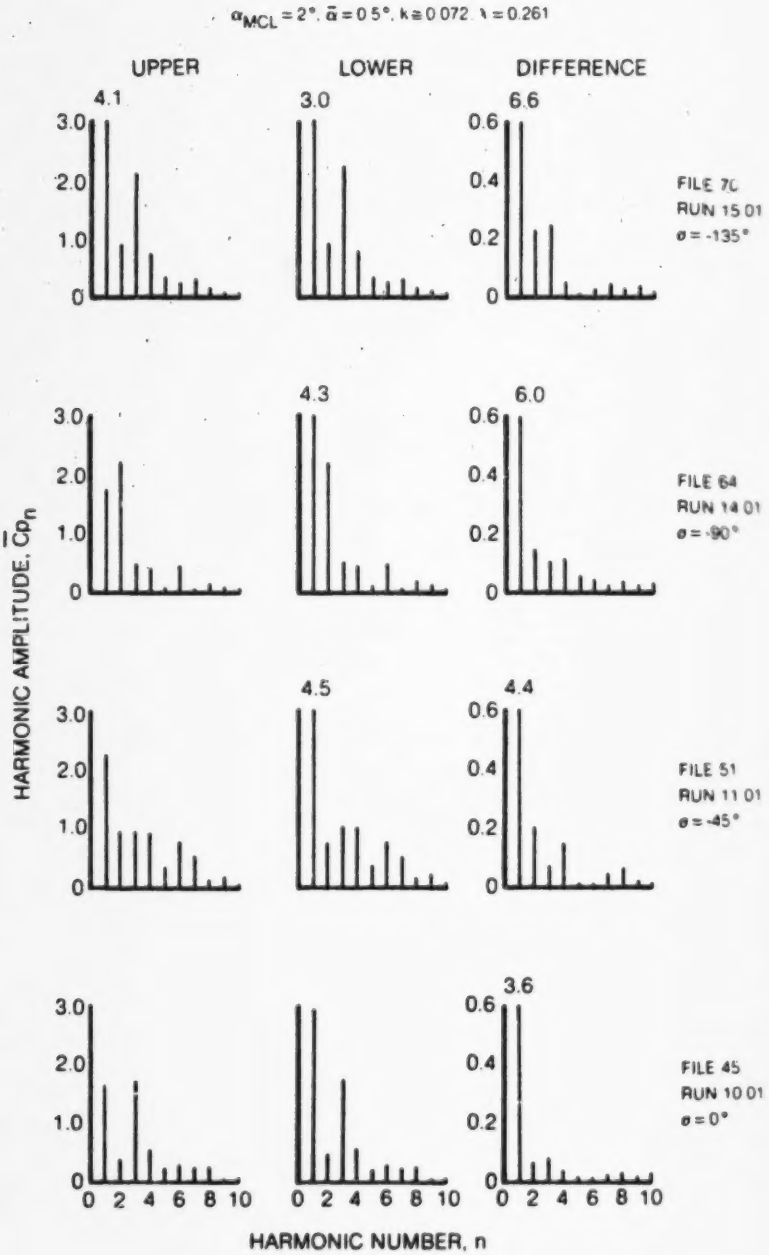

Figure 36 Spectral Histogram for Pressure Amplitude

81-7-1-1

BEST DOCUMENT AVAILABLE

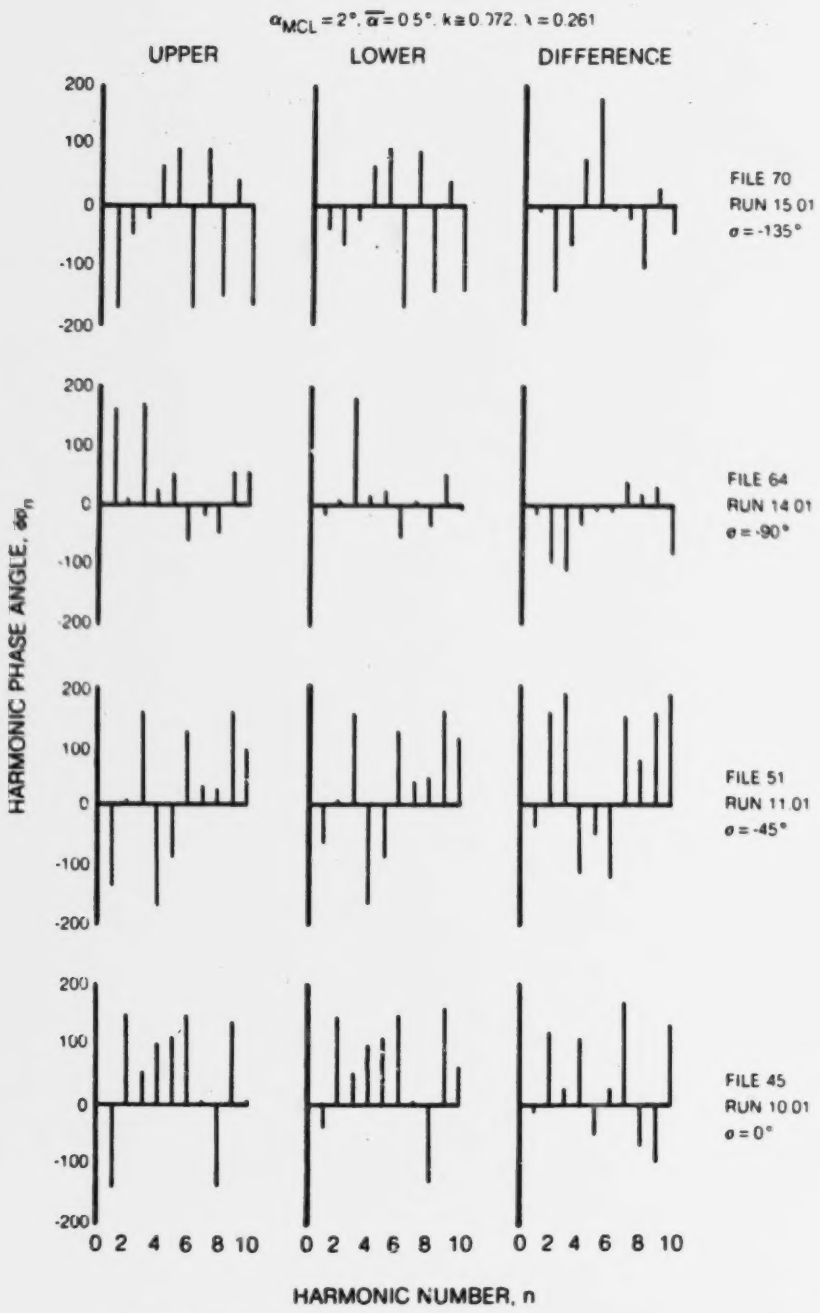

Figure 37 Spectral Histogram for Pressure Phase Angle

81-7-1-2

BEST DOCUMENT AVAILABLE

BEST DOCUMENT AVAILABLE

1. Report No.	2. Government Accession No.	3. Recipient's Catalog No.
NASA CR-3513		

4. Title and Subtitle	5. Report Date
AN EXPERIMENTAL INVESTIGATION OF GAPWISE PERIODICITY AND UNSTEADY AERODYNAMIC RESPONSE IN AN OSCILLATING CASCADE. I - EXPERIMENTAL AND THEORETICAL RESULTS	June 1982
	6. Performing Organization Code

7. Author(s)	8. Performing Organization Report No.
Franklin O. Carta	R81-914618-27
	10. Work Unit No.

9. Performing Organization Name and Address	11. Contract or Grant No.
United Technologies Research Center Silver Lane East Hartford, Conn. 06108	NAS3-22018
	13. Type of Report and Period Covered
12. Sponsoring Agency Name and Address	Contractor Report
National Aeronautics and Space Administration Washington, D.C, 20546	14. Sponsoring Agency Code 510-55-12

15. Supplementary Notes

Final report. Project Manager, Donald R. Boldman, Fluid Mechanics and Acoustics Division, NASA Lewis Research Center, Cleveland, Ohio 44135.

16. Abstract

Tests were conducted on a linear cascade of airfoils oscillating in pitch to measure the unsteady pressure response on selected blades along the leading edge plane of the cascade, over the chord of the center blade, and on the sidewall in the plane of the leading edge. The tests were conducted at a constant inlet velocity of 61 m/sec (200 ft/sec) for all 96 combinations of 2 mean camberline incidence angles (α_{MCL} = 2 and 6 deg), 2 pitching amplitudes ($\bar{\alpha}$ = 0.5 and 2 deg), 3 reduced frequencies (k = 0.072, 0.122, and 0.151 based on semi chord), and 8 interblade phase angles (σ = 0, ± 45, ± 90, ± 135, 180 deg). The pressure data were reduced to Fourier coefficient form for direct comparison, and were also processed to yield integrated loads and, particularly, the aerodynamic damping coefficient. In addition, results from the unsteady Verdon/Caspar theory for cascaded blades with nonzero thickness and camber were compared with the experimental measurements. A compilation of all data obtained during the test program is presented in NASA CR-165457. The three primary results that emerged from this investigation were: 1) from the leading edge plane blade data, the cascade was judged to be periodic in unsteady flow over the range of parameters tested, 2) as before, the interblade phase angle was found to be the single most important parameter affecting the stability of the oscillating cascade blades, and 3) the real blade theory and the experiment were in excellent agreement for the several cases chosen for comparison. These are felt to be particularly significant because 1) this was the first known test of unsteady periodicity in cascade, and its verification lends credence to the self-consistency of the data gathered herein, 2) the cascade damping measurements continue to corroborate previous assessments of the importance of interblade phase angle in controlling stability, and 3) the mutual agreement of real blade theory and experiment represents an important milestone because it establishes the validity of both.

17. Key Words (Suggested by Author(s))	18. Distribution Statement
Cascade aerodynamics; Unsteady cascade periodicity; Cascade instability; Unsteady cascade theory; Interblade phase angle; Unsteady flow; Oscillating airfoils; Unsteady pressure distributions	Unclassified - unlimited STAR Category 02

19. Security Classif. (of this report)	20. Security Classif. (of this page)	21. No. of Pages	22. Price*
Unclassified	Unclassified	101	A06

* For sale by the National Technical Information Service, Springfield, Virginia 22161

NASA-Langley, 1982